Gamma-ray detection and Compton camera image reconstruction with application to hadron therapy.

Mirela Frandes

Numéro d'ordre : 2010-ISAL-0067 Année 2010

THÈSE

présentée devant

L'Université de Lyon

L'Institut National des Sciences Appliquées de Lyon

pour obtenir
LE GRADE DE DOCTEUR

ÉCOLE DOCTORALE : ÉLECTRONIQUE, ÉLECTROTECHNIQUE, AUTOMATIQUE

par

Mirela Frandes

Gamma-ray detection and Compton camera image reconstruction with application to hadron therapy

Soutenue le 16 septembre 2010 devant le jury:

Laurent Desbat	Professeur, Université Joseph Fourier	Rapporteur
Mai Nguyen-Verger	Professeur, Université de Cergy-Pontoise	Rapporteur
Denis Dauvergne	Directeur de Recherche CNRS, IPN Lyon	Examinateur
Voichita Maxim	Maître de Conférences, INSA Lyon	Co-encadrante
Rémy Prost	Professeur, INSA Lyon	Directeur de Thèse
Isabelle Magnin	Directrice de recherche Inserm, CREATIS	Président du jury

'. . . be transformed by the renewing of your mind. . . '
Romans 12:2

Résumé

Une nouvelle technique de radiothérapie, l'hadronthérapie, irradie les tumeurs à l'aide d'un faisceau de protons ou d'ions carbone. L'hadronthérapie est très efficace pour le traitement du cancer car elle permet le dépôt d'une dose létale très localisée, en un point dit 'pic de Bragg', à la fin du trajet des particules. La connaissance de la position du pic de Bragg, avec une précision millimétrique, est essentielle car l'hadronthérapie a prouvé son efficacité dans le traitement des tumeurs profondes, près des organes vitaux, ou radio-résistantes.

Un enjeu majeur de l'hadronthérapie est le contrôle de la délivrance de la dose pendant l'irradiation. Actuellement, les centres de traitement par hadronthérapie effectuent un contrôle post-thérapeutique par tomographie par émission de positron (TEP). Les rayons gamma utilisés proviennent de l'annihilation de positons émis lors la désintégration bêta des isotopes radioactifs créés par le faisceau de particules. Les images TEP ne sont pas en coïncidence directe avec le pic de Bragg. Une alternative est l'imagerie des rayons gamma nucléaires émis suites aux interactions inélastiques des hadrons avec les noyaux des tissus. Cette émission est isotrope, présentant un spectre à haute énergie allant de 100 keV à 20 MeV. Une technique avancée de détection des rayons gamma est proposée. Elle est basée sur la diffusion Compton avec possibilité de poursuite des électrons diffusés. Cette technique de détection Compton a été initialement appliquée pour observer les rayons gamma en astrophysique (télescope Compton). Un dispositif, inspiré de cette technique, a été modélisé avec une géométrie adaptée à l'Imagerie en HadronThérapie (IHT). Il se compose d'un diffuseur, où les électrons Compton sont mesurés et suivis ('tracker'), et d'un calorimètre, où les rayons gamma sont absorbés par effet photoélectrique. Un scénario d'hadronthérapie a été simulé par la méthode de Monte-Carlo, en suivant la chaîne complète de détection, de la reconstruction d'événements individuels jusqu'à la reconstruction d'images de la source de rayons gamma. L'algorithme 'Expectation Maximisation' (EM) à été adopté dans le calcul de l'estimateur du maximum de vraisemblance (MLEM) en mode liste pour effectuer la reconstruction d'images. Il prend en compte la réponse du système d'imagerie qui décrit le comportement complexe du détecteur. La modélisation de cette réponse nécessite des calculs, en fonction de l'angle d'incidence de tous les photons détectés, de l'angle Compton dans le diffuseur et de la direction des électrons diffusés. Dans sa forme la plus simple, la réponse du système à un événement est décrite par une conique, intersection du cône Compton et du plan dans lequel l'image est reconstruite. Une forte corrélation a été observée entre l'image de la source gamma reconstruite et la position du pic de Bragg. Les performances du système IHT dépendent du détecteur, en termes d'efficacité de détection, de résolution spatiale et énergétique, du temps d'acquisition et de l'algorithme utilisé pour reconstituer l'activité de la source de rayons gamma.

L'algorithme de reconstruction de l'image a une importance fondamentale. En raison du faible nombre de photons mesurés (statistique de Poisson), des incertitudes induites par la résolution finie en énergie, de l'effet Doppler, des dimensions limitées et des artefacts générés par l'algorithme itératif MLEM, les images IHT reconstruites sont affectées d'artefacts que l'on regroupe sous le terme 'bruit'. Ce bruit est variable dans l'espace et dépend du signal, ce qui représente un obstacle majeur pour l'extraction d'information. Ainsi des techniques de dé-bruitage ont été utilisées. Une stratégie de régularisation de l'algorithme MLEM (WREM) en mode liste a été développée et appliquée pour reconstruire les images Compton. Cette proposition est multi-résolution sur une base d'ondelettes orthogonales. A chaque itération, une étape de seuillage des coefficients d'ondelettes a été intégrée. La variance du bruit a été estimée à chaque itération par la valeur médiane des coefficients de la sous-bande de haute fréquence. Cette approche stabilise le comportement de l'algorithme itératif, réduit l'erreur quadratique moyenne et améliore le contraste de l'image.

Mots-clés: Hadronthérapie, rayons gamma, imagerie Compton, reconstruction d'image, algorithme MLEM, ondelettes.

Abstract

A novel technique for radiotherapy - hadron therapy - irradiates tumors using a beam of protons or carbon ions. Hadron therapy is an effective technique for cancer treatment, since it enables accurate dose deposition due to the existence of a Bragg peak at the end of particles range. Precise knowledge of the fall-off position of the dose with millimeters accuracy is critical since hadron therapy proved its efficiency in case of tumors which are deep-seated, close to vital organs, or radio-resistant.

A major challenge for hadron therapy is the quality assurance of dose delivery during irradiation. Current systems applying positron emission tomography (PET) technologies exploit gamma rays from the annihilation of positrons emitted during the beta decay of radioactive isotopes. However, the generated PET images allow only post-therapy information about the deposed dose. In addition, they are not in direct coincidence with the Bragg peak.

A solution is to image the complete spectrum of the emitted gamma rays, including nuclear gamma rays emitted by inelastic interactions of hadrons to generated nuclei. This emission is isotropic, and has a spectrum ranging from 100 keV up to 20 MeV. However, the measurement of these energetic gamma rays from nuclear reactions exceeds the capability of all existing medical imaging systems. An advanced Compton scattering detection method with electron tracking capability is proposed, and modeled to reconstruct the high-energy gamma-ray events. This Compton detection technique was initially developed to observe gamma rays for astrophysical purposes. A device illustrating the method was designed and adapted to Hadron Therapy Imaging (HTI). It consists of two main sub-systems: a tracker where Compton recoiled electrons are measured, and a calorimeter where the scattered gamma rays are absorbed via the photoelectric effect. Considering a hadron therapy scenario, the analysis of generated data was performed, passing trough the complete detection chain from Monte Carlo simulations to reconstruction of individual events, and finally to image reconstruction. A list-mode Maximum-Likelihood Expectation-Maximization (MLEM) algorithm was adopted to perform image reconstruction in conjunction with the imaging response, which has to depict the complex behavior of the detector. Modeling the imaging response requires complex calculations, considering the incident angle, all measured energies, the Compton scatter angle in the first interaction, the direction of scattered electron (when measured). In the simplest form, each event response is described by Compton cone profiles. The shapes of the profiles are approximated by 1D Gaussian distributions. A strong correlation was observed between pattern of the reconstructed high-energy gamma events, and location of the Bragg peak.

The performance of the imaging technique illustrated by the HTI is a function of the detector performance in terms of detection efficiency, spatial and energy resolution, acquisition time, and the algorithms used to reconstruct the gamma-ray activity. Thus beside optimizations of the imaging system, the applied imaging algorithm has a high influence on the final reconstructed images. The HTI reconstructed images are corrupted by noise due to the low photon counts recorded, the uncertainties induced by finite energy resolution, Doppler broadening, the limited model used to estimate the imaging response, and the artifacts generated when iterating the MLEM algorithm. This noise is spatially varying and signal-dependent, representing a major obstacle for information extraction. Thus image de-noising techniques were investigated. A Wavelet based multi-resolution strategy of list-mode MLEM Regularization (WREM) was developed to reconstruct Compton images. At each iteration, a threshold-based processing step was integrated. The noise variance was estimated at each scale of the wavelet decomposition as the median value of the coefficients from the high-frequency sub-bands. This approach allowed to obtain a stable behavior of the iterative algorithm, presenting lower mean-squared error, and improved contrast recovery ratio.

Keywords: Hadron therapy, gamma rays, Compton imaging, image reconstruction, MLEM algorithm, wavelets.

Contents

List of Abbreviations

ARM	:	**A**ngular **R**esolution **M**easure
ART	:	**A**lgebraic **R**econstruction **T**echniques
C-SPRINT	:	**C**ompton-**S**ingle **P**hoton **RIN**g **T**omograph
COMPTEL	:	**COMP**ton **TEL**escope
CsI(TI)	:	**C**esium **I**odide doped with **T**hallium
CT	:	**C**omputed **T**omography
DWT	:	**D**iscrete **W**avelet **T**ransform
ENLIGHT	:	**E**uropean **N**etwork for **R**easearch in **L**ight **I**on **T**herapy
ETOILE	:	**E**space de **T**raitement **O**ncologique par **I**ons **L**égers dans le cadre **E**uropéen
GSI	:	**G**esellschaft für **S**chwer**I**onenforschung
HCL	:	**H**arvard **C**yclotron **L**aboratory
HIMAC	:	**H**eavy **I**on **M**edical **A**ccelerator in **C**hiba
HTI	:	**H**adron **T**herapy **I**maging
IMR	:	**I**ntensity **M**odulated **R**adiotherapy
$LaBr_3$	:	**La**nthanum **Br**omide
LET	:	**L**inear **E**nergy **T**ransfer
MAP	:	**M**aximum **A** **P**osterior
ME	:	**M**aximum **E**ntropy
MEGA	:	**M**edium **E**nergy **G**amma-ray **A**stronomy
MGH	:	**M**assachusetts **G**eneral **H**ospital
MLEM	:	**M**aximum-**L**ikelihood **E**xpectation-**M**aximization
MRI	:	**M**agnetic **R**esonance **I**maging
NaI	:	Sodium (**Na**trium) **I**odide
PET	:	**P**ositron **E**mission **T**omography

PMMA	:	**P**oly**M**ethyl **M**eth**A**crylate
PMT	:	**P**hoto**M**ultiplier **T**ube
RBE	:	**R**elative **B**iological **E**ffectiveness
SOBP	:	**S**pread **O**ut **B**ragg **P**eak
SPD	:	**S**catter **P**lane **D**eviation
SPECT	:	**S**ingle **P**hoton **E**mission **C**omputed **T**omography
TIGRE	:	**T**racking and **I**maging **G**amma **R**ay **E**xperiment
WREM	:	**W**avelet **R**egularized **EM**

Introduction

Les principales motivations d'un examen par imagerie médicale sont le diagnostic, ou la confirmation du diagnostic, ainsi que la surveillance de l'évolution d'une maladie et de l'action de son traitement. L'une des applications de l'imagerie dans le suivi du traitement est le contrôle de la qualité de la radiothérapie.

L'hadronthérapie est une technique de radiothérapie très efficace contre le cancer. Elle utilise un faisceau de particules chargées, par exemple, des protons ou des ions carbone. L'hadronthérapie a prouvé son efficacité en cas de tumeurs difficiles à traiter par radiothérapie conventionnelle, du fait de leur radiorésistance, de leur profondeur, ou de leur proximité d'organes vitaux. Le faisceau d'hadrons permet d'obtenir un dépôt très localisé de la dose létale en un point dit 'pic de Bragg', à la fin du trajet des particules. L'exploitation de cet avantage nécessite un strict contrôle de la position du pic de Bragg.

Un centre d'hadronthérapie sera implanté à Lyon en 2013: projet ETOILE (Espace de Traitement Oncologique par Ions Légers dans le cadre Européen) [Pommier et al., 2002]. Ce centre sera un pôle à vocation nationale et européenne. Une première exploitation de l'hadronthérapie en Europe est le projet expérimental du GSI (Gesellschaft für Schwerionenforschung), à Darmstadt en Allemagne [Crespo et al., 2001]. Plus récemment, un établissement hospitalier a été construit à Heidelberg. Plusieurs autres projets sont en cours en Autriche, en Italie, en Espagne, en Suède. (Selon ENLIGHT: European Network for Reasearch in Light Ion Therapy).

Le succès de l'hadronthérapie dépend de toute la chaîne médicale associée au traitement: diagnostic, planification, irradiation, vérification de la qualité du traitement. Les données initiales du plan de traitement sont composées par des images de la cible (tumeur) acquises à l'aide de plusieurs techniques d'imagerie médicale et les données décrivant le faisceau d'irradiation. Le plan de traitement comprend principalement: le calcul de la distribution de dose dans la cible ainsi que dans les régions voisines, le choix et la validation de la technique d'irradiation, comme par exemple, l'estimation du nombre de directions du faisceau entrant. La phase d'irradiation emploie habituellement une méthode de livraison fractionnée de la dose [Parodi, 2004]. La méthode de vérification de la qualité de l'irradiation doit assurer la possibilité de contrôler la position du pic de Bragg et de détecter les écarts entre le dépôt de dose réel et prévu. Nos travaux se concentreront sur ce dernier aspect, c'est-à-dire les techniques de surveillance permettant de vérifier la qualité de l'irradiation, en considérant les hadrons les plus légers : les protons. Une méthode de vérification consiste à mesurer les rayons gamma secondaires issus des réactions nucléaires au cours de l'irradiation du volume cible. Le spectre d'énergie de ces rayons gamma nucléaires s'étend de 100 keV à plus de 20 MeV, ce qui constitue une difficulté majeure, rendant impossible leur détection par les dispositifs d'imagerie médicale existants. Nous proposons une nouvelle technique d'imagerie basée sur la diffusion Compton.

Les modalités d'imagerie médicale diffèrent principalement par la nature des rayonnements utilisés pour imager l'objet à étudier. En tomographie par transmission (Computed Tomography CT), on utilise des rayons X. Ils sont atténués au sein du milieu traversé. La médecine nucléaire, comme par exemple, la tomographie par émission de positons (TEP), ou la tomographie d'émission monophotonique (SPECT), utilise des radio-isotopes qui sont des sources de rayons gamma. Une image de la répartition spatiale de l'atténuation du rayonnement ou de l'intensité de celui-ci, est reconstruite, respectivement, pour ces modalités. Par conséquent, ces modalités d'imagerie nécessitent la résolution d'un problème

inverse. Plusieurs aspects doivent être pris en compte en imagerie nucléaire, la nature du rayonnement, ses propriétés et ses interactions dans les milieux (tissus) traversés. Par conséquent, tous les processus physiques intervenant dans l'émission et la détection des rayonnements considérés (par exemple, les rayons gamma), ainsi que les particules secondaires (par exemple, les électrons), doivent être pris en compte. Les principales interactions intervenant en hadronthérapie sont présentées dans le premier chapitre.

En médecine nucléaire, deux approches sont généralement mises en oeuvres. La tomographie par émission de positons (TEP) utilise des sources qui émettent des photons dans une configuration connue a priori. Des positons s'annihilent avec des électrons de leur voisinage, ce qui entraîne la production de deux photons gamma de 511 keV dans des directions opposées. La détection des ces deux photons permet la localisation de leurs émissions sur une droite. En SPECT, des détecteurs avec collimateurs rend possible la localisation directionnelle, en ne comptant que les photons qui sont dans la direction de l'entrée des collimateurs. La caméra est déplacée autour du patient, on obtient ainsi une série de projections. Une perte importante de sensibilité est acceptée pour connaître la direction des photons, il en résulte une faible qualité des images. Un accroissement du temps d'acquisition permet un comptage plus important au prix d'artefacts liés au mouvement des organes.

La détection de photons par le processus de diffusion Compton a été introduite dans le contexte de l'imagerie des rayons gamma pour améliorer l'efficacité et la sensibilité de détection. Des détecteurs basés sur la diffusion Compton sont utilisés pour des applications médicales, astrophysiques, industrielles et environnementales. La première utilisation de l'effet Compton pour la détection de rayons gamma a été proposée par [Schönfelder et al., 1973] en astrophysique. Dans le contexte médical, [Todd et al., 1974] ont proposé des technologies basées sur une caméra Compton. Plusieurs inconvénients de ce détecteur ont été montrés. L'un des problèmes rencontrés est l'estimation de l'ordre des événements Compton. Une première caméra Compton pour SPECT a été proposée par [Singh and Doria, 1983a]. Le prototype de cet appareil se composait de deux éléments. Un détecteur, où les photons incidents sont diffusés par l'effet Compton et où l'énergie de l'électron diffusé ainsi que ses positions d'interaction sont mesurées. Un calorimètre, où le photon diffusé est absorbé par l'effect photoélectrique. L'énergie des photons entrants peut être inférieure au seuil de détection, et, d'autre part, une absorption incomplète peut avoir lieu. Les solutions proposées optimisent la géométrie de détection et les matériaux des deux détecteurs. Par exemple, l'augmentation du nombre de détecteurs peut constituer une solution. Dans ce cas, un algorithme doit reconstituer le chemin de chaque photon dans les détecteurs. Le deuxième chapitre de la thèse présente les principaux détecteurs de rayons gamma, en fonction leur énergie.

Les détecteurs basés sur l'effet Compton doivent avoir une haute résolution énergétique afin d'obtenir une résolution angulaire précise car l'énergie et l'angle d'arrivée d'un photon sont liés par l'équation de diffusion Compton qui est utilisée dans l'estimation de cet angle. Un événement Compton est décrit par un vecteur qui représente les positions d'interactions mesurées, l'énergie déposée, la direction du rayon gamma diffusé (ou des directions, en cas de diffusions Compton multiples). Le processus de mesure de données Compton d'un détecteur de géométrie complexe est modélisé par la réponse du système d'imagerie à un photon d'entrée. Il dépend de l'angle d'incidence du photon d'entrée, des énergies mesurées, de la direction de l'électron diffusé, de l'angle de diffusion Compton dans la première interaction. Ainsi, chaque événement Compton mesuré a une grande influence sur la résolution de l'image initiale qui sera utilisée pour la reconstruction de l'image finale. La Section 5.1 de la thèse explique comment l'image initiale est générée. La transformation des données, de l'espace des événements à l'espace de l'image, doit calculer la probabilité qu'un événement détecté a été émis par le point de l'image reconstruite correspondant. Géométriquement, ces données rétro-projetées dans l'espace de l'image représentent des cônes, dans les directions d'incidences possibles des photons. Considérant un plan parallèle au détecteur, situé à une distance donnée, l'intersection de ce plan avec le cône génère des 'traces' (ces courbes sont des coniques, en termes géométriques) des événements Compton.

Un algorithme doit reconstruire l'image en trois dimensions (3D) à partir des rétroprojections dans

chaque plan. Cet algorithme apporte la solution du problème inverse associé. Des algorithmes ont été proposés dans la littérature visant à trouver une solution optimale de ce problème inverse. Ils sont présentés dans le Chapitre 3. Deux approches sont possibles: déterministes et statistiques (itératives). Les approches statistiques itératives présentent plusieurs avantages sur leurs homologues déterministes. En effet, elles permettent d'inclure, plus facilement, un modèle de l'émission et du processus de détection. L'application d'une méthode statistique nécessite plusieurs choix, comme par exemple, le modèle statistique des mesures, la fonction de coût, l'algorithme itératif. Le paramètre d'estimation, ou de la fonction de coût, peut être le critère du maximum de vraisemblance (ML), sa version pénalisée, ou dans le cadre Bayésien, l'estimation par maximum a posteriori (MAP). Les algorithmes itératifs les plus utilisés sont l'algorithme d'estimation-maximisation (EM), ses versions améliorées, comme par exemple, EM ordonné en sous-ensembles, bloc-itératif EM, EM alterné. L'analyse des performances inclut l'évaluation de la résolution spatiale (par exemple, la préservation des bords), les propriétés du bruit ainsi que la performance de détection. En général, les images reconstruites, en utilisant des méthodes purement basées sur le critère ML, présentent des artefacts qui se propagent au cours des itérations. Un des inconvénients de l'utilisation de l'estimateur pénalisé ML est le choix subjectif du paramètre de pénalité. Les méthodes de réduction du bruit portent sur différentes règles d'arrêt des itérations, l'application des techniques de régularisation, l'intégration d'une information préalable sur la source ou sur le système de détection. Des approches de reconstruction analytique ainsi que des approches itératives déterministes ont été proposées. Les solutions analytiques ont été obtenues en termes de transformations intégrales, harmoniques sphériques, cependant des restrictions sur les projections Compton sont introduites. Néanmoins, les méthodes analytiques sont importantes pour la compréhension qu'elles apportent au problème de reconstruction Compton. Les approches itératives peuvent être considérées comme des processus en deux étapes: estimation de la réponse du système d'imagerie, suivie par l'application d'un algorithme itératif. Cette vision de deux étapes de la reconstruction itérative de données Compton est adoptée dans ce mémoire.

Comme il a été mentionné précédemment, l'une des motivations de l'imagerie médicale est la surveillance d'un traitement. La mesure des rayons gamma provenant des réactions nucléaires d'hadrons dans la cible est un moyen de satisfaire cette exigence. Les systèmes actuels, tels que le système TEP en faisceau proposée par [Parodi et al., 2002], exploitent les rayons gamma en coïncidence de 511 keV de l'annihilation de positons émis lors de la désintégration du produit des isotopes radioactifs. Toutefois, le faible nombre d'isotopes générés qui subissent une désintégration beta, et leur temps de décroissance exigent un temps d'acquisition de données assez long. Par conséquent, il ne donne qu'une information post-traitement sur le lieu où la dose a été déposée. Contrairement aux scanners TEP conventionnels, la TEP en faisceau a un angle de couverture limité en raison de la 'gantry', ce qui réduit la précision. En outre, l'activité de positrons créés par les interactions nucléaires subit des processus métaboliques et est lavée par le flux sanguin.

Le but ultime est de surveiller l'emplacement du dépôt de la dose en temps réel et en 3D. Une méthode plus favorable pour atteindre cet objectif est la mesure du spectre complet des rayons gamma émis lors de l'interaction du faisceau d'hadrons avec la cible. Cela inclue les rayons gamma nucléaires qui sont émis par la relaxation des noyaux produits. Cette émission est isotrope et son spectre d'énergie se situe de 100 keV à plus de 20 MeV. Elle est accompagnée par un fond plus énergique de neutrons. Une relation entre la distribution spatiale des rayons gamma suivant les réactions nucléaires et la région de la décroissance de dose a été signalée par [Min et al., 2006] avec un faisceau expérimental de protons. Dans cette expérience, les rayons gamma nucléaires sont observés par un système de collimation qui ne compte que les photons gamma émis avec un angle de 90° par rapport à la direction du faisceau. En règle générale, en médecine nucléaire, les systèmes de détection (TEP, SPECT) sont optimisés pour les énergies en dessous de 1 MeV. Ainsi, la mesure des rayons gamma énergétiques des interactions nucléaires dépassent la capacité de tous les systèmes médicaux existants. Toutefois, les rayons gamma sont observés en astronomie, grâce à des télescopes Compton et paires positon-électrons [Zoglauer,

2005], ou avec détecteurs utilisant des micro-chambres à projection temporelle [Tanimori et al., 2004]. Ces systèmes ne nécessitent pas de collimateurs et ont un rendement élevé ainsi qu'un large champ de vue. Par conséquent, nous avons considéré que l'adaptation d'un tel système pour la vérification de la qualité d'un traitement d'hadronthérapie pourrait se révéler avantageuse.

La technique d'imagerie que nous avons proposée pour la détection des rayons gamma de haute énergie est basée sur la diffusion Compton et la possibilité de suivre l'électron diffusé [Frandes et al., 2010b]. Un instrument qui illustre cette méthode est le prototype MEGA ("Medium-Energy Gamma-ray Astronomy"). MEGA est le premier télescope combiné Compton et paires entièrement étalonné et fonctionnant avec succès, capable de mesurer les rayons gamma d'énergie de près de 400 keV à 50 MeV. Basé sur le principe de mesure du prototype MEGA, nous avons optimisé un appareil pour l'Imagerie en l'HadronThérapie (IHT). Il se compose de deux parties principales: le 'tracker' où les électrons Compton sont mesurés et le calorimètre où les rayons gamma sont arrêtés par l'effet photoélectrique. L'angle de diffusion Compton de la première interaction au sein du tracker, ainsi que les positions des deux premières interactions, permettent de localiser la direction du photon incident sur la surface d'un cône. La direction de l'électron diffusé permet de restreindre l'origine de la distribution à un segment de cône. L'analyse des données mesurées doit couvrir la chaîne complexe depuis les interactions dans le détecteur à la reconstruction de l'origine de la source. Les algorithmes utilisés pour l'analyse des données acquises par le système IHT sont décrits dans la Section 4.3.4. Ils se composent principalement d'algorithmes de reconstruction d'événements et d'images. Chacun d'eux représente une étape critique de l'analyse des données, ayant une grande influence sur le résultat final. La reconstruction des événements a pour but de reconstituer la trajectoire de chaque rayon gamma dans le détecteur aussi précisément que possible, alors que la reconstruction d'image a pour but, à la fois de lier les données de l'espace des événements à l'espace image et d'estimer l'origine de la source la plus probable.

Des calculs Monte Carlo numériques des profils de photons gamma émis dans un fantôme en PMMA sont présentés, avec le dépôt d'énergie des particules. Un scénario d'hadronthérapie à été simulé, les événements Compton enregistrés par le système IHT ont été générés au cours d'un traitement par des calculs de Monte Carlo, et, ensuite, une image a été reconstruite. L'algorithme en mode liste MLEM a été adopté pour reconstruire les images de la distribution de rayons gamma émis. L'algorithme itératif a été appliqué en conjonction avec la réponse d'imagerie. La forme la plus simple d'approximation de la réponse est une représentation par fonctions gaussiennes. Ce modèle de la réponse du système d'imagerie s'est révélé insuffisamment adapté, en particulier à la haute énergie des rayons gamma qui ne sont pas toujours complètement mesurés par le système IHT. En outre, le faible nombre de photons enregistrés ainsi que les incertitudes induites par la résolution finie en énergie, la résolution en position, et l'effet Doppler, produisent des images reconstruites bruitées à partir des événements IHT. Ce bruit est variable spatialement et dépend du signal, ce qui représente un obstacle majeur pour l'extraction d'information. De plus des artefacts sont générés lors de l'itération de l'algorithme MLEM. Afin de résoudre ces problèmes, des techniques de dé-bruitage des images ont été implémentées.

Une stratégie de régularisation de l'algorithme MLEM en mode liste, dans l'espace transformé en ondelettes orthogonales, a été développée (WREM). Une méthode efficace de débruitage utilise le seuillage des coefficients d'ondelettes (mise à zéro des petits coefficients), avec un seuil calculé en fonction du niveau de bruit estimé. Cette technique est bien formalisée pour un bruit indépendant des données dont les propriétés statistiques sont connues. Malheureusement, ces conditions ne sont pas satisfaites en imagerie Compton. Notre premier modèle suppose que les données de travail, c'est à dire, les images Compton initiales, sont représentées par le comptage d'évènements qui suivent une statistique de Poisson sans sources de bruit. L'application de la méthode proposée commence par une étape de stabilisation de la variance des données, par la transformation d'Anscombe [Frandes et al., 2009]. Cependant, si le bruit de Poisson est généralement admis pour caractériser des données de projection (comme par exemple, les données TEP/SPECT), après quelques itérations de l'algorithme de reconstruction, les données de l'espace de l'image suivent des distributions plus complexes. Notre second modèle suppose que le

bruit présent dans les données, après quelques itérations, suit une distribution gaussienne par application du théorème central limite [Frandes et al., 2010a]. Le seuillage est appliqué aux itérations suivantes et la variance du bruit est approximée à l'aide de l'estimateur empirique médian, appliqué aux coefficients d'ondelettes des sous-bandes hautes fréquences. L'évaluation de la méthode a été faite en utilisant différentes configurations de sources mono-énergétiques. Les données Compton ont été acquises par l'enregistrement des mesures produites dans une caméra Compton, qui a été conçue comme un modèle simplifié du système IHT. L'objectif principal de cette étude a été l'illustration de la performance de l'algorithme d'imagerie dans une configuration donnée du système de détection. Notre algorithme nommé WREM (Wavelets Reconstruction EM) a été appliqué pour reconstruire des sources de rayon gamma simulées. L'algorithme WREM est présenté dans la Section 5.2.3. Les conclusions de la thèse sont développées dans le Chapitre 6.

Introduction

In medical imaging, the main reasons for examination is to diagnose or confirm diagnosis as well as to monitor the progress of a disease or a treatment. A possible application in treatment monitoring is the quality assurance of radiation therapy by hadron beams, where gamma-ray imaging reveals an essential point of the treatment success.

Hadron therapy is an effective cancer treatment using charged particle beams of e.g., protons or carbon ions. Hadron therapy proved its efficiency in case of tumors which are hard to treat by conventional radiotherapy because they are radio-resistant, deep-seated, or close to vital organs. The hadron beam enables a high precision in the dose deposition due to the existence of a Bragg peak at the end of the beam range. In order to exploit this benefit, a strict control or monitoring technique of location and amount of the delivered radiation dose is extremely important.

Cancer treatment by hadron beams is an on growing technique in France, especially after the adoption of the ETOILE (Espace de Traitement Oncologique par Ions Légers dans le cadre Européen) project in 2005, to build a clinical center situated in the Rhône-Alpes region [Pommier et al., 2002]. A first attempt to exploit the advantages of hadron therapy was the experimental project from GSI (Gesellschaft für SchwerIonenforschung Darmstadt) [Crespo et al., 2001], along with the more recently hospital based facility from Heidelberg, Germany. Several other projects are on going in Austria, Italy, Spain, Sweden, according to the ENLIGHT (European Network for Reasearch in Light Ion Therapy) coordination activity.

The quality of hadron therapy depends on all the aspects involved into the treatment: the diagnostic phase, the treatment planning, the irradiation phase, and the quality verification of the treatment. The input data for the treatment plan consist of the target images acquired using several medical techniques, and data describing the irradiation beam. Mainly two operations are included in the treatment plan: the calculation of dose distribution within the target region as well as surroundings regions, and the choice and validation of the irradiation technique, e.g., estimate the number of incoming beam directions. The irradiation phase usually employs a fractional method of beam delivery by synchrotron, allowing a pulse-to-pulse variation of the beam parameters, as used at GSI [Parodi, 2004]. The quality verification method should assure the possibility to monitor the maximum beam range, verify the position of the irradiation field, and detect deviations between real and planned treatment, during the irradiation. The work herein will concentrate on the last aspect, namely the monitoring techniques enabling to verify the quality of the treatment during irradiation, considering the lightest hadron particles: the protons. A verification method is to measure the secondary gamma-rays issued from nuclear reactions during irradiation of the target volume by hadron beams. The energy spectrum of these nuclear gamma rays ranging from 450 keV up to 20 MeV constitute a real drawback, making their detection impossible by all existing medical imaging devices. Herein, a novel imaging technique based on the Compton scattering effect is proposed to measure the nuclear gamma rays during hadron therapy. Details about the proposed quality assurance solution will be further presented, after the main required notions will be introduced.

Medical imaging modalities differ mostly by the form of emanations used to generate images of the object under study. The emanations represent the physical processes involved in the measurement. In transmission Computed Tomography (CT), the emanations are represented by X-rays which are atten-

uated along interactions within the traversed medium. Nuclear medicine, e.g., Positron Emission Tomography (PET), or Single Photon Emission Tomography (SPECT) uses radio-pharmaceuticals which constitute emission sources of gamma rays. Given the measurements of emanations, an image of the spatial distribution of the object is reconstructed. Hence, medical imaging modalities are inverse problems.

Several aspects have to be in detail considered when medical images are studied. The nature of emanations as well as their properties should be known along with the interactions occurring within the traversed objects. Therefore, all physical processes involved in emission and detection of the considered emanations (e.g., gamma rays) as well as the production of subsequent particles (e.g., electrons) should be well understood. The main interaction processes related to hadron therapy are presented in the first chapter.

The issue of the detection of emerging photons is a the directional localization of their emission source. In nuclear medicine, mainly two approaches are generally underlined. PET uses sources which emit photons in a priori known configuration - positrons annihilate with electrons placed in their vicinity, resulting in generation of two 511 keV gamma photons at (almost) opposite directions. Detection of the two photons results into localization of their origin emission somewhere on the straight line determined by the positions of interaction. In SPECT, collimator based detectors achieve directional localization, counting only those photons which are directed perpendicular to the face of the camera. During detection, the collimated camera is rotated around the subject (patient), resulting in a set of collected projections. A severe loss of sensitivity is accepted to know the incoming direction of emitted photons, resulting in degraded image quality. Data collection times should not be increased to improve photon counts, thus more efficient and sensitive detection is desirable.

Photon detection by means of the Compton scattering process was introduced for gamma-ray imaging context as a solution to improve the efficiency and sensitivity of detection. Compton scattering based detectors are mainly used for medical and astrophysical applications, as well as industrial applications, e.g., non-destructive analysis of nuclear waste, environmental monitoring. The first idea of using Compton scatters for gamma-rays detection was proposed by [Schönfelder et al., 1973] for astrophysics applications. In the medical context, [Todd et al., 1974] proposed the Compton camera technologies, and several drawbacks in constructing this detectors were shown; one of them was the problem of finding the correct order of the Compton events. A Compton camera for SPECT was firstly proposed by [Singh and Doria, 1983a]. The prototype of the camera consisted of mainly two principal sub-parts which have to work in coincidence. Namely, the scattering detector where the incoming photons are Compton scattered, and the recoiled electron's energy as well as its interaction positions are measured. The scattered photon undergoes photoelectric absorption in the second detector by deposing its full energy. When the energy of the incoming photons are above a detectable threshold, incomplete absorption may be recorded. The proposed solutions tried to optimize the detector geometry as well as to improve the materials composing it. Namely, increasing the number of detectors may constitute a valuable solution in certain applications. In this case, algorithms which reconstitute the paths of incoming photons have to be available. They start by grouping the interactions into events which further are assigned to the photon tracks producing them. Finding the correct order of events belonging to a track as well as their measured information (e.g., position, energy), is an essential step in knowing if a complete absorption was recorded, and finally, to compute the source location. The second chapter of the thesis introduces the principal groups of gamma-ray detectors, which vary according to the targeted energy.

Compton detectors should have high energy resolution to allow a reasonable angular resolution. The energy and angular parameters are related via the Compton equation. A Compton event consist of a vector which represent the measured interaction positions, deposed energies, scattered gamma-ray direction (or directions, in case of multiple Compton scatterings). The Compton measurement process - in combination with a complex detector geometry - results in a multi-dimensional imaging response which depends on all measurements (e.g., incidence angle, measured energies, direction of the scattered electron, Compton scatter angle in the first interaction). Hence, each measured Compton event has a

high influence on the resolution of the initial image. Section 5.1 of the thesis explains how the initial image is generated. The transformation of data from event-space to image-space requires to compute the probability that a detected event was really emitted by the underlined image pixel. Geometrically, these data back-projected in image space correspond to a cone of possible origin directions. Considering a parallel to the detector plane, situated at a given distance, the intersection of this plane with the cone generates "shapes", or profiles of the Compton events. A profile represents the distribution of possible true event cones from the measured one, and the distribution of true scatter planes from the measured one.

An implementable algorithm has to be available for reconstructing the image from the measured emanations. This step means to find a solution to the associated inverse problem. The source function is generally defined over a 3D domain. Many algorithms were proposed in the literature aiming to find its optimal expression. Part of them are reviewed in Chapter 3. Two main approaches of image reconstruction exists, namely analytic and iterative methods. Iterative approaches present several advantages over their analytic counterparts, allowing to include into reconstruction a model of both emission and detection processes. Applying an iterative method demands to make several choices, e.g., the statistical model of measurements, the cost function, the iterative algorithm. The estimation parameter or cost function may be the maximum-likelihood (ML) criterion, its penalized version, or in the Bayesian framework, the maximum a posterior (MAP) estimate. Widely used iterative algorithms include the expectation-maximization (EM) algorithm, along with its improved versions, e.g., ordered-subsets EM, block-iterative EM, space-alternating EM. The image performance analysis includes evaluation of spatial resolution properties (e.g., edge-preserving), noise properties as well as detection performance. Generally, images reconstructed purely using methods based on ML criterion present artifacts, which propagate during iteration. Disadvantages of using the penalized ML estimator include the rather subjective choice of the penalty parameter. Methods to reduce noise include various stopping rules, application of regularization techniques, integration of a prior information about the source or detection system.

Analytical as well as iterative approaches were proposed to reconstruct Compton data. Analytical solutions were derived in terms of integral transforms, spherical harmonics, including restrictions to the Compton projections possible to use. Nevertheless they are important for the insight they bring into the Compton reconstruction problem. The iterative approache may be viewed as a two steps process: estimation of the imaging response, followed by the application of an iterative algorithm. An accurate imaging response is required when a high resolution of the final reconstructed images is needed. This two steps vision about iterative reconstruction of Compton scattered data is adopted herein.

When studying medical images, beside the required criteria introduced, an essential condition may be underlined; namely, the necessity of obtaining an image representing useful diagnostic information about the spatial distribution of the object under study.

As it was mentioned above, one reason to generate medical images is to obtain an easily to interpret way of monitoring a treatment. The measurement of gamma rays originating from nuclear reactions of the hadrons within the target volume is a way to fulfill this requirement. Current systems, such as the in-beam PET system proposed by [Parodi et al., 2002], exploit the coincident 511 keV gamma rays from annihilation of positrons emitted during the beta decay of generated radioactive isotopes. However, the low number of generated isotopes which undergo beta decay, and their decay time require quite long data acquisition times. Therefore it only gives a post-therapy information about the location of the deposed dose. Unlike conventional PET scanners, in-beam PET has limited angle of coverage due to the gantry, reducing the quantitative precision. Moreover, positron activity created by nuclear interactions undergoes metabolic processes and is washed out via the blood flow. The ultimate goal, however, is to monitor location and deposed dose of the beam in real-time in 3D. One way to achieve this goal is to measure the complete spectrum of the emitted gamma rays during the interaction of the hadron beams with the target. This includes nuclear gamma rays which are emitted by the relaxation of generated nuclei. This emission is isotropic, and its energy spectrum ranges from roughly 100 keV up to 20 MeV,

accompanied by a more energetic background of neutrons. A relation between the spatial distribution of gamma rays following nuclear reactions and the dose falloff region was reported by [Min et al., 2006] with an experimental proton beam. There, the nuclear gamma rays are observed by a collimated system counting only those gamma rays which are emitted with an 90° angle with respect to the beam direction.

In general, in nuclear medicine, the detection systems (PET, SPECT) are optimized for energies below 1 MeV. Thus the measurement of energetic gamma rays from nuclear interactions exceeds the capabilities of all existing medical systems. However, those gamma rays are a prime target for astronomical imaging systems, such as tracking Compton and pair telescopes [Zoglauer, 2005], detectors using micro time projection chambers [Tanimori et al., 2004]. Those systems do not require collimators and therefore can achieve a high efficiency and large field-of-view. Furthermore, they can use gamma ray and electron tracking to identify and thus reject a large portion of the background. Therefore, the adaptation of such a system to hadron therapy monitoring might prove advantageous.

The proposed detection technique of the high-energy gamma-rays is based on Compton scattering with the electron tracking possibility [Frandes et al., 2010b]. An instrument illustrating this method is the MEGA prototype ("Medium-Energy Gamma-ray Astronomy"). MEGA was the first fully calibrated and successfully operating combined Compton and pair telescope, capable of measuring gamma rays in the energy range from roughly 400 keV up to 50 MeV. Based on the MEGA prototype measurement principle, an advanced imaging device was optimized for Hadron Therapy Imaging (HTI) to observe gamma rays from an object. It consists of two main parts: the tracker where Compton recoiled electrons are measured, and the calorimeter where gamma rays are stopped via the photoelectric effect. The Compton scattering angle of the first interaction within the tracker, along with the positions of the first two interactions allow to localize the direction of the incoming photon on a cone surface. Including information about the recoil electron direction enables to further restrict the origin distribution to a cone segment. The analysis of measured data has to cover the complete detection chain starting from the hits into the detector to reconstructing the source image. Algorithms used for the analysis of the HTI data are described in Section 4.3.4. They mainly consist of event and image reconstruction algorithms. Each of them represents a critical step of data analysis, having both a high influence on the final results. Event reconstruction has to reconstitute the path of each gamma ray into detector as accurately as possible, while image reconstruction has to both link the data from event space to image space, and estimate the most probable source origin.

Monte Carlo numerical experiments of the emitted gamma photons profiles into a PMMA phantom are presented, along with the energy deposition of hadron particles. Considering a hadron therapy scenario, the HTI recorded Compton events were generated during the treatment by Monte Carlo calculations, and further reconstructed. A list-mode MLEM was adopted to reconstruct images of the emitted gamma-ray distribution. The iterative algorithm was applied in conjunction with the imaging response. The simplest form of response approximation, i.e., estimation by 1D Gaussian functions, was adopted herein. This model of the imaging response proved insufficiently adapted, especially to high-energy gamma-rays which are not always completely measured by the HTI system. Moreover, the low photon counts recorded as well as the uncertainties induced by finite energy, position resolution, and Doppler broadening, result in noisy reconstructed images of the HTI events. In addition, artifacts are generated when iterating the MLEM algorithm. This noise is spatially-varying and signal-dependent, representing a major obstacle for information extraction. Therefore image de-noising techniques were investigated.

A wavelet based multi-resolution strategy of list-mode MLEM regularization (WREM) algorithm was developed and applied to reconstruct Compton events. Wavelet based methods are widely used for a large range of applications. In image processing, they are mainly employed for image compression and de-noising. One of the image de-nosing methods includes a shrinkage technique of wavelet coefficients, according to an adopted policy based on the estimated noise level. An ideal application of this technique should include that the noise is data independent, and the statistical properties of the noise are known. However, in case of nuclear images, and more particularly, in case of Compton images,

these aspects are not a priori available. A first model assumes that the working data, i.e., Compton initial images, are represented by Poisson counts without any other additive noise. The application of the proposed method starts by a normalization step, which includes the data pre-processing by Anscombe transform [Frandes et al., 2009]. However, the Poisson noise is generally assumed to characterize the projection data (e.g., PET/SPECT data), whereas in the image space, after deconvolution, data could follow different, generally more complex distributions. A second model assumes that the noise present in the data follows a Gaussian distribution after a number of iterations, when considering the central limit theorem [Frandes et al., 2010a]. The thersholding is applied to the further iterations, while the noise variance is approximated as the MAD estimator using the high sub-bands wavelet coefficients. The evaluation of the method was done using different configurations of mono-energetic sources. Compton data were acquired by recording the measurements occurred on a Compton camera, which was designed as a simplified model of the HTI system. The primary aim of the study was the illustration of the imaging algorithm performance in a given configuration of detection system. The proposed method is presented in Section 5.2.3, while the Chapter 6 concludes the thesis.

Chapter 1

Fundamentals of particle physics and hadron therapy

Gamma-ray imaging appears as a necessary assess in various domains, e.g., medical imaging, astrophysics, demanding the knowledge of both gamma-rays emission and detection processes. Emission of gamma rays is strongly related to the creation medium, which is defined by e.g., its atomic number, dimensions, material. Meanwhile, detection implies the complex analysis of gamma ray properties, e.g., energy spectrum, emission time, in order to achieve an effective response to the imaging assignment. Gamma rays lose energy in a variety of ways involving liberation of atomic electrons, which further deposit the energy in interactions with other electrons. Hence, an understanding of the basic physical processes is desirable.

Imaging of gamma rays reveals as a strongly required capability of the treatment quality evaluation during radiation therapy by hadron beams. Namely, imaging of gamma rays generated during fragmentation of target nuclei constitute a verification approach that each incident beam was delivered as intended, i.e., the beam energy (or dose) was deposed according to the treatment plan. The treatment quality verification represents a fundamental issue in hadron therapy, due to the necessity of maximizing the dose delivered to the target volume (tumor), while preserving as much as possible the surrounding (healthy) regions. This aim is a critical aspect, especially for hadron therapy, where the depth-dose distribution is characterized by a relatively low dose at the entrance region, and a sharply elevated dose at the end of the range. Solutions proposed to monitor the dose deposition in hadron therapy are reviewed in Section 1.2.2.

1.1 Interaction processes

Interaction processes which occur when charged particles travel within matter, determine the loss of their energy by collision with orbital electrons, or band electrons in materials such as Silicon or Germanium. Scattering of gamma rays is a process with a wide range of possible results, following statistical distributions. Possible interaction processes vary with both particles energy, and atomic number of the material.

Gamma rays are high-energy ionizing radiation. They could depose energy in the mass of a material when passing through. A measure of the amount of energy per unit of mass is, in a general sense, named dose. Dose is affected by the type of radiation, the amount of radiation, and the physical properties of the material. Specifically, dose is referred as the absorbed dose in tissue, or a material such as Silicon, or Germanium.

The energy transferred to the medium per unit length of the ionization path is named Linear Energy Transfer (LET) . The latter is useful to indicate the quality of different types of radiation. Equal doses of different types of ionizing radiation will produce different biological effects. Generally, X-rays (e.g.,

250 kVp X-rays) are used as the reference standard to compare different types of radiation. The Relative Biological Effectiveness (RBE) is defined as D_x/D, where D_x is the X-rays reference dose, while D is the dose of test radiation which produce the same biological effect. The RBE of gamma rays and β particles is 1, for protons is 5, while for α particles and neutrons is 20, and included in the interval of $5-20$, respectively.

Particles such as α, β, positrons cause biological effects by directly ejecting an electron, while gamma rays interact with matter creating biological effects by indirect processes, e.g., scattering, pair creation. All of these processes liberate high energy electrons, which can further cause ionizations of e.g., living matter, resulting in biological changes. Generally, three consequences can occur: the change is repaired or partially repaired (case when a form of disease could appear as a result of ionizing radiation), or the change is not repaired. Section 1.1.2 presents gamma-rays interaction processes.

Often, Monte Carlo simulations are performed to calculate the interactions of particles as well as their path in different matrials, e.g., components of detector systems. The program has to compute the probability of an interaction by taking into account a large number of parameters, e.g., the atomic number, thickness and density of the interaction material, the interaction cross-section, the average distance between two interactions, i.e., the mean free path. Monte Carlo simulation programs include also description of atomic and nuclear processes for the ions transport in matter. However, the existence of realistic models for accurate description of physical processes is a critical issue.

1.1.1 Interaction of electrons

Electrons are charged particles which are scattered when they pass through a material, or lose a part or all their energy by several processes, e.g. ionization, emission of photons (e.g., bremmstrahlung), ejection of secondary electrons. In a Silicon based detector, the dominant processes are ionization at low energies, and bremmstrahlung at high energies. Electrons can interact through their Coulomb field by inelastic scattering, or Molière scattering. The latter can be described by small-angle scatterings (forward scattering). The scatter angle distribution can be approximated by a Gaussian. The width of distribution projecting it on a scatter plane is expressed by

$$\delta_{0,proj} = \frac{13.6MeV}{\beta cp}\sqrt{\frac{r}{R_0}}\left(1 + 0.038\ln\frac{r}{R_0}\right) \tag{1.1}$$

where $\beta cp = \frac{E_e^2+2E_eE_0}{E_e+E_0}$ is the velocity times the momentum of the electron, E_e is the electron energy, E_0 is the rest energy of the electron, R_0 represents the radiation length in the material, while r is the straight path length (i.e., the straight line between the start and end points) of the electron in the material.

Small-angle scatterings consitute a drawback in a particle detector, e.g., a tracking Silicon based gamma-ray system has to overcome the limits imposed by the scattering in the measurements of the electron direction. Scattering in high angles is rather unlikely, but the probability increases with increasing the atomic number of the material.

1.1.2 Interaction of gamma rays

Gamma rays can pass through matter without interaction, interacting with matter by scattering from the initial path deposing only a part of their energy, or being completely absorbed by deposing all the energy.

Gamma rays are completely absorbed either by the photoelectric effect at energies below 500 keV or, at high energy range, e.g., above 1 MeV, by emission of two particles (electron and positron), which share the energy of the gamma rays. The positron loses its energy through ionization, and interaction with an electron creating two annihilation photons with energy of 511 keV each. The latter can further escape or interact within the medium through Compton scattering or photoelectric effect.

Instead of transferring all its energy to an electron of an atom, gamma rays are Compton scattered yielding only a part of its energy to electrons, which are ejected from the orbital position. After they

continue to pass through matter along a deflected path. The lost energy depends on the scattering angle, and the nature of the scattering medium.

1.1.2.1 Photoelectric absorption

Photoelectric absorption is the process when a gamma ray interacts with a bound electron lossing all its energy by mostly transferring it as kinetic energy to the electron, which is subsequently freed from the material (Figure 1.1). The vacancy created is filled by the capture of an electron, or the rearrangement of electrons from other shells of the atom, or both. Photoelectric absorption is a desirable process for gamma-ray detection because of the full energy absorption, but it is the predominant interaction only for low-energy gamma-rays.

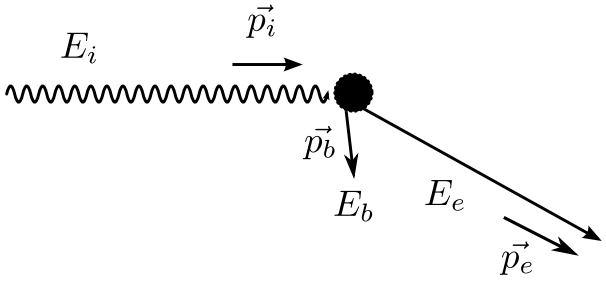

Figure 1.1: Representation of the photoelectric absorption process. A photon of energy E_i and momentum $\vec{p_i} = h/\lambda_i$ interacts with an electron causing its ejection. The vacancy is taken by an orbital electron which is generally placed at a lower orbital shell. The movement is followed by emission of a fluorescent photon.

The energy of the photo-electron E_e liberated by the interaction is given by the difference between the gamma-ray energy E_i and the electron binding energy E_b:

$$E_e = E_i - E_b \tag{1.2}$$

Generally, for most imaging detectors, the photo-electron is stopped in the active volume, which emits a small output pulse, whose amplitude is proportional to the energy deposited by the electron.

1.1.2.2 Rayleigh scattering

Rayleigh scattering process is the elastic scattering of X-rays by atomic electrons. Even if no energy change is produced between photons and the medium, the scattered X-rays undergo a change of their trajectory (Figure 1.2).

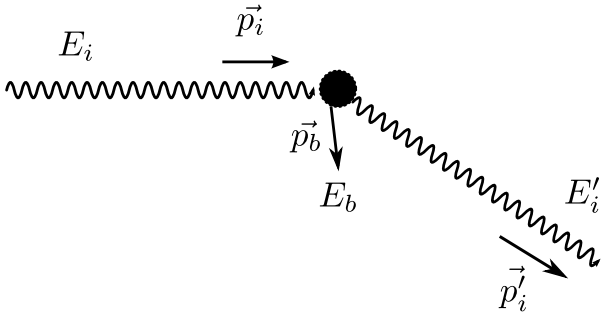

Figure 1.2: Representation of the X-ray Rayleigh scattering process. The incident X-ray is scattered by interaction with an atomic electron. The energy of the scattered X-ray E_i' is equal to the energy of the incident X-ray E_i. Rayleigh scattering is most likely at low-energy X-rays and high-Z materials.

Rayleigh scattering angles are generally small, since the atom must recoil as a whole without inducing atomic excitation or ionization. Rayleigh scattering probability increases when decreasing the photons energy.

1.1.2.3 Compton scattering

Compton scattering is the process when a photon inelastically scatters a free electron through an angle θ_g. The scattered photon leaves the interaction location, having a different direction to the incident photon,

and less energy (Figure 1.3).

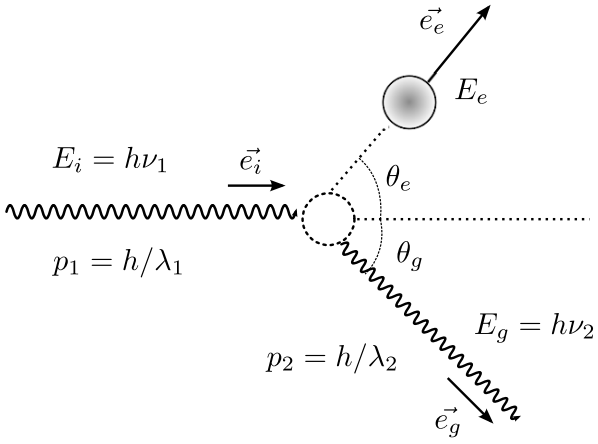

Figure 1.3: Representation of the Compton scattering process. A photon of initial momentum h/λ_1 collides an electron of mass m. The scattering angle θ_g can be derived using conservation of momentum and energy, the momentum of the scattered photon h/λ_2, the recoil electron mass, and the initial momentum. E_g is the scattered gamma-ray energy, while E_e is the energy of the recoiled electron.

Considering the theoretical assumption of an bound electron which is at rest, and the conservation of both energy and momentum [1], the Compton scattering equation can be formulated as the following:

$$\lambda_2 - \lambda_1 = \frac{h}{mc}(1 - \cos\theta_g) \tag{1.3}$$

The photon of initial wavelength λ_1 and energy ν_1 is scattered through an angle θ_g, and further, the photon wavelength is λ_2, and the energy is ν_2. The parameter h denotes the Plank's constant, while mc^2 is the electron rest energy.

Considering

$$\alpha = \frac{h\nu_1}{\mathrm{mc}^2} \tag{1.4}$$

the equation which relates the scattering angle to the change of energy $\Delta E = h\nu_2 - h\nu_1$ of the photon can by approximated by the formula:

$$\Delta E = \frac{h\nu_1(1 - \cos\theta_g)}{1/\alpha + 1 - \cos\theta} \tag{1.5}$$

$$\cos\theta_g = 1 - \frac{\Delta E}{(h\nu_1 - \Delta E)\alpha} \tag{1.6}$$

The Compton equation 1.6 can be rewritten

$$\cos\theta_g = 1 - \frac{E_0}{E_g} + \frac{E_0}{E_g + E_e} \tag{1.7}$$

where $E_0 = \mathrm{mc}^2$, E_g is the scattered gamma-ray energy, while $E_e$is the recoil electron energy.

For a mathematically valid Compton angle, the following restrictions have to be verified:

$$\frac{E_0 E_i}{2E_i + E_0} < E_g < E_i \tag{1.8}$$

$$0 < E_e < \frac{2E_i^2}{2E_i + E_0} \tag{1.9}$$

The photon is back-scattered when its energy attains the minimal value, while no scattering takes place when $E_i = E_g$.

[1] postulated by Arthur H. Compton

The equations related to the scatter angle θ_e of the recoil electron, and the total angle $\theta = \theta_g + \theta_e$ between the scattered photon and recoil electron are approximated by the following:

$$\cos\theta_e = \frac{E_e(E_i + E_0)}{E_i\sqrt{E_e^2 + 2E_eE_0}} \tag{1.10}$$

$$\cos\theta = \frac{E_e(E_g - E_0)}{E_g\sqrt{E_e^2 + 2E_eE_0}} \tag{1.11}$$

For a given initial energy E_i, θ_e takes values between 0° (back-scattering), and 90° (forward scattering) where $E_e = 0$. When no energy is transferred to the electron, θ is equal to 90°. In the case of back-scattering, θ is equal to 180°.

In reality, the electrons are in motion around the nucleus, thus the measured energy does not reflect only one scattering angle, but various angles around it. This effect of electrons results in Doppler broadening. Influencing the energy spectra of photons, Doppler broadening limits the accuracy obtained when the Compton scattering angle is measured.

The Compton collision cross-section σ_c determines the probability that an incident photon will undergo a Compton scatter. Considering n_e electrons per unit volume, a photon beam of intensity Φ incident on a material of thickness dx verifies the following equation:

$$d\Phi = -\Phi n_e \sigma_c dx \tag{1.12}$$

The number of photons scattered by unit volume is directly proportional to the beam intensity, the number of photons per unit volume, and the Compton cross-section:

$$\frac{dN}{dV} = -\frac{d\Phi}{dx} = \Phi n_e \sigma_c \tag{1.13}$$

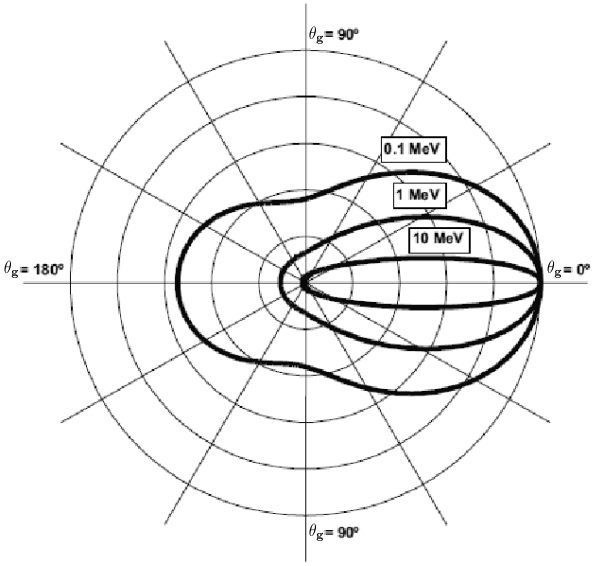

Figure 1.4: Illustration of the angular dependence of the Compton cross-section on photons energy: At higher energy, the average Compton scattering angle is smaller resulting in stronger forward scattering.

The Klein-Nishina equation of differential Compton cross-section $\frac{d\sigma_c}{d\Omega}$ for unbound electrons can be approximated by the following formula:

$$\frac{d\sigma_c}{d\Omega} = \frac{r_e^2}{2}\left(\frac{E_g}{E_i}\right)^2\left(\frac{E_g}{E_i} + \frac{E_i}{E_g} - \sin^2\theta_g\right) \tag{1.14}$$

Klein-Nishina cross-section as a function of the Compton scattering angle θ_g from 0.1, 1, and 10 MeV photons is illustrated in Figure 1.4. When considering bound electrons, i.e., the Doppler broadening effect, a more complex expression of Compton cross-section is required. One expression has been derived by [Ribberfors, 1975]

$$\left(\frac{d\sigma_c}{d\Omega}\right)_{bound} = \frac{d\sigma_c}{d\Omega} \cdot S_i(E_i, \theta_g, Z) \tag{1.15}$$

where S_i denotes the incoherent scattering function [Ribberfors and Berggren, 1982] of the ith shell of electrons, and Z is the atomic number of the scattering material.

1.1.2.4 Pair production

A photon can create an electron-positron pair when its energy is at least 1.022 MeV, and is situated in the presence of the electric field of a nucleus (Figure 1.5). After losing its kinetic energy, the positron interacts with an electron in an annihilation process, which will release two gamma rays with equal energy of 0.511 MeV. These gamma rays can further interact with the absorbing material, or escape.

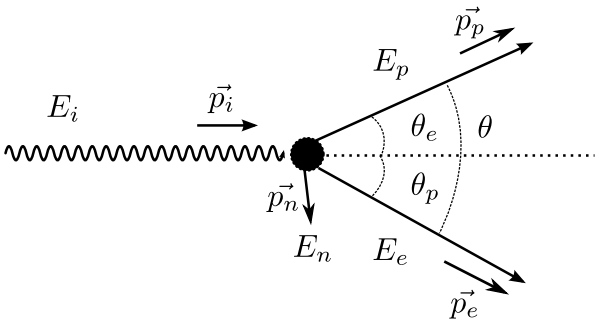

Figure 1.5: Representation of the pair production process. A photon of energy E_i passing nearly to an atomic nucleus (or electron) of energy E_n is converted into an electron pair of positive and negative charge. Later, the positron could interact with an orbiting electron, and two annihilation photons of almost opposite directions are emitted.

The pair production process is described by the following equations of energy and momentum conservation:

$$E_i = E_e + E_p + E_n + 2E_0 \tag{1.16}$$

$$\vec{p_i} = \vec{p_e} + \vec{p_p} + \vec{p_n} \tag{1.17}$$

When the photon energy exceeds four times the rest mass of electron, pairs can also be created in the field of an electron. In this case, the momentum is transferred to the electron instead of nucleus. The recoil of the electron could produce signatures in a detector, being presumably possible to measure by a detector. For one atom with Z electrons, the probability relation for pair production on an electron and nucleus can be expressed by

$$p_{\text{electron}} = \frac{1}{CZ} p_{\text{nucleus}} \tag{1.18}$$

where Z is the atomic number (e.g., $Z = 14$ for Silicon), and C represents a factor which depends on the gamma-ray energy (C is close to 1 when $E_i >> 4m_e c^2$).

In a detector, the pair creation is a predominant process when the energy of incident photon exceeds an energy threshold, or when the material consists of high-Z elements. The path of the pair created depends on both the energy of photons, and the dimension of detector.

1.1.3 Interaction of heavy charged particles

Heavy charged particles passing though matter interact mainly with electrons by Coulomb inelastic collisions. At high initial energy, the interactions are short and just a slight amount of energy is transfered.

Increasing the depth, the particles are slowed down, and the mean energy transfer during collisions with electrons become large, transferring a higher dose to medium. Thus, the dose increases at the end of their path to high values attaining a maximum point, called Bragg peak. Afterwards the dose decreases when the range of particles reaches its end. Hence, the description of heavy charged particles travelling in a medium may be viewed as a continuously slowing down process at an energy loss rate mainly given by the electronic stopping power.

The equation of electronic stopping power is described by the Bethe-Bloch formula:

$$-\frac{dE}{dx} = 2\pi r_e^2 m_e c^2 N_{e^-} \frac{Z^2}{\beta^2}\left[ln\left(\frac{2m_e c^2 W_{max}\beta^2}{I^2(1-\beta^2)}\right) - 2\beta^2 - 2\frac{C}{Z_t} - \lambda\right] \tag{1.19}$$

where Z is the particle charge, and β its velocity; r_e and m_e are the electron radius and its mass, respectively. W_{max} is the largest possible energy loss in a single collision with an electron, while N_{e^-} and I are the electronic density and ionization potential of the medium with the atomic number Z_t. The parameters C and λ denote the energy and absorber dependent shell and density corrections, respectively.

The particle mean range R for a given initial energy E_0 can be approximated by the following:

$$R = \int_{E_0}^{0}\left(\frac{dE}{dx}\right)^{-1} dE \tag{1.20}$$

Interactions which result in energy deposition may occur randomly giving statistical fluctuations of their number as well as the transfered energy in each interaction. The latter is known as energy straggling, or range straggling. The deposed energy is rather independent of the traversed medium composition, but is rather sensitive to its density.

Atomic nucleus can be at a moment in a ground state or in an exited state. The latter may be acquired by an addition of energy to the nucleus. The emission of this excess of energy can be done by electromagnetic radiation, i.e., emission of gamma rays within rather nanoseconds. The energy can also be transferred to one of inner electrons, which will have enough energy to leave the atom. This process is called internal conversion.

1.1.3.1 Nuclear reactions

Heavy charged particles deposit energy through interactions with atomic electrons or nuclei. Possible nuclear interactions induced by, e.g., protons, are both elastic or inelastic processes, which include nuclear capture and nuclear scattering.

Nonelastic nuclear interactions occur at higher particle energies and produce secondaries, e.g., protons, neutrons, beta particles, and gamma rays. These secondary particles usually stop in the vicinity of the interaction presenting high RBE. The secondaries as well as the fragments produced in nuclear reactions could influence the spatial dose profile of distribution. The fragmentation reaction represents the dominant interaction in the high energy interval, e.g., 60-250 MeV for protons. Other nuclear reactions are small angles Multiple Coulomb scattering, and large elastic nuclear collisions.

The attenuation in depth of flux distribution particle follows the equation [Knoll, 2000]

$$\Phi(x) = \Phi_0 e^{-\mathcal{N}\sigma_R x} \tag{1.21}$$

where σ_R is the reaction cross-section, while Φ_0 and $\mathcal{N}$ are the initial flux, and the atomic density, respectively. Hence, the dose delivered by the primary particle is reduced with increasing the depth.

Nuclear fragmentation is a complex process where exited fragments are produced within $\simeq 10^{-22}$ s in the collisions, which are followed by nuclear evaporation, and photon emissions in about $\simeq 10^{-21} - 10^{-16}$ s. For protons, mostly target fragmentation is possible. For heavier ions, the fragmentation products to generation of secondary particles along the beam path. The latter travel mostly forward and could determine further interactions, thus undesirable dose deposition beyond the Bragg peak could appear.

In addition, the emission of fragments results in a larger lateral spread of the beam, especially near the Bragg peak. Hence, the nuclear fragmentation reactions may contribute to modifications of the longitudinal and transversal dimension of the deposed dose.

1.1.3.2 Gamma rays following nuclear reactions

Heavy charged particles traveling through matter lose their energy by ionization and nuclear interactions with the nuclei of the medium. Besides others, the interactions lead to (delayed) beta decays, which are radioactive decays with the emission of either an electron and an electron anti-neutrino (β^- decay) or a positron and an electron neutrino (β^+ decay). If the resulting nucleus is in an excited state, its de-excitation is usually accompanied by gamma-ray emission. The emission of these secondary photons occurs usually within an extremely short time span (e.g., pico-seconds), and the photons have a characteristic energy reflecting the energy level structure of the de-exited nucleus. Since nuclear states present well-defined energies, the energy of the emitted gamma rays are also specific. For example, when a product nucleaus such as ^{12}C is in an exited state, it has a lifetime of 64 fs, and its decay gives rise to a gamma ray of 4.4 MeV energy. When ^{16}O is in exited state, gamma rays of 6.13 MeV are emitted, presenting a life-time of 2×10^{-11} s [Knoll, 2000].

Section 4.2 presents Monte Carlo calculations of the origin location of secondary gamma rays emitted during the first second of a PMMA phantom irradiation by proton beams at different energies. A correlation between the lateral profiles of dose deposition and the gamma rays was observed. A special characteristic of these gamma rays is their energy spectrum, which ranges from roughly 450 keV up to 20 MeV.

1.2 Hadron therapy

Conventional radiation therapy is the use of radiation in cancer treatment. Generally, its application relies on cases where other treatment techniques failed, with the limitation given by the risk of radiation-induced cancers. Before the therapy, a detailed plan of dose to be delivered is analyzed and computed considering all the parameters involved, e.g., tumor type, location, stage, uncertainties of internal or external movement. Several angles of exposure which intersect the tumor are considered to preserve as much as possible the health tissue. A generally used technique is to fraction the dose over the time for allowing the normal cells to recover, and the tumor cells which are in a radio-resistance phase to become more treatment sensitive. However, an optimal treatment approach has to include the capability of both localization and tracking the beam in order to ensure a high quality assurance.

Radiation therapy improved the clinical results by using modern high-energy ($4 - 20$ MeV) linear accelerator, which can deliver irradiation from different directions. The innovative technique of Intensity Modulated Radiotherapy (IMR) allows a non-uniform photon flux delivery. Despite the advances, the therapeutic effectiveness is limited by the physical and biological properties. The lateral depth dose profile of photons restrict the irradiation precision of tumors situated close to vital organs, or radioresistant.

Heavy charged particles, e.g., hadrons (protons, carbon ions), may overcome the limitations of photon irradiation by a more precise and selective energy deposition. Figure 1.6 illustrates comparatively the depth dose profiles generated by photon and proton beams.

The application of protons for radiation therapy was first suggested by R. Wilson in the 1946 while working at the design of the Harvard Cyclotron Laboratory (HCL) . The large mass of the proton would minimize lateral scattering, and the energy deposition pattern would allow to place the maximum dose within the tumor, and thus providing maximal sparing of the health tissues. Two years after, the cyclotron at the Lawrence Berkeley Laboratory became available for physics and radio-biological investigations in preparation for clinical use.

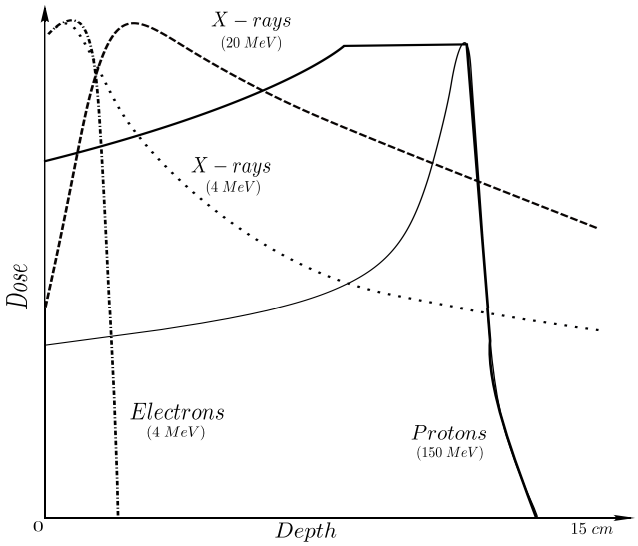

Figure 1.6: Illustration of depth dose profiles of photons with different radiation sources (discontinuous lines), and protons (continuous lines). Protons depose the energy in a relatively low constant dose which ends by a sharp peak. The modulation of energy particles forms a region referred as Spread Out Bragg Peak (SOBP). A uniform biological dose distribution within the SOBP region can be obtained by varrriation in RBE of irradiation as a function of depth.

The first treatments were performed at the particle accelerators built for physics research at Berkeley Radiation Laboratory in 1954, and at Uppsala in Sweden, in 1957. Meanwhile, in 1961, a collaboration began between the HCL and the Massachusetts General Hospital (MGH) to use the proton beam as a neurosurgical tool for treatment. In the early 1970s, progresses were made by the developments of new techniques for eye tumors. Also at MGH in Boston, a large-field fractionated radiation treatment program was initiated for brain tumors including tools for three-dimensional treatment planning. The first hospital based center for proton therapy was established in 1990 at the Loma Linda University Medical Center, USA, and the Heavy Ion Medical Accelerator in Chiba (HIMAC), Japan. Since then, new facilities have been growing worldwide [Sisterson, 2005]. Due to the rather higher complexity and costs of ion therapy, most of the centers adopted the lightest ion particle, proton, which offers superior biological effectiveness than conventional techniques.

The German project at the Gesellschaft für SchwerIonenforschung Darmstadt (GSI) is a pilot project of an experimental carbon ion therapy since 1997, which attempts to demonstrate the clinical application of the therapy technique [Crespo et al., 2001]. GSI uses a three-dimensional beam delivery based on a two-dimensional intensity controlled raster scanning in combination with active energy variation from the accelerator ($88-430$ AMeV), treatment planning, and therapy monitoring by means of in-beam Positron Emission Tomography (PET) [Parodi et al., 2002]. Recently, a new hospital-based ion beam facility was built in Heidelberg. Various beams, e.g., protons, oxygen ions, are studied in order to investigate their clinical impact. Several European projects dedicated to ion beam facilities are nowadays ongoing.

In order to exploit the benefits of hadron particle therapy, an accurate control of delivered dose location is hightly demanded. The measurement of gamma rays originating from nuclear reactions of the hadrons within the body is a way to fulfill this requirement. The currently available systems, e.g., in-beam PET, exploit the coincident 511 keV gamma rays from annihilation of positrons emitted by some of the nuclear fragments. The low number of positron emitting fragments and their decay time require slightly long acquisition times, i.e., on the order of tens minutes, and thus only provide post-therapy information about the location of the deposed dose. However, the ultimate goal is the three-dimensional and real-time monitoring location and dose deposition of the beam.

1.2.1 Treatment plan

Hadron therapy requires three-dimensional planning. The position and density of each region of the beam has to be defined. Computed Tomography (CT) is a way to obtain these data and Magnetic Resonance Imaging (MRI) can assist in the definition of target and normal tissues boundaries. In CT, the source corresponds to the attenuation of X-rays radiation at different rates, and media. CT data are acquired

with filtered $120-140$ kVp X-rays, and represent the linear attenuation coefficients of these X-rays. The X-rays are sourced outside the object and directed through it to be detected by a ring of sensors, or a rotate fan beam scanner. The energy of X-rays are generally in the interval of $20-100$ keV. Generally, the X-ray paths are assumed to be straight lines. On their passage though the object, the X-rays are attenuated, mainly by scattering processes. Therefore, the variable to be measured is the X-ray attenuation density of the object. Since the scattering process is related to the electron density, the X-ray attenuation density is considered as related to the mass density of the object, thereby it could provide useful diagnostic information of the object structure. These measured data have to be converted into carbon or proton stopping powers in order to calculate the ion energy and range required to reach the target. The system used in treatment planning for ^{12}C therapy at GSI is presented in [Kramer et al., 2000].

The physicist or dosimetrist developing the plan typically selects 2-4 beams per target to achieve the desired dose distribution. Target volumes often have a close geometrical relationship to critical normal tissues, which suggest a few optimal beam angles to minimize normal tissue doses. Selecting a beam direction, a field-defining aperture is designed taking into account the lateral beam fall-off, target motion, and set-up uncertainties. Each beam is designed to pass the target to a specified depth. After dose calculation, individual beam parameters may still be changed until the plan is optimized.

1.2.2 Treatment monitoring

The high effectiveness of ion therapy requires an accurate precision in the monitoring of the applied dose, especially in delicate clinical situations. Hence, a high precision of ion range localization is demanded. Minor errors could result in a severe disagreement between the dose delivered to the tumor, and the surrounding healthy tissue. The treatment planning present an uncertainty of $\simeq$ 1%-3% in range calculations. In addition, the beam delivery fractionated on a long time interval could lead to unpredictable range deviations from the X-ray CT planning due to changes of e.g., patient position, or local anatomical information. Therefore, the visualization of the beam distribution within the patient is strongly required.

An intensively studied method conducts the monitoring by means of β^+ activity emitted by positrons, e.g., ^{15}O, ^{11}C, which are issued from nuclear fragmentations. The first attempts of the method application date to 1970, when the possibility of assessing an accurate dose verification was observed. Despite the results, the system was never used in clinical routine. Secondly, a PET scanner was installed at HIMAC to detect the β^+ profile when the beam delivery was in off-line mode. More recently, at GSI, a double-head PET scanner was installed and investigations were carried out for in-beam monitoring of ^{12}C ion therapy irradiation. The images were reconstructed during a fractionated treatment, i.e., using the annihilation events registered in the beam pauses, and after the end of irradiation. Since the dose depth profiles of ion beams are not identical to the β^+-activity distribution, the in-beam PET reduces to comparison between the expected β^+-activity and the one which is actually measured. The expected distribution is calculated by Monte Carlo simulations. Note that β^+ activity is highly sensitive to time variations due to e.g., dynamics of positron emitters decay, washout. Hence, knowing the treatment is divided in several sessions, the prediction of β^+ activity distribution is a complex and delicate process. In case of protons, the in-beam PET method presents applicability drawbacks due to the lack of positron emitters. Until now, no definitive conclusion was drawn about its feasibility in clinical use.

An alternative to monitor the beam location and deposed dose during irradiation treatment is to measure the complete spectrum of the emitted gamma rays. This includes nuclear gamma rays which are emitted by the relaxation of generated nuclei. This emission is isotropic, and its energy spectrum from roughly 100 keV up to 20 MeV. A detailed description of gamma rays following nuclear reactions is presented in Section 1.1.3.2. A relation between these gamma rays and the fall off region of an experimental proton beam was reported by [Min et al., 2006]. There, the nuclear gamma rays are observed by a collimated system counting only those photons which are emitted perpendicularly with respect to the beam direction. Methods of nuclear gamma-ray imaging capable to determine the delivered dose deposition for a given particle treatment fraction would be possible if an imaging system adequate to

e.g., gamma-ray emission spectra, would exist. A tracking Compton scattering based detection method is proposed as a possible solution for imaging gamma rays emitted during hadron therapy. Chapter 4.3 presents the expected performance of a simulated system, which illustrates the method, along with the reconstructed images when considering both ideal events, and events including detection uncertainties.

The ultimate goal is to infer on the dose from the measured gamma ray signal. The comparison between expected and measured activity could indicate deviations, so a prompt intervention has to be considered for the next treatment session. However, for in-beam PET, the clinical relevance of deviation can not be easily extracted from the PET images alone [Parodi, 2004]. An optimal solution to the dose quantification problem would be the development of an algorithm able to estimate the most probable dose distribution for a gamma-ray image measured at known conditions, e.g., time of irradiation. That would mean to solve the inverse problem of recovering the applied dose $D(x)$ from the measured distribution $A(x)$. The relation can be formulated by the equation $A = M \times D$, where M is the transition matrix storing the probabilities that a dose contribution $dD(x)$ reflects the production of an activity $dA(x)$. However, the in-beam PET images present several drawbacks which make the problem resolution difficult. The PET images are not quantitative. Moreover, the recorded counts are extremely reduced due to also the limited angle of the PET scanner geometry. The chosen solution is an interactive software tool [Parodi, 2004]. An alternative describes the PET image as a convolution of the dose distribution with a filter function under certain assumptions, e.g., the absorbing medium is homogeneous near the distal fall-off region. A formalism to analytically recover the filter function from the simulated PET data was developed by [Parodi and Bortfeld, 2006]. However, the fundamental step of inverting the convolution procedure has to be concluded before being able to state the feasibility of dose monitoring with the measured data.

Chapter 2

Gamma-ray detectors

2.1 General overview

Detection and measurement of gamma rays is a complex process since they have to interact directly with a particle in order to be detected. Generally, the interaction alters the properties of photons. Therefore, a desired detection is by means of photoelectric absorption process in one single interaction, being restricted to only when the underlined application permits. When considering the Compton scattering process, the photon continues its travel after a scattering event by spreading out its energy. Meanwhile, it becomes the predominant interaction process when increasing the initial energy of the incoming photons. Usually, detector materials with high atomic numbers are used to obtain predominantly photoelectric absorption events. Contrary, the Compton based detectors made by low-atomic materials facilitate the scattering process, and the directional localization is gained from the interaction positions, and energy deposits. A detailed description of Compton based detectors is presented in Section 2.2. When photon sources present energies above $\sim$ 10 MeV, a detector based on pair creation may be considered. Pair detectors used in gamma-ray astronomy consist of two sub-detectors: a converter and an absorber. The use of conversion foils limits the angular resolution and energy measurement at lower energy. Modern pair telescopes include GLAST [Gehrels and other, 1999], and AGILE [Tavani et al., 2003].

Detection of photons implies the transition of photon energy into a form of electrical energy. This process could be achieved by means of direct detection of photons, or their conversion into light photons followed by the light detection. Direct detection of photons requires that photons are photoelectrically absorbed within the detector volume. On absorption, an atom is ionized and photoelectrons are ejected. A method of collecting the photoelectrons and determination of the ejection sites has to exist. The two main types of direct detection are based on gas-filled chamber and semiconductors [Knoll, 2000]. Semiconductor detectors present several advantages over the gas-filled detectors, including higher quality of ionization detection, and higher mobility of charged particles.

When considering a large energy band of gamma-rays from several keV up to tens of MeV, other detection techniques can be underlined. Temporal and spatial modulation detectors are mostly used for gamma-ray astronomy, being rather simple detectors, and rather more complex ones, respectively. Coded masks based systems are spatial modulation detectors consisting of mainly two parts: a mask with open/opaque pixels, and a spatially resolving detector divided into pixels. Each detector pixel records the sum of signals from different incoming directions. Coded masks detectors present the advantage of a large Field-Of-View (FOV), at the expense of high background.

A focusing gamma-ray detector is based on Laue lenses, which integrated into an optical system deviates the incident photons to a focal spot by a shifting phase and a subsequent inference. Laue lenses based detectors include the main advantage of a detector volume much smaller than the collection area formed by the lenses. Hence, only a small detector is necessary, and consequently, reducing the background, which constitutes a limiting factor of detection sensitivity. The disadvantage is the very

narrow FOV, which determines limited imaging capability. Laue lenses are mainly applied to energies of gamma-rays up to a few MeV. An example for astrophysics is the CLAIRE balloon-flight [Halloin, 2003].

2.1.1 Scintillation detectors

One of the oldest approach to measure photon radiation is by means of scintillator detectors, which convert photons into light photons. An optimal scintillator should complete several conditions, including efficient and linear conversion of gamma rays, transparency of its emitted light, short decay time [Knoll, 2000]. Generally, no scintillator could present all these properties, thus a compromise solution has to be found.

The uniformity of light collected depends on the geometry of the scintillator. Dispersion and loss of light photons result in degraded energy and position resolutions, thus light sensors should cover all faces of the scintillator. Despite the heavily restriction of the measured data to the emitted photons in perpendicular directions, gamma cameras are still used due to their relatively reduced costs, and simplicity of technologies.

Scintillation based detectors are widely used for nuclear imaging (e.g., emission CT). Emission CT techniques are represented mainly by Single Photon Emission Computed Tomography (SPECT) , and Positron Emission Tomography (PET), where the emanations are represented by gamma photons emitted by e.g., a distribution of radio-pharmaceuticals in the object. Two main differences exist between transmission CT and emission CT. First, there is no control over the sources in emission CT other then choosing the type and method of pharmaceutical administration. Hence, the function to reconstruct in emission CT is the source distribution rather than a physical property of the object, as in the case of transmission CT. Secondly, the source distribution is situated in an enclosed medium (e.g., the patient body), therefore the emitted gamma ray beam is subject to attenuation before escaping. This constitutes a difficult problem to emission CT since the source distribution has to be recovered before attenuation correction. In transmission CT, the knowledge of the source and detector positions determine the straight line path of the X-ray beam. In emission CT, the source position is unknown a priori, so a way to localize the photon's path has to be found.

In SPECT, a collimator is placed in front of a gamma camera to achieve directional localization: only those photons directed perpendicular to the camera could be detected (Figure 2.1). The gamma camera is rotated around the patient during the scan collecting a set of projections. A rather severe loss

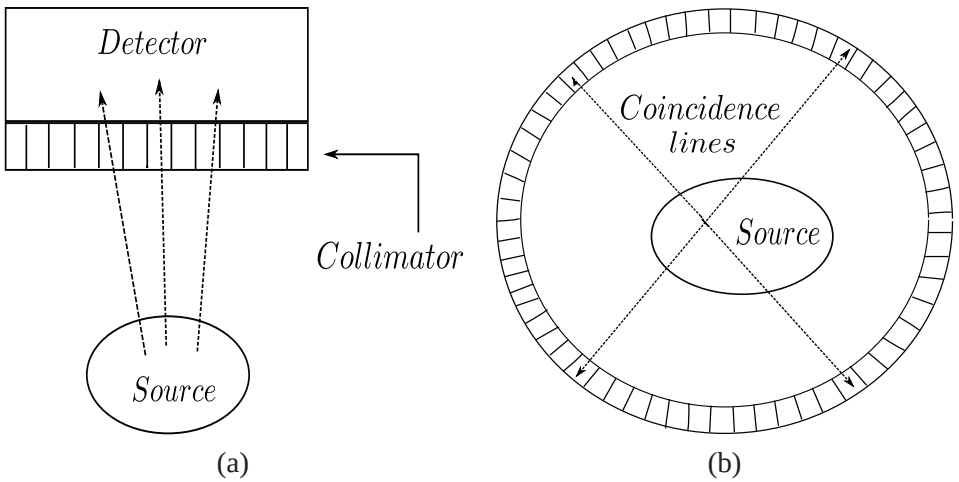

Figure 2.1: Schematic representation of the (a) SPECT, and (b) PET scanner geometry. In SPECT, a collimated detector is rotated around the source of gamma ray; only those photons which arrive perpendicularly to the front of the camera can be detected. In PET, the coincidence detection of two photons determines the source point on their emission line.

of sensitivity is accepted for knowing the path of the incoming photon. Cone-beam collimators, which have the holes arranged to focus at a point situated at finite distance past the body, could improve the sensitivity by $\simeq$ 2-3 times. Another drawback of collimators is given by the penetration of gamma rays, especially at higher energies, into the collimator material. Collimators consist of holes through which gamma rays have to pass. The material surrounding the holes is called septal fins. If the septal fins are too small, then gamma rays penetrate through them resulting in degraded reconstructed images. If the septal thickness is too large, the spatial resolution is degraded, so a compromise has to be established.

Another alternative to directional localization is to use sources which emit in a priori known configurations. An example is PET, which uses positron sources. A positron annihilates with an electron, generally very near the positron position, resulting a pair of two opposite direction gamma rays (see Section 1.1.2.4). The source direction is approximated on the straight line intersecting the two detection points. The PET detection systems include limitations. The travel distance of the positron before annihilation, and the angular deviation from the straight line of the photon pair degrade the image quality. In contrast to transmission CT, emission CT suffers from low photon counts and poor spatial resolution. In addition, photons which are influenced by attenuation or scattered in the object could be detected. Altogether lead to a generally poor quality of the reconstructed images.

A widely used SPECT detector is the Anger camera. The camera consists of three main components, including the collimator, the PhotoMultiplier Tubes (PMTs), and the lead shield (Figure 2.2).

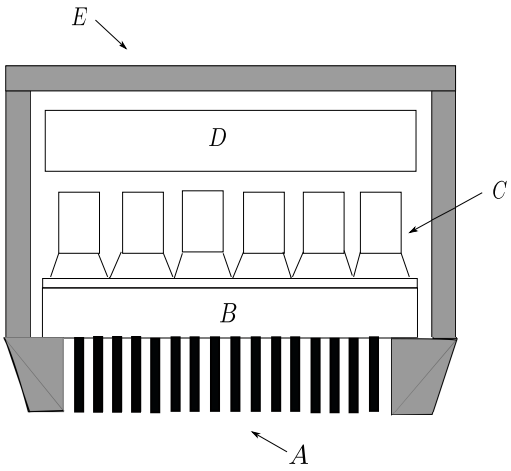

Figure 2.2: Schematic representation of Anger camera with parallel-hole collimator. The main geometry components are (A) multichannel collimator, (B) NaI Crystal, (C) hexagonal array of photomultiplier tubes, (D) position detection network, (E) lead shield.

The collimator performs the function of directional localization. Photons interact into scintillator producing light photons, which following different probabilities could reach the PMTs. Electronics of detection determine the position interactions from the PMTs data. The main interaction desirable to occur between scintillator and gamma rays is photoelectric absorption. However, photons could undergo Compton scattering and further exit the scintillator, or interact in different positions. If the Compton scattered gamma photons subsequently interact, then the light photons spread out over a large spatial distribution.

For not increasing the data collection times, and in the same time to improve the photon counts, a more efficient detection system is desirable. An alternative able to attain higher efficiency includes a first detector which replaces the collimator by a material allowing to measure photons arriving from a large spectrum of directions. Therefore, this detection technique was firstly called electronic collimation, taking further the name of Compton camera. A detailed presentation of its detection principle is included in Section 2.2, along with its main advantage over collimator detectors, namely the imaging capability.

2.1.2 Semiconductor detectors

Semiconductor detectors present rather high energy and spatial resolution for radiation imaging. Meanwhile, they are relatively sensitive to degradation caused by, e.g., neutron radiation. Semiconductor detectors may be divided in two types: classical semiconductor detectors and memory detectors. The memory detectors may be further divided into sub-groups including Charge-Coupled Devices (CCD) and drift detectors. The CDD detectors are not considered herein due to their relatively poor efficiency for gamma-ray imaging, and the need to shift out information serially.

Classical detectors consist of, e.g., a p^+n junction on one face, and a nn^+ junction on the opposite face of a n-type semiconductor wafer. The junction is reverse biased to completely descend the substrate, which creates an electrical field between two junctions. Electron-hole pairs are created by a radiation interaction into substrate, and pass towards the junctions due to electric field. The charge measured at junctions results in energy measurement of radiation interaction. Two-dimensional position resolution is obtained by dividing one face of a junction into strips, and the opposite face into strips oriented in orthogonal direction [Knoll, 2000]. Semiconductor detectors are generally made of, e.g., Silicon or Germanium. If detectors are fabricated from High Purity Germanium (HPGe), they have to be cryogenically cooled to achieve high energy resolution. The cooling is necessary in order to reduce thermally induced noise to acceptable levels. In certain applications, Silicon based detectors have to be operated under cooled conditions as well. Detectors operating at room temperature are made of materials such as CdTe, CdZnTe. Their higher atomic number determine a greater efficiency per unit volume of material, but their use is limited by the low mobility when compared to Silicon or Germanium, and the difficulty of producing large enough detectors.

Drift detectors consist of a n-type Silicon wafer with p^+ electrodes placed at even spacing on both faces of the wafer. An electric field is applied via the electrodes to use up the Silicon bulk. A potential surface is created so that electrons resulting from a gamma-ray interaction are collected at the center of the semiconductor between the faces. A potential tilt parallel to the detector face is created so that electrons from the center of detector are drifted to one end of the detector where the charge is collected by segmented anodes. This information provides position resolution in one direction. Position resolution in the orthogonal direction is performed by measuring the length of the time necessary to electrons to drift out. The time of gamma-ray interaction may be obtained by detecting holes collected at the electrodes. The count rate capability could be of about 10 to 100 times better than classical detectors.

When considering a detector based on Compton scattering, the Silicon presents several advantages, e.g., it can be used at much higher temperature than a Germanium detector, Doppler broadening is smaller at lower atomic materials. To achieve a reasonable detection efficiency, rather thick detectors are required. The limited usable thickness of Silicon drift detectors may be overcame by 'stacking' many detectors, though this increases the electronic complexity.

2.2 Compton scattering based imaging detectors

A gain in sensitivity can be achieved by replacing the collimated part of a gamma camera by a low-atomic material, e.g., Silicon, which can enable radiation detection with a larger spectrum of incoming directions. According to a particular application, the configuration of Compton camera has to be optimized in terms of detection efficiency and resolution. This process is a complex multi-parameter problem, which should determine the optimal values of e.g., thickness of both scattered and absorption detectors, positioning, distance between the two detectors, etc.

Performing directional localization by Compton scattering process implies a form of photons tracking through the complete interaction process in order to determine their initial energy. In collimated detectors, the photon direction lies on a rather straight line. The direction determination becomes more complex when the detection is based on Compton scattering. There, the photon direction lies on the

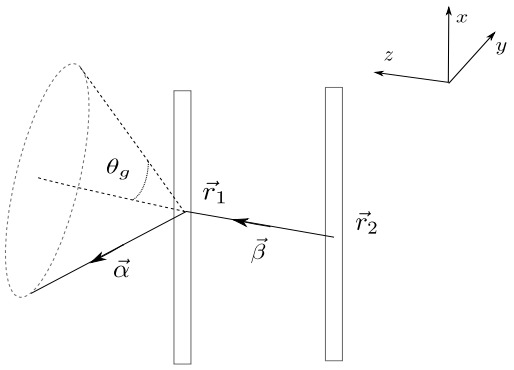

Figure 2.3: Illustration of the conic projection from a Compton scattering event defined by the main required elements: the energy deposited E_1 in the first interaction at the position $\vec{r}_1$, and the energy deposited in the back detector at the position $\vec{r}_2$. The Compton scattering angle θ_g is computed from the measured energies.

surface of a cone determined by the interaction positions and energies deposited, being widened by measurement uncertainties. Further the surface may be restricted to an arc of cone if the scattered electron direction is (partly) known. Hence, a novel image reconstruction problem reveals.

Let $\vec{\alpha}$, $\vec{\beta}$ be unit vectors. Consider a photon of energy E_0 traveling in direction $-\vec{\alpha}$ through a detector capable of tracking multiple Compton events. The photon undergoes a Compton event at a position $\vec{r}_1$ through an angle θ_g. Both position and energy deposited E_1 are measured. The photon of changed direction $-\vec{\beta}$ could further undergo a second Compton interaction at position $\vec{r}_2$ deposing E_2 energy. The travel of photon continues until complete absorption, or escape the detector. Whether a photon is likely to escape or to be completely absorbed depends on the detector geometry. In case of complete absorption, the initial energy can be computed by the summation of energy deposited in the interactions:

$$E_0 = \sum_i E_i \tag{2.1}$$

When the photon escapes the detector, a relation between energies can be derived:

$$E_0 > \sum_i E_i \tag{2.2}$$

The scattering angle θ_g can be computed by the Formula 1.7. When the initial energy is determined by Equation (2.2), the scattering angle will be less than or equal to θ_g. The photon direction after the first scattering event can be computed by the following formula:

$$\vec{\beta} = \frac{\vec{r}_1 - \vec{r}_2}{|\vec{r}_1 - \vec{r}_2|} \tag{2.3}$$

The initial direction of the photon has to verify the equation:

$$\cos\theta_g = \vec{\alpha} \cdot \vec{\beta} \tag{2.4}$$

which corresponds to the localization of the photon incoming direction $\vec{\alpha}$ on the surface of a cone described by its apex $\vec{r}_1$, symmetry axis $\vec{\beta}$, and semiangle θ_g.

2.2.1 Considerations of geometries design

The most simplistic Compton imaging system consists of two planar position and energy sensitive detectors (Figure 2.3). The first detector, called the scattering detector, is made of a low-atomic number material for optimization of the Compton scattering likelihood. The configuration details depend mainly on the imaging system purpose, namely the required energy and spatial resolution when photons of wide energy spectrum are measured. The second detector is made of a high atomic number material to optimize the likelihood of a photon to undergo a photoelectric effect. Several Compton telescopes as well

as the medical Compton scattering cameras are of this type. Measuring the data after the first two interactions, assuming that only one interaction occurred in each detector, all the required information to determine the incoming photon direction is collected. Namely, the initial source of a photon reaching the detector is localized on the surface of a cone by measuring the position of interaction of the first scattering event ($\vec{r}_1$), the energy lost during the first interaction (E_1), and the photon direction ($-\vec{\beta}$) after scattering. If the second interaction is a photoelectric event then the tracking of the photon is completed, allowing to compute the final photon direction. When the photon undergoes other Compton scattering events, a tracking of the photon is required until an absorption occurs, or until it escapes out of the detector. Photon tracking is imperatively needed by the computation of the initial energy of the source and by the event reconstruction process. The original parameters of the incident photons are recovered by application of event reconstruction algorithms when the Compton scattered data is measured by an imaging system enabling multiple Compton interactions. In e.g., astrophysics, advanced Compton imaging detectors (Compton telescopes) consist of a scattered detector formed by several e.g., Silicon layers wherein the incident photons undergo multiple interactions. Details about the general configuration of the detectors as well as the required event reconstructions algorithms can be found further in the present section, or in [Zoglauer, 2005].

Detection of photons by means of Compton scatters was firstly proposed by [Schönfelder et al., 1973], in the measurement of atmospheric gamma-rays context. [Todd et al., 1974] introduced the Compton imaging system for medical applications as an improved alternative to collimated based detectors. Since the first Compton camera prototype was developed for medical application by [Singh and Doria, 1983a], different geometry models were proposed searching to attain an efficient design of Compton camera. A single high-purity germanium, and a scintillator detector were next proposed by [Singh and Doria, 1985]. [Kamae et al., 1988] developed a Compton imager replacing the detectors of the first camera prototype with layers of Silicon strip detectors, which were surrounded by a cylindrical CsI(TI) scintillator. In astrophysics, the COMPTEL [Schönfelder et al., 1993a] telescope proved a real success in covering an unprecedented energy spectrum from 1 MeV to 30 MeV. For medical applications, [Bolozdynya et al., 1997] explored a model consisting of concentric hollow cylindrical detectors. Meanwhile, [Tumer et al., 1997] analyzed a prototype consisting of multiple detectors followed by CsI(TI) calorimeter arrays, or CdZnTe [Du et al., 1999]. The University of Michigan group in collaboration with CERN developed a camera prototype C-SPRINT (Compton-Single Photon RINg Tomograph), which consists of a Silicon cylindrical detector surrounded by an absorption detector [Leblanc et al., 1999]. The optimal parameters which could solve the trade-off between sensitivity and resolution of this prototype simulated version were studied [Chelikani et al., 2004].

Advanced Compton cameras referred as Compton telescopes can enable the tracking of electrons recoiled in Compton scatterings. The photon direction is then further restricted to a segment of a cone, whose length depends on the measurement accuracy of the recoil electron. Hence, the origin of the incoming photons could be solved with higher accuracy. The tracking Compton and pair telescope MEGA (Medium Energy Gamma-ray Astronomy) [Zoglauer, 2005] was studied at the Max-Planck-Institut für extraterrestriche Physik (Garching, Germany) where in 2003 a prototype version was calibrated. MEGA mainly consists of a tracker (or scatterer) where Compton scattering and pair creation events are factorized, and a calorimeter which surrounds the low hemisphere of the tracker. The latter has the purpose to measure the interactions position as well as the deposited energy of the secondary particles. Other examples of this group are the TIGRE [Bhattacharya et al., 2004], and detectors where gaseous time projections chambers are used to track the recoil electron [Tanimori et al., 2004].

In case of electron tracking detectors as MEGA, an intermediate step is integrated into data analysis, namely the event reconstruction. Event reconstruction reconstitutes the photons path into detector, i.e., finding the interactions which belong to an event, the start and end points of their track, classify the event as Compton scattering, or other interaction. The initial step is the identification of electron tracks as well as their travel direction. This determination is done by investigating the topology of the tracks

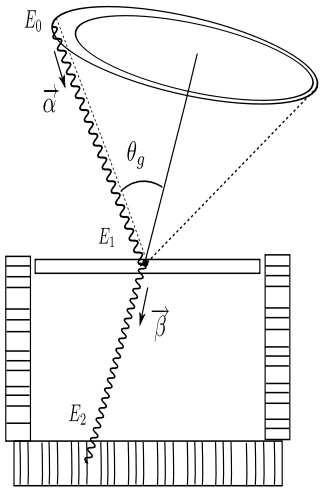

Figure 2.4: Schematic representation of the conic projection from one Compton event measured by the Compton Camera (CC) imaging detector. The simulated CC system is made of a single double-sided Silicon layer, which consists of one wafer which has a length of 10 cm, thickness of 2 cm, and 0.47 mm pitch. The second detector consists of $LaBr_3$ bars (surface area: 5×5 mm, length: 8 cm).

and the Compton kinematics, especially the energy deposits on the wafers. Afterwards, searches for the Compton interaction sequences are performed, i.e., all Compton interactions are arranged in their kinematically correct order. The parameters guiding the search are the direction of the recoiled electron, the redundant information when the event consists of three or more interactions, the geometry of the detector as well as the absorption probabilities along the path of the photon [Zoglauer, 2005].

2.2.2 Angular resolution

Consider a Compton scattering based camera consisting of a scattering detector and an absorption detector, similar to the camera design proposed by [Singh and Doria, 1983a]. Both detectors are represented by their dimensions, noted as $l_s \times l_s$, $l_a \times l_a$, and the pixel size, $d_s \times d_s$, $d_a \times d_a$. The distance between the detectors is noted by S, and the thickness of the scattering detector by t_s.

The accuracy of direction localization of an incident photon depends mainly on how precisely the cone parameters are determined. Inherent measurement errors of interaction positions and scattering angle (θ_g) bring uncertainty in the location of the source. Hence, the main factors influencing the measurement are the energy resolution of the scattering detector, the position resolution of both detectors, the thickness of the scattering detector, and the distance of the source to the scattering detector. All factors contribute to the angular uncertainty $\Delta\theta_g$ in the cone angle measurement. This dependence can be expressed by the formula [Singh and Doria, 1983a]:

$$\tan^2 \Delta\theta_g = \tan^2 \Delta\theta_1 + \tan^2 \Delta\theta_2 + \tan^2 \Delta\theta_3 + \tan^2 \Delta\theta_4 \tag{2.5}$$

where $\Delta\theta_1$ denotes the uncertainty due to the scattering detector energy resolution, $\Delta\theta_2$ and $\Delta\theta_3$ are due to the scattering element width and thickness, respectively. The factor $\Delta\theta_4$ represents the uncertainty due to the position resolution of the absorption detector.

The angular uncertainty due to the energy resolution of the scattering detector when considering photons of initial energy E_0 is given by

$$\Delta\theta_1 = |\frac{d\theta_g}{dE_s}|\Delta E_s = \frac{[1+\alpha(1-\cos\theta_g)]^2}{\alpha E \sin\theta_g}\Delta E_s \tag{2.6}$$

where ΔE_s is the uncertainty in measuring the scattering energy E_s, and α is given by Formula 1.4. Noise processes in the semiconductor detector determine the minimum energy which is possible to measure. Hence, a minimum scattering angle above which all the scattering events are not detectable exists. In the ideal case, the minimum angle should be less than 5°.

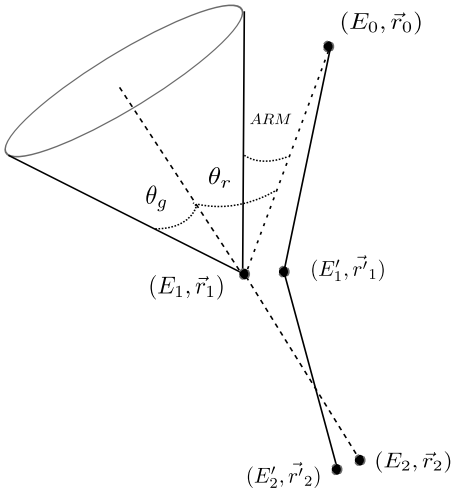

Figure 2.5: The angular resolution measure represents the difference between the Compton scatter angle θ_g calculated from the measured energies, E_1, E_2, and the angle between the known initial direction, and the measured direction of the scattered gamma ray. ARM parameter corresponds to the width of the Compton scatter cone (or arc).

The angular uncertainty depends also on the camera geometry [Singh and Doria, 1983a]

$$S\tan(\theta_g - \Delta\theta_2) = S\tan(\theta_g - \tan^{-1}(d_s/2D)) - 1/2d_s \quad (2.7)$$
$$S\tan(\theta_g + 1/2\Delta\theta_3) = (S + 1/2t_s)\tan\theta_g \quad (2.8)$$
$$S\tan(\theta_g - 1/2\Delta\theta_4) = S\tan\theta_g - 1/2d_a \quad (2.9)$$

where D is the distance of a point source to the front of the camera.

The factors which contribute to angular uncertainty may be written

$$\Delta\theta_2 = \theta_g - \tan^{-1}(\tan(\theta_g - \tan^{-1}(d_s/2D)) - 1/(2d_sS)) \quad (2.10)$$
$$\Delta\theta_3 = 2\tan^{-1}(1 + 1/2St_s)\theta_g - 2\theta_g \quad (2.11)$$
$$\Delta\theta_4 = 2\theta_g - 2\tan^{-1}(\tan\theta_g - 1/2d_a) \quad (2.12)$$

The spatial uncertainty of a point source at a distance D to the front of the camera verifies the equation [Singh and Doria, 1983a]

$$\Delta x = D\tan(\Delta\theta_g) \quad (2.13)$$

The above equations assume unknown the energy of the incoming photons, deposing all the energy in two interactions.

The Compton detector design has to consider the intended energy regime. When increasing the detector thickness, the efficiency improves. But this gain is obtained at the expense of angular uncertainty [Singh and Doria, 1983a]. Hence, a compromise between different parameters describing the detector has to be found. The optimization process of camera geometry should consider inherent created effects, such as Doppler broadening, important especially in case of low-energy (e.g., below 1 MeV) gamma-rays of scattered spectra, the polarization photons.

An usual parameter describing the angular uncertainty is the Angular Resolution Measure (ARM) . This parameter is defined as the angle between the reconstructed back-projection cone, and the real (or simulated) source direction, or as the shortest diatance between the known initial photon direction, and the photon scatter cone defined by the measured direction of the scattered photon:

$$\Delta ARM = \theta_r - \theta_g \quad (2.14)$$

where θ_r is calculated from the measured interaction positions and the true source location ($\vec{r}_0$):

$$\theta_r = \arccos(\vec{\alpha} \cdot \vec{\beta}) = \arccos\left(\frac{(\vec{r}_1 - \vec{r}_0)(\vec{r}_2 - \vec{r}_1)}{|\vec{r}_1 - \vec{r}_0||\vec{r}_2 - \vec{r}_1|}\right) \tag{2.15}$$

The angle θ_g is computed from the measured energies by the Compton formula 1.7.

Note that different scattering angles result in different ARM distributions when considering the energy uncertainty and Doppler broadening effect. A way to reduce angular uncertainty is the selection of events having certain scattering angles at the expense of efficiency.

In case of a more complex imaging system, e.g., electron tracking Compton telescope, the angular resolution can be described by the ARM jointly with the Scatter Plane Deviation (SPD) . When the recoil electron is incompletely absorbed, the ARM is positive, while its value becomes negative in case of an incompletely absorbed photon. The SPD parameter illustrates the angle between the real scatter plane described by $\vec{\alpha}$ and $\vec{\beta}$, and the measured plane described by $\vec{\beta}$ and $\vec{e}$, assuming that $\vec{\beta}$ was correctly measured:

$$\Delta SPD = \arccos((\vec{\alpha} \times \vec{\beta}) \cdot (\vec{\beta} \times \vec{e})) \tag{2.16}$$

where $\vec{e}$ is the direction of the recoil electron. Note that SPD is relevant only when $\vec{e}$ was measured, being influenced by the measurement accuracy. ARM describes the Compton cone width for each individual reconstructed Compton event, while SPD provides a measure for the length of the Compton scatter arc.

The ARM is influenced by mostly all components of the measurement process, the accuracy of the energy of the electron and the scattered gamma ray as well as the accuracy of directions calculations. The energy resolution determines the Compton scattering angle θ_g in the Formula (2.14), while the quantity θ_r is influenced by the position resolution. The propagation of measurement errors in computation of the Compton scattering angle θ_g (Formula (1.7)) results in the following expression

$$d\theta_g = \frac{E_0}{\sin\theta_g}\sqrt{\left(\frac{1}{E_g^2} - \frac{1}{(E_e + E_g)^2}\right)dE_g^2 + \frac{1}{(E_e + E_g)^4}dE_e^2} \tag{2.17}$$

The angular uncertainty determines the response of an imaging system. Both energy and position uncertainty on the detector contribute to the resulted angular uncertainty. The interaction positions define the axis of the back-projected cone, so uncertainty on positions reflect uncertainty on the cone axis direction. However, the Doppler broadening constitutes an inherent limit of measurements precision [Zoglauer and Kanbach, 2003].

2.2.3 Efficiency parameters

The basic definition of photon detection efficiency in case of a complex arbitrary detector is

$$E_{\text{tot}} = \frac{\text{total number of detected photons}}{\text{total number of photons emitted by the source}} \tag{2.18}$$

It may be expressed also by the product of four factors

$$E_{\text{tot}} = E_{\text{geom}} E_{\text{abs}} E_{\text{sample}} E_{\text{int}} \tag{2.19}$$

The geometric efficiency E_{geom} denotes the fraction of photons which arrive on a detector for a point source. Its expression is

$$E_{\text{geom}} = \frac{A}{4\pi r^2} \tag{2.20}$$

where A is the cross-sectional area of the detector, and r is the distance of the source to the detector. The absorption efficiency E_{abs} represents the absorption coefficient of different materials which constitute

the detector, absorbing a part of incoming photons before interacting within the detector volume. Its expression is

$$E_{\text{abs}} = e^{-\sum \mu_i \rho_i x_i} \tag{2.21}$$

where μ_i, ρ_i, and x_i are the mass absorption coefficient, density and thickness of the ith material, respectively.

The sample efficiency E_{sample} is the fraction of emitted photons which actually emerge from a sample material. Its expression is

$$E_{\text{sample}} = \frac{1 - e^{-(\mu\rho x)_s}}{(\mu\rho x)_s} \tag{2.22}$$

The intrinsic efficiency E_{int} is the probability that a photon interacting into detector will result in a valuable signal. A standard form to express E_{int} is

$$E_{\text{int}} = 1 - e^{-\mu\rho x} \tag{2.23}$$

Generally, the detection efficiency strongly depends on the photon source energy, i.e., E_{int} dominates at higher energy, while E_{abs} at lower energy.

The efficiency of Compton camera can be expressed by the product

$$S = \frac{\Omega}{4\pi} P\epsilon \tag{2.24}$$

where Ω is the solid angle subtended by the scattering detector relative to the source location while ϵ is the efficiency of the absorption detector. The parameter P represents the probability that a photon is scattered without further interaction in the absorption detector. [Singh and Doria, 1983a] derived its value. The solid angle follows the formula [Knoll, 2000]

$$\Omega = \int_A \frac{\cos\vartheta}{c^2} dA \tag{2.25}$$

where A is the surface of the scattering detector, ϑ is the angle between the line segment from the source to the element of area dA, and the normal to dA. The length of the line segment is c. For a point source located at a distance D to the scattering detector, the solid angle Ω is given by the formula:

$$\Omega = 4\tan^{-1}\left(\frac{l_s^2}{4D\sqrt{1/2l_s^2 + D^2}}\right) \tag{2.26}$$

When considering a Compton scattering based camera, another issue is important, namely the full flux of photons under which it is exposed, unlike, e.g., Anger camera, which is shielded by the collimator. The absorbing detector of the Compton camera receives both photons passing interacting with the scattering detector, and all other photons passing directly without interaction. The absorbing detector has to be able to handle high count rates, even though a part of events are rejected as not valuable events. A proposal is to use a scintillation detector as the absorbing detector. Even if high performance technology exists to implement the absorbing detector, it is still likely to be the limiting factor to the total achievable count rate of the Compton scattering camera.

To characterize the measured count rate r_m of usable coincident detections, consider the count rate r_s incident on the scattering detector. The count rate r_a incident on the absorbing detector is

$$r_a = r_s\left[e^{-\mu_p t_s} + \left(\frac{\Omega_s}{\Omega_a} - 1\right)\frac{\Omega_a}{\Omega_s}\right] \tag{2.27}$$

where μ_p is the photoelectric absorption coefficient of the scattering detector, while Ω_s and Ω_a are the solid angles presented to the source by the scattering and absorbing detectors, respectively. The first term

of Equation (2.27) includes photons absorbed in the scattering detector, and the second term includes the solid angle shown by the absorbing detector over the scattering detector. The measured count rate of valuable photon interactions r_m is then given by

$$r_m = \frac{P r_a e^{-r_a \tau}}{\Omega_a/\Omega_s - 1 + e^{-\mu_p t_s}} \tag{2.28}$$

where P is the probability of a useful scatter, while τ is the dead time of the absorbing detector.

Several possibilities to improve the count statistics were proposed depending on the targeted energy regime. When imaging sources of 140 keV, [Singh and Doria, 1983a] proposed a semiconductor material as the absorption detector. Generally, at this energy, a Germanium absorption detector could generate higher count rates, improved energy and position resolution than Anger camera. For higher source energy, the general choice is a scintillator based absorption detector made by either, e.g., NaI, or more effectively by, e.g., $LaBr_3$ bars. An alternative to achieve higher count rates is to use a 'stacked' of scattering layers. This design can improve the camera sensitivity at the expense of increased electronic and control complexity.

2.2.4 Compton imaging

Compton imaging is defined as the image reconstruction process of data generated by a Compton scattering based detector. Compton data are back-projected into the image space without preserving the azimuthal angle when assuming no electron tracks. The complexity of Compton reconstruction process arises from the possible directions of the source laying on the ambiguity of a surface cone. Moreover, the measurement errors of both position and energy result in angular uncertainty over the measured angle of the cone.

Compton imaging may be considered as imaging technique with Poisson measurement statistics beside PET, SPECT, gamma astronomy, and microscopy methods. The factors which distinguish the Compton image reconstruction problem from the conventional tomography are the extremely large amount of data generated by the system, the highly complicated geometries and the low total counts in sample bins, which make Poisson fluctuations a significant factor. These are the reasons for which all practical reconstruction algorithms for the Compton scattering imaging systems are iterative. Iterative methods of Compton image reconstrution are presented in Section 3.2, while Chapter 5 includes algorithms for image reconstruction in particular conditions, i.e., list-mode data acquisition.

In the early 1980's, [Singh and Doria, 1983b] explored the idea of the two stage reconstruction. In contrast, [Hebert et al., 1990] formulated the reconstruction problem as the maximum-likelihood estimation of the three-dimensional distribution 'directly' from the projection data. Following the vision of image reconstruction process divided in two stages, the first stage includes the modeling of detection process, which generates the response matrices. The response describes the probabilities that a photon emission produced a recorded valid Compton event. An accurate determination of probabilities implies high-dimensional calculations, which require detailed knowledge of the detector geometry as well as the uncertainties arising from e.g., finite spatial and energy resolution, Doppler broadening. Hence, the detector response modeling plays a determinant role on the image reconstruction performance. The detector response is further integrated into the image reconstruction method, i.e., the back-projection phase, which is part of the first stage. The second stage of the process includes the application of an iterative algorithm.

2.2.4.1 Theoretical analysis of the Compton detection process

The sequence of physical interactions which corresponds to a detected event begins with the emission of a photon with an initial energy E_0 from the source point $\vec{r}_0$ in direction $-\alpha$. In the following a Compton scattering interaction is assumed to takes place in the first detector at the position $\vec{r}_1 = (x_1, y_1, z_1)$

through an angle θ_g. An energy loss E_1 is followed by a final absorbtion at $\vec{r}_2 = (x_2, y_2, z_2)$. The response matrix is then represented by the coefficients t_{ij}, which represent the probability that a photon emitted from the source location j will be measured as event i described by the measurement $y_i = \{\vec{r}_1, \vec{r}_2, E_1\}$. The following formula

$$t_{ij} = \int_{\vec{r}_0 \in V_j} p(\vec{r}_0) dr_0 \int p(y_i|y_i') p(y_i'|\vec{r}_0) \tag{2.29}$$

expresses the integral over the pixel volume V_j of the density function $p(y_i'|r_0)$ describing the probabilities of an emission from j producing an event y_i', multiplied with a function $p(y_i|y_i')$ describing the measurement process. The probability of an emission from the source to produce a detected event y_i' can be approximated by the probabilities of each sequence interaction in which the physical detection process is divided. Assuming separable measurement probabilities, its expression follows

$$p(y_i|y_i') = p(r_1|r_1')p(r_2|r_2')p(E_2|E_2')p(E_e|E_e')p(\vec{e}|\vec{e'}) \tag{2.30}$$

The probability density function $p(y_i'|\vec{r}_0)$ describes the probability that an emission from $\vec{r}_0$ in direction α, leading to the true event y_i'.

The sensitivity factor is the integral over all possible events $y' \in S$, which is the set including all the possible measurements:

$$s_j = \int_S d\vec{r}_0 p(\vec{r}_0) \int dy' p(y'|\vec{r}_0) \tag{2.31}$$

Determination of transition probabilities t_{ij} and sensitivity factor s_j constitutes the most challenging aspect of the image reconstruction process. As shown in the following, the quality of the reconstructed images highly depends on the accuracy of their calculation.

Assuming a mono-energetic source, complete absorption in the second detector, and no Doppler Broadening, [Wilderman et al., 1998a] includes a detailed description of detection probabilities as well as their impact on the response matrix calculation. In the following, the argumentation goes along the lines of [Zoglauer, 2000].

The detection process of a Compton based imaging system may be described by the sequence of processes which are involved in the detection of an event i.

1. The photon is emitted at $\vec{r}_0$

$$p(r_0)dr_0 \approx \text{const} \cdot dr_0 \tag{2.32}$$

2. The photon leaves the object reaching the detector unscattered

$$p_{\text{esc}}^{\text{obj}} = \int_r e^{-\mu_{\text{tot}}^{\text{obj}}(E_0, l_0) l_0} dl_0 \tag{2.33}$$

   The parameter l_0 denotes the length of photon path r emitted at r_0 in direction α, and μ is the total absorption coefficient knowing l_0 and the energy E_0. The absorption probabilities take into account different materials which constitute the travel medium.

3. The photon passes through the detector to the first interaction point where it is Compton scattered at the depth of l.

$$p_{\text{Compton}}^{D_1} = \mu_{\text{Compton}}^{D_1}(E_1, r_1) \int_l e^{-\mu_{\text{tot}}^{D_1}(E_1, l_1) l_1} dl_1 \tag{2.34}$$

The parameter l_1 denotes the distance in the first detector to the interaction point r_1, while the parameter $\mu^{D_1}_{\text{Compton}}(E_1, r_1)$ is the Compton absorption coefficient depending on the energy E_1, and the interaction point r_1.

4. The photon is Compton scattered at r_1 with an angle θ_g. The probability of the photon to be Compton scattered at a certain angle follows the condition:

$$p^{\text{KN}}(\theta_g) = \frac{\frac{d\sigma_c}{d\theta_g}}{\sigma_c} \tag{2.35}$$

where $\frac{d\sigma_c}{d\theta_g}$ is the Klein-Nishina cross-section (Equation (1.14)), and σ_c is the total scattering cross-section.

5. The scattered photon leaves the first detector:

$$p^{D_1}_{\text{esc}} = \int_r e^{-\mu^{D_1}_{\text{tot}}(E_2, l_2) l_2} dl_2 \tag{2.36}$$

where l_2 is the distance in the first detector from interaction point r_1 in direction $\vec{\beta}$.

6. The photon reaches the second interaction point where it is re-Compton scattered or absorbed:

$$p^{D_2}_{\text{Compton}} = \mu^{D_2}_{\text{Compton}}(E_2, r_2) \int_r e^{-\mu^{D_2}_{\text{tot}}(E_2, l_3) l_3} \tag{2.37}$$

or

$$p^{D_2}_{\text{abs}} = \mu^{D_2}_{\text{abs}}(E_2, r_2) \int_r e^{-\mu^{D_2}_{\text{tot}}(E_2, l_3) l_3} \tag{2.38}$$

where l_3 is the distance in the second detector to the point r_2.

7. All the other (known) interactions in the detector may be similarly described.

The probability density function $p(y'_i|r_0)$ is made up of all these probabilities multiplicatively.

2.2.4.2 Transmission probabilities in Cartesian coordinates

The following algorithm determines the source pixels situated on a focal plane, which are intersected by the back-projection cones for each of the detected gamma ray given the positions and energy losses in the interactions. The method of generating a typical cone equation has to follow the next steps. First, the cone axis is computed known the two interaction positions, i.e., $\vec{\beta} = (r_1 - r_2) = (x_1 - x_2, y_1 - y_2, z_1 - z_2)$. The second step is to compute the Compton angle via the Compton formula (1.6). The image space is viewed as being divided by a series of planes. Each plane is divided by a series of grid lines, which form the pixels in that plane. When an event is detected, a back-projected cone is traced through a given plane. The quadratic which describes the intersection of the cone with a plane situated at $z = z_s$ follows the equation:

$$(n(\vec{r} - \vec{r}_1))^2 = \cos^2\theta_g \cdot |\vec{r} - \vec{r}_1|^2 \tag{2.39}$$

$$(n_x(x - x_1) + n_y(y - y_1) + n_z(z_s - z_1))^2 = cos^2\theta_g \left((x - x_1)^2 + (y - y_1)^2 + (z_s - z_1)\right) \tag{2.40}$$

where $n = (n_x, n_y, n_z)$ represents the components of the unit vector along the cone axis. The following algorithm determines the intersection points between the boundaries of the plane restrained to a given view-port, and the conic [Wilderman et al., 1998b].

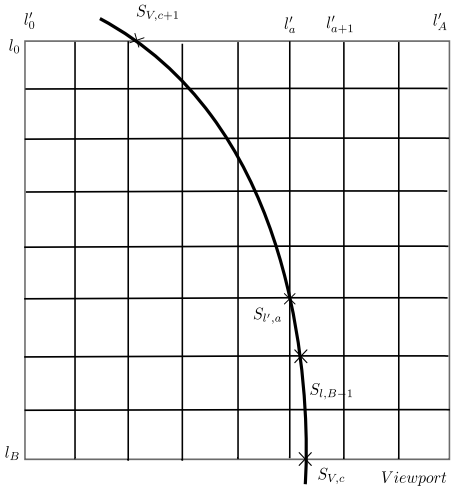

Figure 2.6: Description of sizes:

l_b	Gridlines in the y-direction
l'_a	Gridlines in the x-direction
$S_{V,c}$	Intersections with the view-port
$S_{l,b}$	Intersections with the Gridlines l_b
$S_{l',a}$	Intersections with the Gridlines l'_a

1. First, the intersections $S_{V,c}$ of the cone with the considered plane are calculated. If no intersection exists, the event is either entirely inside or outside the plane, which intersects the view-port. Further intersections are searched in restrained view-ports.
2. The view-port intersections $S_{l',a}$ and $S_{l',a+1}$ of two adjacent lines, l'_a and l'_{a+1}, are searched.
3. The intersection $S_{l,b}$ with the grid line l_b until the intersection $S_{l',a}$ is computed.
4. The distance between the two intersections is calculated.
5. If the intersection in (2) has been found to l'_a, then the search continues to l'_{a-1}, otherwise to l'_{a+2}.
6. The steps from (3) to (5) are repeated if the next intersection of the view-port has been achieved.
7. The steps from (2) to (6) are repeated for the remaining intersections of the view-port.
8. In case of tracked events, the angular distance of the cone to the origin of photons is computed.
9. Finally, an additional weighting of each event is included, according to the probability of track detection.

When considering the effect of Doppler broadening and finite energy resolution, as in practical applications, the intersection line becomes broaden. Therefore a weighting function is included in the description of the relative intensities of the underlined pixels. This function depends on the normal distance d from the pixel to the conic function, being estimated by the following

$$f(d) = 0.9e^{-\frac{d^2}{2\sigma^2}} + 0.1e^{-\frac{d^2}{2(3\sigma)^2}} \tag{2.41}$$

where σ is the standard deviation of the back-projected cone spread function. The cone spread distribution is not Gaussian due to the tails induced by Doppler broadening, thus they are modeled by adding 0.9 times a Gaussian function with the computed standard deviation, and 0.1 times a Gaussian function with three times the standard deviation [Wilderman et al., 1999].

Consider the Compton camera described in Figure 2.4. An uniform 1-sigma energy resolution of 1 keV is assumed in the scattering detector, along with a 10 keV threshold. An energy resolution of 4.3% FWHM at 662 keV, and a threshold of 28 keV are assumed in the absorption detector. Consider a square source emitting from 2 cm above the scattering detector.

Figure 2.7 illustrates back-projected images of Compton events with different scattering angles, intersecting the view-port, and including detection uncertainties, and Doppler broadening. Figure 2.8 shows back-projected images of several Compton events.

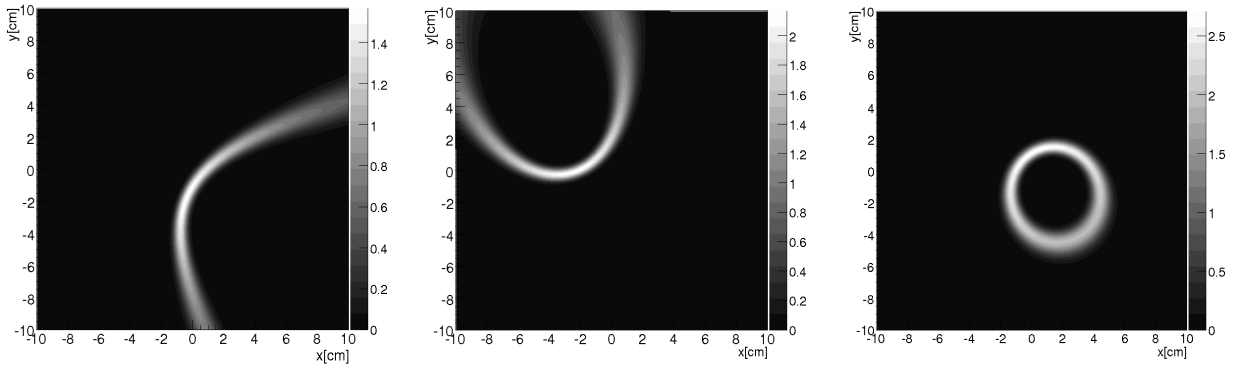

Figure 2.7: Back-projected images of different Compton events.

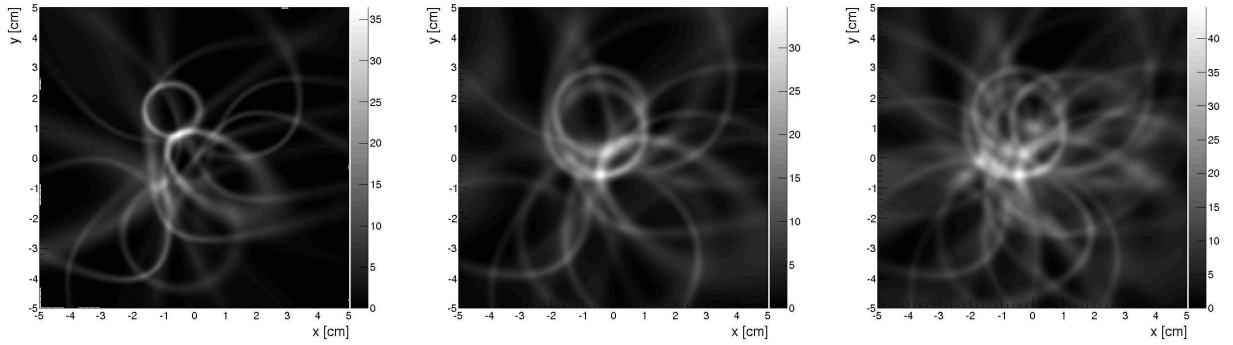

(a) (b) (c)

Figure 2.8: Images of (a) 19 Compton events, (b) 29 Compton events, (b) 51 Compton events with measurement uncertainties from energy, geometry of detector, and Doppler broadening.

2.3 Conclusions

Collimator based detectors widely used during the last decades present rather simple technologies, and a simplified method of incident photons origin localization. These advantages come at the expense of a severe restriction of directions possible to detect, i.e., only photons emitted at a perpendicular direction (and in accord to the hole thickness) to the detector represent valuable signal.

Replacing the collimator by a detector able to detect photons at a larger range of incoming directions can improve the detection sensitivity and efficiency. Compton scattering process is used as a means of detection in the first detector. Various geometry designs were proposed depending on the targeted energy regime, in both medical imaging and astrophysics. Drawbacks are represented by the complexity of technologies and methods, which have to sort and process multiple coincidence events as well as directional localization. These requirements have lately benefited from high-energy physics and gamma-ray astronomy. The cross-fertilization of these areas continue to assist the development of Compton based imaging devices for novel applications (see Chapter 4).

The angular uncertainty of a Compton based detector includes uncertainties due to energy and position resolution as well as geometrical angular resolution. The latter one depends on e.g., thickness and width of the scatterer detector pixels, intrinsic resolution of the absorption detector, distance between detectors and the considered range of scattering angle. Hence, the back-projected cone affected by inherent measurement uncertainty do not intersect the true source position. Thus the origin of photons can not be uniquely determined. The resulted ambiguity has to be solved by image reconstruction techniques.

Chapter 3

Compton image reconstruction

3.1 Medical image reconstrution methods

Modalities of gamma-ray imaging can be integrated into a class of problems named inverse problems. A general inverse problem is the determination of photons source from the detection measurements induced by physical processes. Two large classes of methods for solving an inversion problem exist. Both are based on a mathematical model, which describes the detection process. In the first class, the detection model, i.e., the direct problem, is solved analytically to obtain an inverse solution operator. Afterwards, the solution is discretized, and often solved by a computer based algorithm. Two significant difficulties of the analytic approach can be underlined: Many imaging systems can not be reliably modeled, and even if they can be, the solution may be too difficult to drive analytically.

In the second class, the detection model is firstly discretized, and the inversion problem is solved using mostly computer based iterative algorithms. An advantage of iterative algorithms is that a greater number of systems can be modeled, but an iterative process can be very computationally intensive, and no guarantee exists that the initial supposed solution will converge to the real solution.

Several factors render the image reconstruction imprecise, and possibly unreliable:

- Failure of the mathematical model to accurately portray reality.
- Measurement uncertainty and noise.
- Incomplete measurement of projection data set.
- Discretisation of the detection model.
- Mathematical difficulties to compute an accurate estimation of the solution.

Generally, even if the mathematical model is exact, the image reconstruction can fail because of the other factors. Real detection systems can introduce errors, and read-out noise in the measurement data, so the reconstruction algorithms have to operate imprecise data. Often, computer based operations also tend to amplify the noise inherently present in the data, or even fail. Hence, any practical reconstruction algorithm has to be robust against errors in the measured data.

Section 3.1.1 introduces direct image reconstruction methods applied mostly in X-ray CT imaging, while Section 3.1.2 presents a brief overview of iterative methods of image reconstruction, underlying only the main principles which constitute the base of a considerable large number of reconstruction methods.

Iterative algorithms can be classified in algebraic methods and statistical based methods. The first class includes algebraic reconstruction technique, the simultaneous iterative reconstruction technique, and the iterative least-squares technique. The second group contains algorithms which include or not

a priori information about the source. Both analytical and iterative methods of Compton scattered data reconstruction are reviewed in Section 3.2, underlying their specificity. Namely, analytical solutions in terms of integral transforms are described, including the first attempt towards direct reconstruction of Compton data proposed by [Cree and Bones, 1994]. This approach uses only the projections for which the incoming photons are scattered over a perpendicular direction between the detectors. A model which takes into account the incoming direction of photons without including any restriction about the scattering direction was developed [Maxim et al., 2009]. The inversion formula along with selected numerical experiments are presented in Section 3.2.1.

3.1.1 Direct methods

Consider the measured data g a sampled function which is related to the object under study by an integral equation. An analytic formula to inverse the equation corresponds to a direct solution of the image reconstruction problem. Once this inversion formula is found, a numerical solution has to be established. The applicability of this approach depends on the considered case, and on the operator which correlates the unknown function to the observed data.

The mathematical model of X-ray CT considers the X-beam mono-energetic and infinitesimally narrow. Considering the X-ray attenuation $\mu(x)$ along a straight line L, the measured intensity of the beam Φ follows the equation:

$$\Phi = \Phi_0 e^{-\int_L \mu(x(l))dl} \tag{3.1}$$

where I_0 is the initial X-ray intensity. Note that μ, Φ_0, and Φ depend on the X-ray beam energy. The projection over the path L is

$$p_L = -\ln(\Phi/\Phi_0) = \int_L \mu(x(l))dl \tag{3.2}$$

Generally, several projections are collected to reconstruct the object. However, Equation (3.2) can be solved when all values of L are known. Let s and ϕ be the parameters of line L, where s is the perpendicular distance of the line from the origin, while ϕ is the angle between the line and the x-axis. The projection can be approximated by the formula

$$p(s,\phi) = \int_{L(s,\phi)} \mu(x,y)dl \tag{3.3}$$

The graphical representation is illustrated in Figure 3.1.

Note that a projection along a line described by (s,ϕ) corresponds to a point in the Radon space of attenuation function μ:

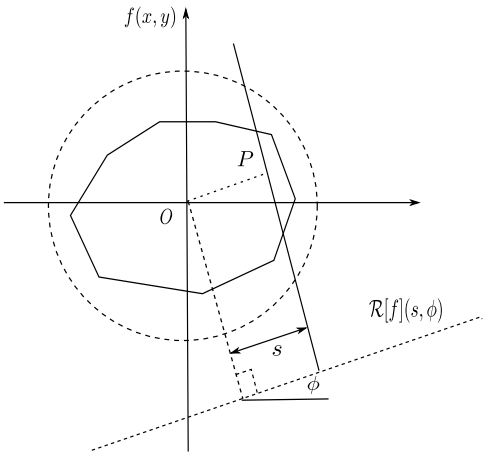

Figure 3.1: Illustration of a CT projection. The projection $\mathcal{R}[f](s,\phi)$ is the integral over the image along the line defined by s and ϕ. In 2D, the Radon transform of f follows the equation $\mathcal{R}[f(x,y)](s,\phi) = \int_{\mathbb{R}^2} f(x,y)\delta(s - x\cos\phi - y\sin\phi)dxdy$.

$$p(s,\phi) = \mathcal{R}[\mu(x,y)](s,\phi) \tag{3.4}$$

If the projections for all $s \in (-\infty,\infty)$ and $\phi \in [0,\pi)$ are measured, then the Radon space is completely filled. The application of the inverse Radon transform allows to recover μ. In practice, only a finite number of projections are collected, thus a finite number of discrete points are known in the Radon space. Several algorithms were proposed to solve the inversion problem when an incomplete set of projections exist.

In practice, X-rays beams are neither mono-energetic, nor infinitesimally narrow. Therefore, the reconstruction algorithms based on these assumptions generate images with artifacts. The width of the X-ray beam is large enough that regions to reconstruct could include variations of the X-ray attenuation coefficient. This variation can lead to wrong values of the attenuation parameter. The effect is referred as the partial volume effect.

The attenuation of the X-rays is mainly due to the Rayleigh scattering process. Thus most of the photons which escape the object, and are further detected, will degrade the image quality. Including corrections could improve the images.

Considering X-ray CT data reconstruction, if the expression relating the projections to the object is the integral equation of the Radon transform:

$$p(r,\phi) = \int\int f(x,y)\delta(r - x\cos\phi - y\sin\phi)dxdy \tag{3.5}$$

then the analytical expression of its inverse is given by:

$$f(x,y) = \frac{1}{2\pi^2}\int_0^\pi \int_0^\infty \frac{\frac{\partial p(r,\phi)}{\partial r}}{r - x\cos\phi - y\sin\phi} dr d\phi \tag{3.6}$$

which is decomposed into three operators:

Derivation D:

$$\overline{p}(r,\phi) = \frac{\partial p(r,\phi)}{\partial r} \tag{3.7}$$

Hilbert transform H:

$$g(r',\phi) = \frac{1}{\pi}\int_0^\infty \frac{\overline{p}(r,\phi)}{(r-r')} dr \tag{3.8}$$

Back-projection B:

$$f(x,y) = \frac{1}{2\pi}\int_0^\pi g(x\cos\phi + y\sin\phi,\phi)d\phi \tag{3.9}$$

The second step is to approximate numerically the integral expression. If the $p(r,\phi)$ were known for all r and ϕ, then the expression would generate a reliable solution. But $p(r,\phi)$ are known for a finite set of discrete values of r and ϕ with limited precision. Therefore two difficulties appear when numerically solving the inverse problem: the derivation $\frac{\partial p(r,\phi)}{\partial r}$, and the integration over r. Generally, the derivation is replaced by a filter (high-pass), while the Hilbert transform is applied in the Fourier domain. The integration over ϕ corresponds to the back-projection B.

The main drawback of considering the Equation (3.6) as the final inversion formula is that projections are known only for a set of discrete values of r and ϕ. The latter fact results in two difficulties, namely the computation of derivative, and the integral over r. Solutions were derived approximating the derivation by a high-pass filter, and the integration is applied in the Fourier domain.

- Back-projection of filtered projections in the frequency domain:

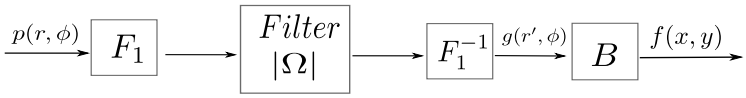

- Filtering by convolution and back-projection:

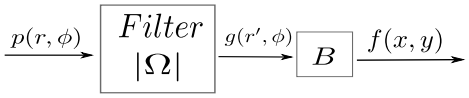

- Back-projection and 2D filtering in the frequency domain:

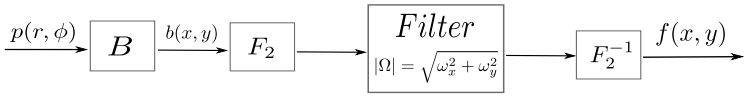

- Back-projection and filtering by 2D convolution:

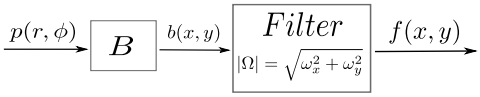

Four different methods of analytical inversion of the Radon transform are schematized above. The first and the third are versions of filtered back-projection, where the projection data are first backprojected, filtered in the Fourier space, and then inverted by the corresponded Fourier transform. It represents a reather efficient method of CT image reconstruction. Filtered backprojection has the advantage of applying the filter to each measured projection, resulting in a calculation efficiency gain. Other X-ray CT reconstruction methods include algorithms using linograms [Edholm and Herman, 1987], Chebyshev polynomials [Bortfeld and Oelfke, 1999], and nonlinear backprojection methods [Andia et al., 2002].

3.1.2 Iterative methods

"Very early it become obvious that image reconstruction was more complex than the mere problem of analytically inverting the Radon transform, and then discretizing the resulting inversion formula."
[Defrise and Gullberg, 2006]

Iterative methods can offer improvements over analytical methods since the noise structure present in measurements can be more realistically integrated in the detection system model. Application of an iterative reconstruction approach consists on several choices, which generate a significant impact on the quality of the obtained results. First, the representation basis of the source, the system physical model as well as the statistical model of measurements has to be established. Afterwards, a critical step is the choice of the cost function, or the estimation criterion on the considered data conditions. A classical approach is the Maximum-Likelihood (ML) estimation, which has various limitations, e.g., fluctuations of the solutions, noise propagation during the iterative process, etc. Alternatives can be derived on the Bayesian framework obtaining the formulations of e.g., Maximum A Posterior (MAP), Maximum Entropy (ME). Both of them present the possibility to include a prior knowledge about e.g., source distribution, expected level of noise. Corruption of solutions by noise can simultaneously be overcame including a regularization step, which incorporates constraints of the object, e.g., the smoothness degree of the solution. A regularization method is to change the cost function by adding a roughness penalty, which can be either separable or non-separable, quadratic or non-quadratic, and convex or non-convex.

Optimization of the estimation criterion implies the choice between Expectation-Maximization (EM) based iterative algorithms, e.g., Ordered-Subsets EM (OSEM) [Hudson and Larkin, 1994], Generalized EM (GEM), Space-Alternating Generalized EM (SAGE) [Fessler and Hero, 1995], and direct optimization algorithms, e.g., coordinate descent, conjugate gradient. Versions of estimation methods as well as

optimization algorithms were applied to PET, SPECT data. Reviews of iterative methods are presented in [Vandenberghe et al., 2001], [Qi and Leahy, 2006], [Defrise and Gullberg, 2006].

Consider the discrete expression of the source function is given by

$$f = \sum_j f_j b_j \tag{3.10}$$

where f_j is the average value of function f at pixel j. The f_j is the coefficient of f on the basis b_j.

Let M be the measurement model, and suppose M is linear.

$$y = Mf = M(\sum_j f_j b_j) = \sum_j M(b_j) f_j \tag{3.11}$$

and

$$y_i = \sum_j M_i(b_j) f_j \tag{3.12}$$

Consider T the response matrix of the imaging system. The discrete expression of T is related to the source function by

$$y_i \simeq \sum_j t_{ij} f_j \tag{3.13}$$

where y_i is the measured data at bin i. The response matrix represents the transition probabilities t_{ij} that an emission from f_j was detected in y_i, i.e., $t_{ij} = M_i(b_j)$ depend on the source model and measurements.

Consider e the difference between the two sides of Equation (3.13), which can be then written as

$$y = Tf + e \tag{3.14}$$

where e denotes the measurement errors.

The discrete reconstruction problem can be formulated as the estimation of the image vector f given the measured data $y = \{y_i,\, i = \overline{1, N}\}$. Iterative methods start from an initial solution f^0, which is forward projected resulting $y \sim Tf^0$. The latter is compared to the measured projections, and updated based on the knowledge about their ratio. The step is repeated until an acceptable solution is obtained. Iterative algorithms differ when considering the method which compares the current estimate to the measured data, and the application method of the correction.

3.1.2.1 Algebraic reconstruction techniques

Algebraic Reconstruction Techniques (ART) are one of the first technique used for image reconstruction from projections, being proposed as an alternative to direct Fourier reconstruction. It is essentially identical to a technique described by Kaczmarz (1937) to solve a system of simultaneous equations. The original ART algorithm [Gordon et al., 1970] looks for solutions to $y = Tf$, assuming $e = 0$, and the existence of a unique solution. The algorithm requires modifications to allow reasonable solutions in realistic conditions.

The additive ART algorithm considers the vector m_i as the transpose of the ith row of matrix T. Consider an arbitrary initial solution f^0. The additive iterative formula can be written as

$$f^{k+1} = f^k + \frac{y_i - m_i \cdot f^k}{m_i \cdot m_i} m_i \tag{3.15}$$

where $i = (k mod J) + 1$, and J is the number of elements in f. Note that only one element of y and the corresponding row of T are used to update f. To obtain a complete update on f using all rows of T requires several iterations. Variations of the basic algorithm are presented in [Herman and Lent, 1976].

3.1.2.2 Maximum-likelihood algorithms

The ML reconstruction technique was introduced in emission CT by [Lange and Carson, 1984] in conjunction with the EM algorithm, taking into account the statistical nature of photons emission. The ML criterion states that the best estimate of the source f has to give the greatest probability of obtaining the measurement y. This condition can be expressed as the following

$$\hat{f} = \arg\max_{f \geq 0} p(y|f) \tag{3.16}$$

The method can be summarized as follows. Considering the detection process is a Poisson process, the probability of observing y_i events in the ith bin is given by

$$y_i \sim Poisson(\vec{y}_i) \Rightarrow p(y_i|f) = e^{-\bar{y_i}} \frac{\bar{y_i}^{y_i}}{y_i!},\ i = \overline{1, N} \tag{3.17}$$

where $\bar{y_i}$ is the mean number of photons detected in bin i, being expressed as the sum of the mean number of photons emitted from all source pixels times the transition probabilities:

$$\bar{y_i} = \sum_{j=1}^{M} t_{ij} f_j \tag{3.18}$$

Assuming the number of detected photons in all bins independent variables, the likelihood function is

$$p(y|f) = \prod_{i=1}^{N} P(y_i|f) = \prod_{i=1}^{N} e^{-\bar{y_i}} \frac{\bar{y_i}^{y_i}}{y_i!} \tag{3.19}$$

Maximization of the likelihood function is equivalent to find the maximum of the log-likelihood function. The log-likelihood function can be expressed as follows

$$l(y|f) = \sum_{i=1}^{N} y_i \log(\bar{y_i}) - \bar{y_i} - \log(y_i!)) \tag{3.20}$$

$$= \sum_{i=1}^{N} (y_i \log(\sum_{j=1}^{M} t_{ij} f_j) - \sum_{j=1}^{M} t_{ij} f_j - \log(y_i!)) \tag{3.21}$$

According to the ML criterion, to estimate the source f giving the highest probability of generating y, is equivalent to find the maximum of $l(y|f)$. The existence of local maximum of the likelihood function is assured by the Kuhn-Tucker conditions. In addition, if the function is concave, the local maximum is a global maximum. The Kuhn-Tucker conditions of a solution f^* to maximize $l(y|f)$ are given by

$$\frac{\partial l(y|f)}{\partial f_j}|_{f=f^*} = \begin{cases} = 0 & \text{if } f_j^* \geq 0 \\ \geq 0 & \text{if } f_j^* = 0 \end{cases} \tag{3.22}$$

while the first and second derivatives of the log-likelihood function are

$$\frac{\partial l(y|f)}{\partial f_j} = \sum_i t_{ij} \left(\frac{y_i}{\sum_k t_{ik} f_k} - 1 \right) \tag{3.23}$$

$$\frac{\partial^2 l(y|f)}{\partial f_j \partial f_l} = -\sum_i \frac{t_{ij} t_{il} y_i}{(\sum_k t_{ik} f_k)^2} \tag{3.24}$$

A necessary and sufficient condition for a function to be concave is to have its Hessian negative semi-definite

$$\sum_j \sum_l c_j c_l \frac{\partial^2 l(y|f)}{\partial f_j \partial f_l} \leq 0 \tag{3.25}$$

for all vectors $c = \{c_1, c_2 \cdots c_N\}$, and all non-negative images $f \geq 0$. Considering the Equation (3.24), the inequality (3.25) is verified, resulting that the log-likelihood function is concave.

The straightforward way to find a local maximum of f is to compute its partial derivatives and to equal them to zero.

$$\frac{\partial l(y|f)}{\partial f_j} = -\sum_{i=1}^{N} t_{ij} + \sum_{i=1}^{N} \frac{y_i t_{ij}}{\sum_{j=1}^{M} t_{ij} f_j} \tag{3.26}$$

Note that $\sum_{i=1}^{N} t_{ij}$ is the detection sensitivity, which is the probability that a photon emitted from pixel j will be detected.

EM algorithm

Finding the maximum of Equation (3.26) is a difficult process because of its non-linearity, so the use of a numerical method is required. The iterative EM algorithm asymptotically achieves the ML of f. At each iteration, the EM algorithm consists of two parts. The first one is the expectation step (E-step), where the expectation of the likelihood function is obtained in terms of complete data, given the measurement y, and the estimation f^k from the previous iteration. The second one is the maximization step (M-step), where the estimation f^{k+1} of the current iteration can be obtained as the critical points of the expectation function calculated in the E-step.

To satisfy the requirement for a complete data set for the EM algorithm, the random variable z_{ij} is introduced as the unobserved data

$$z_{ij} = \begin{cases} 1, & \text{if event } j \text{ originated in bin } i \\ 0, & \text{otherwise} \end{cases} \tag{3.27}$$

The relation between the measurements and complete data $\hat{y_i}$ can be expressed

$$\hat{y_i} = \sum_{j=1}^{M} z_{ij} = \sum_{j=1}^{M} t_{ij} f_j \tag{3.28}$$

The log-likelihood in terms of complete data may be written

$$l(z_{ij}|f) = \sum_{i=1}^{N} \sum_{j=1}^{M} (z_{ij} \log(t_{ij} f_j) - t_{ij} f_j - \log(z_{ij}!)) \tag{3.29}$$

In the E-step, the conditional expectation of the log-likelihood with respect to the measured data, and the estimation f^k from the previous iteration is

$$E[l(z_{ij}|f)|y, f^k] = \sum_{i=1}^{N} \sum_{j=1}^{M} (N_{ij}^k \log(t_{ij} f_j) - t_{ij} f_j) \tag{3.30}$$

where

$$N_{ij}^k = E[z_{ij}|y_i, f^k] = y_i \frac{t_{ij} f_j^k}{\sum_{j=1}^{M} t_{ij} f_j^k} \tag{3.31}$$

In the M-step, the maximum estimate f^{k+1} can be computed by setting derivative of Equation (3.30) to zero:

$$\frac{\partial E[l(z_{ij}|f), y, f^k]}{\partial f_j} = \left[\frac{1}{f_j}\sum_i N_{ij}^k - \sum_i t_{ij}\right] |_{f=f^{k+1}} = 0 \tag{3.32}$$

where $\sum_{i=1}^{N} t_{ij} = s_j$ is the detection sensitivity.

3.1.2.3 Bayesian methods

ML based algorithms incorporate information about the Poisson nature of photons emission, and in addition the constraint of non-negativity. Other information possible to include may be the bounds of the solution as well as its derivatives up to a certain order. In case of Bayesian approach, the additional information is given by statistical properties of the object, e.g., the probability density of f denoted $p(f)$, and called prior. The joint probability density of (f, y) is given by

$$p(f, y) = p(y|f)p(f) \tag{3.33}$$

Introducing the marginal probability density of y, and applying the Bayes formula, the conditional probability density of f for a given value y is given by

$$p(f|y) = \frac{p(f, y)}{p(y)} = \frac{p(y|f)p(f)}{p(y)} \tag{3.34}$$

The MAP estimate of the source is defined as the function which maximizes the a posteriori probability density

$$f^* = \arg\max_{f \geq 0} p(f|y) \tag{3.35}$$

Considering the log of $p(f|y)$, the MAP estimator can be written

$$\phi(f) = l(y|f) + \log p(f) \tag{3.36}$$

which represents the sum of the log-likelihood and the log of the prior. Widely used priors are independent of the source values, or based on interaction models. The first class includes the Gaussian model [Huesman et al., 2000], which results in a quadratic form, the gamma prior [Lange et al., 1987] which allows non-negative values of source function. Independent priors can be derived based on the maximum entropy criterion [Liang et al., 1989]. The prior has the following general form

$$p(f) = \frac{1}{C}\prod_{i=1}^{N} e^{-f_i \log(f_i)} \tag{3.37}$$

where C is a normalization factor. These priors require the estimation of the mean values of the object, causing biased solutions. Priors using the Markov random models are known as Gibbs distributions. The Gibbs distribution has the following general form

$$p(f|\beta) = \frac{1}{C} e^{-\beta U(f)} \tag{3.38}$$

where $U(f)$ is the Gibbs energy function.

Using a priori information may be viewed as the integration of a 'penalty' term at each iteration. As the prior, the penalty term could generate the intended properties to the reconstructed images, e.g., the smoothness level. A challenge is to choose the optimal method of penalty application.

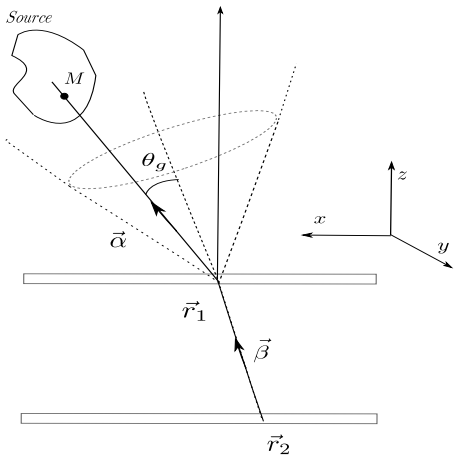

Figure 3.2: Illustration of the conic projection from the Compton scattering event generated by a point M of the source. The event is defined by the first interaction at the position $\vec{r}_1$, the position $\vec{r}_2$, and the Compton scattering angle θ_g. The dotted lines indicate the cone defined by the unit vector $\vec{\beta}$, and the Compton angle θ_g.

3.2 Inversion of Compton scattered data

In transmission and emission CT problems, the measured data are expressed as line integrals. In case of Compton scattered data reconstruction, the back-projection of a detected event leads to photon source localization on the surface of a cone (see Section 2.2.4).

In the following, the analytical as well as the iterative approaches proposed to reconstruct data generated by a Compton scattering based detector are presented. Analytical methods were investigated using deterministic data; herein, the method proposed by [Cree and Bones, 1994] is detailed, considering the most simplistic model of Compton scattering camera. Iterative methods allow integration of measurement uncertainties in on a straightforward manner. Therefore, ML based estimation and related penalized likelihood versions are widely applied. Even if analytic methods have generally several disadvantages in comparison to their iterative counterparts, they are nevertheless important for the insight they bring into the Compton image reconstruction problem.

3.2.1 Analytical methods

Consider the generic Compton camera presented in Section 2.2.1. The measured data g are expressed as the integration of the photon source distribution over the surface of the cone defined by r_1, r_2 and θ_g (Figure 3.2). This quantity, labeled $g(r_1, \vec{\beta}, \theta_g)$, is called cone-surface projection, which has the form

$$g(r_1, \vec{\beta}, \theta_g) = \int_{\text{cone}} w f dS \tag{3.39}$$

where w is the weighing factor issued from geometrical considerations, described by e.g., Klein-Nishina cross-section. Here, the photons source of intensity function f is a positive and real valued function with compact support.

Consider

- the unit vectors $\vec{\alpha}$, $\vec{\beta}$, which satisfy the realation $\vec{\alpha} \cdot \vec{\beta} = \cos\theta_g$
- with respect to the cone axis, θ_g and ϕ are the polar and the azimuthal angles, respectively, describing $\vec{\alpha}$, thus $\vec{\alpha} = \vec{\alpha}(\vec{\beta}, \theta_g, \phi)$
- r is the distance from the apex to a given point of the cone

then the cone-surface projection has the form

$$g(r_1, \vec{\beta}, \theta_g) = K(\theta_g) \int_0^{2\pi} \int_0^{\infty} f(r_1 + \vec{\alpha} \cdot r) r \sin\theta_g dr d\phi \tag{3.40}$$

where $K(\theta_g)$ is the Klein-Nishina distribution for Compton scattering. The image reconstruction problem is to determine f given $g(r_1, \vec{\beta}, \theta_g)$.

The first attempt to directly invert Compton data was proposed by [Cree and Bones, 1994], where the solution is limited to cases when the scattering direction is perpendicular to the second detector, leading to a dramatic loss of data. [Basko et al., 1999] formulated an analytical inversion formula of Compton projections without considering the distribution of possible scattering angles. The cone surface projections are transformed into plane projections using spherical harmonics, which allow the application of the Radon transform, as in case of CT inversion problems. The formulation by spherical harmonics considers that each detector pixel is the center of an unit sphere independently of the detector geometry design. [Parra, 2000] completes the previous work by deriving an analytical formula considering the probability of scattering at different angles based on the Klein-Nishina formula. [Gunter, 2006] applied a fast FBP algorithm to the inversion problem assuming detectors which should be sensitive to scattering angles from 0° to 180° degrees. In practice, a Compton camera usually can not provide the complete set of scattering angles due to geometry limitations. [Tomitani and Hirasawa, 2002] proposed a solution to the direct inversion problem including this limitation. However, besides the spatially variant and incomplete sampling, the angular uncertainty needs aslo to be included into the image reconstruction algorithm.

3.2.1.1 Inversion of the restricted cone-surface projection

In the following, the algorithm developed by [Cree and Bones, 1994] is presented. The cone-projection is developed as follows: the scattering detector surface is taken to extend over the xy-plane, $r_1 = (x, y, 0)$. Then, the cone-surface projection reduces to

$$g(r_1, \vec{\beta}, \theta_g) = K(\theta_g) \int_0^{2\pi} \int_0^{\infty} f(x + r\alpha_x, y + r\alpha_y, r\alpha_z) r \sin\theta_g dr d\phi \tag{3.41}$$

where $\vec{\alpha} = (\alpha_x, \alpha_y, \alpha_z) = (\sin\theta_g \cos\phi, \sin\theta_g \sin\phi, \cos\theta_g)$.

[Cree and Bones, 1994] considers only the subset of cone-surface projections where $\vec{\beta} = z$. The cone-surface projection is now denoted as the restricted cone-surface projection, $g(x, y, \theta_g)$. Knowing $z = r\cos\theta_g$, the restricted cone-surface projection is given by

$$g(x, y, \theta_g) = K(\theta_g) \frac{\sin\theta_g}{\cos^2\theta_g} \int_0^{2\pi} \int_0^{\infty} f(x + z\tan\theta_g \cos\phi, y + z\tan\theta_g \sin\phi, z) z dz d\phi \tag{3.42}$$

Denoting $\tan\theta_g = t$, the restricted cone-surface projection has the form

$$g(x, y, t) = K(t) t\sqrt{1 + t^2} \int_0^{2\pi} \int_0^{\infty} f(x + zt\cos\phi, y + zt\sin\phi, z) z dz d\phi \tag{3.43}$$

The restricted cone-surface projection can be analytically inverted, and the inversion is stated by the following theorem:

Theorem 3.2.1 *From a complete set of restricted cone-surface projections, i. e., $g(x, y, t)$ for $(x, y) \in R^2$ and $t \in [0, \infty)$, the gamma ray source distribution $f(x, y, z)$ can be reconstructed.*

Proof The inversion is performed in the Fourier space

$$G_2(u, v, t) = \mathcal{F}_2[g(x, y, t)] \tag{3.44}$$

$$F_2(u, v, t) = \mathcal{F}_2[f(x, y, t)] \tag{3.45}$$

where $\mathcal{F}_2$ denotes the 2D Fourier transform.

Consider $\mathcal{F}_2$ acts on both sides of Equation (3.43), and apply the Fourier shift theorem

$$G_2(u,v,t) = K(t)t\sqrt{1+t^2}\int_0^{2\pi}\int_0^{\infty} F_2(u,v,z)e^{2\pi izt(u\cos\phi+v\sin\phi)}zdzd\phi \tag{3.46}$$

By expressing the rectangular coordinate pair (u,v) in terms of the polar coordinates pair (ρ,φ) in Equation (3.46), the ϕ-integral is recognizable as the standard integral definition of the zero-order Bessel function of the first kind.

$$G_2(u,v,t) = K(t)t\sqrt{1+t^2}2\pi\int_0^{\infty} F_2(u,v,z)\mathcal{J}_0(2\pi zt\sqrt{u^2+v^2})zdz \tag{3.47}$$

The z-integral is a zero-order Hankel transform acting on F_2.
Letting $\xi = z\sqrt{u^2+v^2}$ allows to write

$$G_2(u,v,t) = \frac{K(t)t\sqrt{1+t^2}}{u^2+v^2}\mathcal{H}_0[F_2(u,v,\frac{\xi}{\sqrt{u^2+v^2}})](\xi\to t) \tag{3.48}$$

The Hankel transform is self-reciprocal, so

$$F_2\left(u,v,\frac{\xi}{\sqrt{u^2+v^2}}\right) = \mathcal{H}_0[\frac{u^2+v^2}{K(t)t\sqrt{1+t^2}}\Lambda_2(u,v,t)](t\to\xi) \tag{3.49}$$

where care must be taken to exclude $t=0$.

An inverse Fourier transform will give f, however the transform has to be performed on the surface defined by $z = \frac{\xi}{\sqrt{u^2+v^2}}$ in the (u,v,z)-space.

3.2.1.2 Inversion of the Compton transform using the full set of available projections

Reconsider that the solution proposed by [Cree and Bones, 1994] assumes the scattered gamma-ray direction perpendicular to the detectors. In the following, an approach towards an inversion formula of the cone-surface projections using the full set of data possible to measure is presented. A slightly modified model of Compton projections is adopted [Maxim et al., 2009], namely

$$g'(u_1,u_2,\omega,\psi,\theta_g) = w\int_{M\in\mathcal{C}(u_1,u_2,\omega,\psi,\theta_g)} f(M)\cos\Theta dS \tag{3.50}$$

where Θ denotes the polar angle of the cone's points M, while $\omega\in[0,\pi/2)$, and $\psi\in[0,\pi)$ denote the polar angle and the azimuthal angle of the cone's axis, respectively (Figure 3.3 (a)). The model of Compton projections is based on the model proposed by [Gunter, 2006], and it assumes that the projections $g'(\cdot,\cdot,\omega,\psi,\theta_g)$ of a source of intensity f, described by a point $(u_1,u_2)\in\mathbb{R}^2$, are proportional to the integral of the incoming flux intensity on the surface of the cone $\mathcal{C}(u_1,u_2,\omega,\psi,\theta_g)$.

The solution proposed by [Cree and Bones, 1994] can be now described as follows

$$g(x,y,\theta_g) = g'(x,y,0,0,\theta_g) \tag{3.51}$$

The parametric expression of the Compton projections writes

$$\begin{aligned} g'(u_1,u_2,\omega,\psi,\theta_g) = K(\theta_g)\int_0^{\infty}\int_0^{2\pi} f(u_1+zc(\omega,\theta_g)+za(\omega,\theta_g)\cos\phi,\\ u_2+zb(\omega,\theta_g)\sin\phi,z)zb(\omega,\theta_g)d\phi dz \end{aligned} \tag{3.52}$$

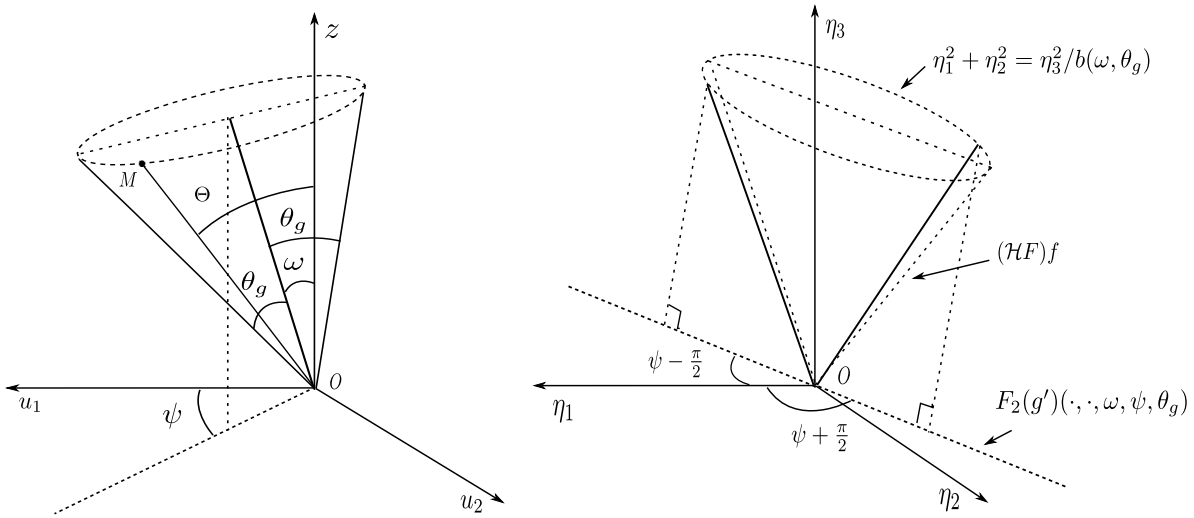

(a) Spatial domain. Cone $\mathcal{C}(0,0,\omega,\psi,\theta_g)$.

(b) Fourier domain. Cone $\mathcal{C}_{\mathcal{F}}(\omega,\theta_g)$.

Figure 3.3: (a) Spatial domain. The Compton projections are the result of the integration on the surface of the cones, which present parallel axes, and the same Compton angle θ_g. Each cone is a translation of the cone $\mathcal{C}(0,0,\omega,\psi,\theta_g)$. (b) Fourier domain. The dashed line represents a line of the Fourier transform of the Compton projections. The solid line represents one slice of the Hankel-Fourier transform of f on the surface of the cone $\mathcal{C}_{\mathcal{F}}(\omega,\theta_g)$.

where

$$a(\omega,\theta_g) = \frac{\sin\theta_g\cos\theta_g}{\cos^2\omega-\sin^2\theta_g}, \tag{3.53}$$

$$b(\omega,\theta_g) = \frac{\sin\theta_g}{\sqrt{\cos^2\omega-\sin^2\theta_g}}, \tag{3.54}$$

$$c(\omega,\theta_g) = \frac{\sin\omega\cos\omega}{\cos^2\omega-\sin^2\theta_g} \tag{3.55}$$

The quantities $za(\omega,\theta_g)$ and $zb(\omega,\theta_g)$ are respectively the major and minor half-axes of the ellipse describing the projections, while $zc(\omega,\theta_g)$ represents the distance from the center of the ellipse to the vertical axis Oz.

The inversion is derived similarly to [Cree and Bones, 1994], yielding the following formula

$$\begin{aligned} f(x,y,z) = \int_{-\infty}^{\infty}\int_{-\infty}^{\infty}\int_{0}^{\frac{\pi}{2}-\omega} \frac{b'_{\theta_g}(\omega,\theta_g)}{K(\theta_g)} F_2(g')(\eta_1,\eta_2,\omega,\vartheta+\epsilon\frac{\pi}{2},\theta_g) \\ \mathcal{J}_0(2\pi z b(\omega,\theta_g)\sqrt{\eta_1^2+\eta_2^2}) d\theta_g \\ \exp(2\mathbf{i}\pi(x\eta_1+y\eta_2))(\eta_1^2+\eta_2^2)d\eta_1 d\eta_2 \end{aligned} \tag{3.56}$$

where

$$b'_{\theta_g}(\omega,\theta_g) = \frac{\cos^2\omega\cos\theta_g}{(\cos^2\omega-\sin^2\theta_g)^{3/2}} > 0 \tag{3.57}$$

Only a set of projections is considered, namely projections for which the axis has the azimuthal angle of $\psi = \vartheta + \epsilon\pi/2$, where $\epsilon = \pm 1$, and ϑ denotes the polar angle of an arbitrary fixed point (η_1,η_2) in

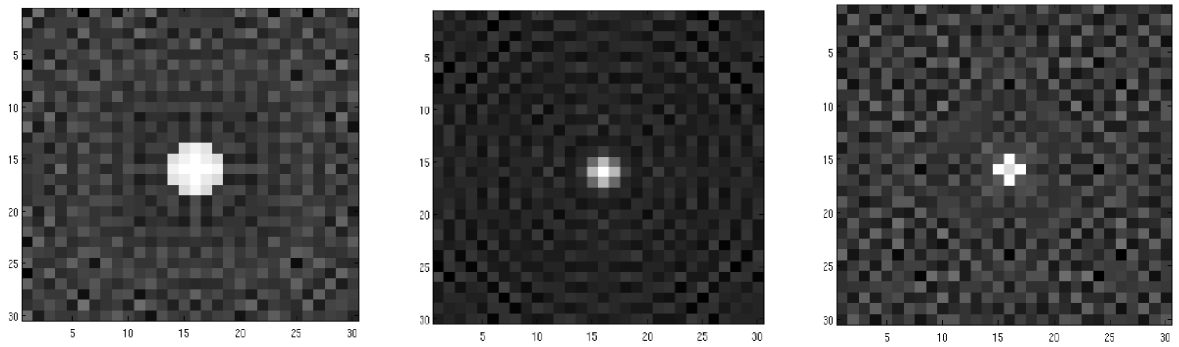

$\omega = 0\ z = 5\ r = 2.5$ $\omega = 0\ z = 3\ r = 1.5$ $\omega = 0\ z = 7\ r = 1.5$

Figure 3.4: Spherical source situated at $(0.5, 0.5, 5)$, radius $R = 2.5$ units. Detector of size 30×30 units at $z = 0$. One slices is represented for $\omega = 0$ corresponding (from the first to the third column) to $z = 5$ (center of the sphere), $z = 3$ (not empty intersection, close to the detector) and $z = 7$ (the same distance from the center of the sphere, but further from the detector). The intersection between the sphere and the horizontal plane is a disc with radius r.

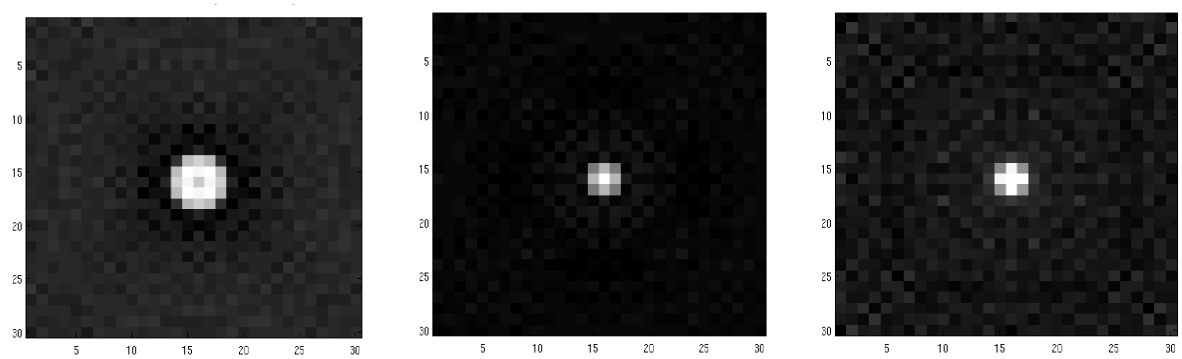

$\omega = \pi/6\ z = 5\ r = 2.5$ $\omega = \pi/6\ z = 3\ r = 1.5$ $\omega = \pi/6\ z = 7\ r = 1.5$

Figure 3.5: Spherical source placed at $(0.5, 0.5, 5)$, radius $R = 2.5$ units. Detector of size 30×30 units at $z = 0$. One slice is represented for $\omega = \pi/6$ corresponding (from the first to the third column) to $z = 5$ (center of the sphere), $z = 3$ (not empty intersection, closer to the detector) and $z = 7$ (the same distance from the center of the sphere, but further from the detector). The intersection between the sphere and the horizontal plane is a disc with radius r.

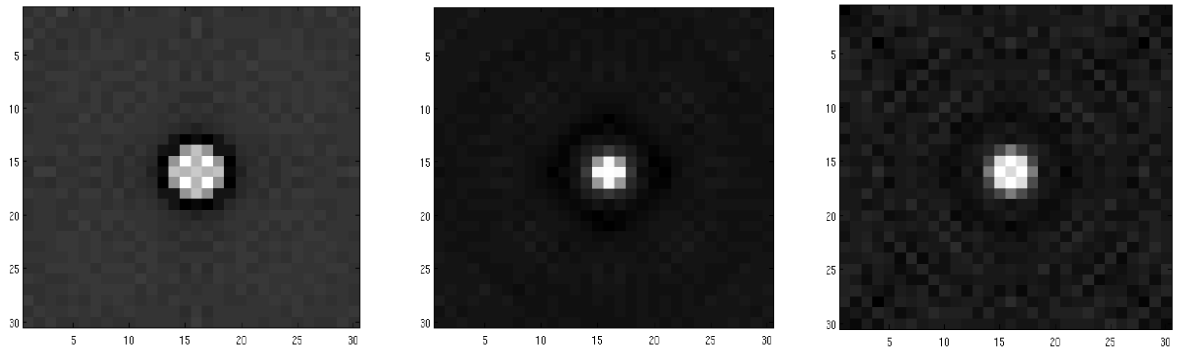

$\omega = \pi/3\ z = 5\ r = 2.5$ $\omega = \pi/3\ z = 3\ r = 1.5$ $\omega = \pi/3\ z = 7\ r = 1.5$

Figure 3.6: Spherical source placed at $(0.5, 0.5, 5)$, radius $R = 2.5$ units. Detector of size 30×30 units at $z = 0$. One slice is represented for $\omega = \pi/3$ corresponding (from the first to the third column) to $z = 5$ (center of the sphere), $z = 3$ (not empty intersection, closer to the detector) and $z = 7$ (the same distance from the center of the sphere, but further from the detector). The intersection between the sphere and the horizontal plane is a disc with radius r.

the Fourier space (Figure 3.3 (b)). The discrete form of the inversion formula may be found in [Maxim et al., 2009].

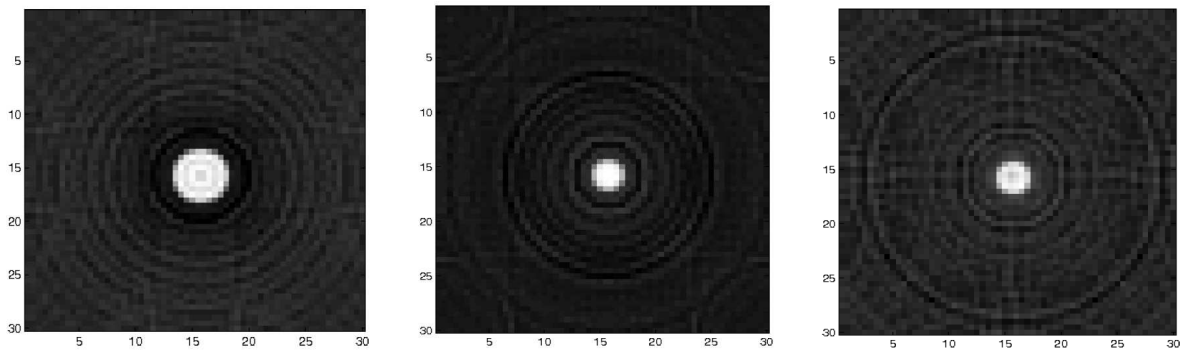

$\omega = \pi/6\ z = 5\ r = 2.5$ $\omega = \pi/6\ z = 3\ r = 1.5$ $\omega = \pi/6\ z = 7\ r = 1.5$

Figure 3.7: Spherical source of radius $R = 2.5$ placed in front of a detector of 30×30 units and 60×60 pixels. The artifacts due to the finite dimension of the detector are reduced compared to Figures 3.4, 3.5.

In the following, several numerical experiments are presented, using simple, mathematical tractable source conditions. The scatter detector is sampled on a discrete grid, considering only the center of a pixel is sensitive and receives information. For spherical sources, Formula (3.52) may be partly calculated analytically: for a fixed angle ϕ, the values of the z coordinates of the points of the cone belonging to the source are solutions of a second order inequality defining the sphere and its interior. Thus an interval depending on ϕ is obtained. Since the considered sources are of uniform intensity 1, the integral in z is just the length of this interval, and only discretisation in ϕ is required.

In most of the tests a scatter detector of size 30×30 units divided in equal square pixels situated in the plane $z = 0$ is considered. The center of the coordinate system is placed at the center of the scatterer.

The sampling in θ_g is equispaced, covering the interval $(0, \pi/2 - \omega)$. The disadvantage of this choice is to suppose that the energy resolution of the detector depends on ω. Also, the integration step is not constant from one value of ω to another. The energy resolution of the absorber, except the one induced by the discretization scheme in θ_g, is not considered. A simple rectangle method was considered herein.

Figures 3.4, 3.5, 3.6 show three reconstructed slices of a sphere with radius $R = 2.5$ and center situated at $(0.5, 0.5, 5)$. Following the altitude of the cut, the expected result is a disc with radius r as indicated downside each image. As ω grows, the reconstructed radius is slightly larger than expected, especially in the in the upper slice, due to the finite size of the scatter detector and border effects.

A finer sampling of the detector is considered for the numerical test from Figure 3.7. A spherical source of radius $R = 2.5$ units was placed at a distance of $z = 5$ units from a scatter detector, whose size was 30×30 units sampled in 60×60 pixels [Maxim et al., 2009].

3.2.2 Iterative methods

The section presents an overview of iterative methods applied to Compton scattering data reconstruction. The presentation is not an exhaustive description of all proposed reconstruction methods, but an illustration of the principal approaches adopted to attain an efficient Compton data reconstruction. The methods are presented without references about the configuration of the Compton camera. Note that all algorithms were applied using projection data generated according to a particular geometry of the detector.

Reconsider the view of Compton image reconstruction as a two stage method. The first stage includes Compton data back-projection, while the second step improves the initial back-projected image by applying an iterative algorithm. The latter includes mostly algorithms which were previously used to reconstruct PET, or SPECT data. The early approach proposed the application of ART algorithms [Singh and Doria, 1983b]. Afterwards, MLEM based algorithms were widely used for Compton reconstruction [Sauve et al., 1993], [Wilderman et al., 1998a].

Computation of the maximal solution by direct resolution of Equation (3.26) is a complicated process

since the equation is not linear. A possible alternative is to achieve asymptotically the ML of f by an iterative algorithm. A commonly used approach is the EM algorithm. In the first step, i.e. the E-step, the expectation of the likelihood function is obtained from the complete data given the measurement y and the estimation of f from the previous iteration. The second step called the M-step, maximize the expectation of the current iteration by solving the derivatives of the expectation functions from the E-step. The iterative ML-EM formula has the following form

$$f_j^{k+1} = \frac{f_j^k}{\sum_{i=1}^N t_{ij}} \sum_{i=1}^N \frac{y_i t_{ij}}{\sum_{b=1}^M t_{ib} f_b^k} \tag{3.58}$$

where $\sum_{i=1}^N t_{ij} = s_j$ is the detection sensitivity.

An accelerate version of the EM algorithm is adopted by [Kim et al., 2007], analyzing several methods to group the conical projection data into ordered subsets. The OSEM algorithm applies the EM algorithm to each sub-objective function. The update equation has the form

$$f_j^{(k,l+1)} = \frac{f_j^{(k,l)}}{\sum_{i \in S_l} t_{ij}} \sum_{i \in S_l} \frac{y_i t_{ij}}{\sum_{b=1}^M t_{ib} f_b^{(k,l)}} \tag{3.59}$$

where $f_j^{(k,l)}$ denotes the image estimate at the kth iteration and lth subset, while S_l denotes the lth subset. All the proposed versions of the OSEM algorithm overrun the classical EM algorithm, while it preserves the same overall quality.

The reconstruction problem can be reformulated in a Bayesian framework, including a prior distribution on the image. The prior reflects characteristics of image, e.g., the smoothness degree. The image is computed as the MAP estimate from the posterior density for the image conditioned on data. A Bayesian framework approach is investigated in [Lee, 2008]. The cost function is a maximum a posteriori estimate, while the iterative algorithms are firstly, a row-action method and secondly, a block-sequential method, which is a relaxed version of the OSEM method. The regularization is done by using a convex non-quadratic smoothing prior. The prior information reflects assumptions about the spatial distribution of the source. Both algorithms are applied in their binned-data version.

When considering Row-Action ML Algorithm (RAML), the projection data are ordered in a sequence of p disjoint subsets S_l, $l = \overline{1,p}$. The update equation has the form

$$f_j^{(k,l+1)} = f_j^{(k,l)} - \epsilon_k f_j^{(k,l)} \sum_{i \in S_l} t_{ij} \left(1 - \frac{y_i}{\sum_j t_{ij} f_j^{(k,l)}} \right), \quad l = \overline{1,p} \tag{3.60}$$

where $f^k = f^{(k,p)}$, $f^{k+1} = f^{(k+1,p)}$, and ϵ_k represents a sequence of positive relaxation parameters, which are fixed throughout a complete cycle of the subsets.

Block-Sequential EM algorithm (BSEM) with regularization consists of two steps, an update of ML using RAML, and a secondary update in the gradient direction of the prior.

1.
$$f_j^{(k,l+1)} = f_j^{(k,l)} - \epsilon_k f_j^{(k,l)} \sum_{i \in S_l} t_{ij} (1 - \frac{y_i}{\sum_j t_{ij} f_j^{(k,l)}}), \quad l = \overline{1,p} \tag{3.61}$$

2. Set $f^{k+1/2} = f^{(k,p)}$ and compute

$$f^{k+1} = f^{k+1/2} - \epsilon_k D^k \bigtriangledown E_p(f^{k+1/2}) \tag{3.62}$$

where D^k is the diagonal matrix, $D^k = diag(f^{k+1/2})$.

The algorithms are similar to the J. Fessler's versions, e.g., [Fessler and Hero, 1994].

[Wilderman et al., 1998a] derived the MLEM algorithm in list-mode, and applied it to Compton data, resulting in a significant computational advantage over approaches using binned projection data. The algorithm is presented in Section 5.1.

Compton scattering data reconstruction proved a necessary asses in imaging far-field point sources. The Bayesian technique including the maximum entropy prior was applied by [Strong et al., 1990] to reconstruct COMPTEL data. Both ML and ME based estimations consider the pixel size constant in the reconstruction, rendering "the biggest errors under the brightest sources" [Dixon et al., 1996]. A way to overcome the pixel size constraint, the notion of pixon was introduced, representing a generalized, flexible pixel. Pixon based methods allow to change the model, e.g., the system response, parameters according to the information available in the measured data. The application of a method version in case of COMPTEL data is reported in [Dixon et al., 1996].

Chapter 4

A tracking Compton imaging system for hadron therapy

A novel detection method based on Compton scattering process is proposed as solution to gamma-rays imaging during hadron-particle therapy [Frandes et al., 2010c]. Imaging gamma rays emitted during target irradiation by hadron beams is a way to verify the location of the deposed dose.

First, the dose distribution as well as the generated particles are analyzed, considering a simplified hadron therapy scenario. Section 4.1 describes the emission of gamma rays during the first second of the irradiation, while Section 4.2 presents the projections of their origin emission at different energy bands.

In the following, an instrument operating in the required energy regime, called MEGA prototype ("Medium-Energy Gamma-ray Astronomy") is introduced. MEGA was the first fully calibrated and successfully operating combined Compton and pair telescope, capable of measuring gamma rays in the energy range from roughly 400 keV up to 50 MeV. Based on the MEGA prototype measurement principle, an advanced Hadron Therapy Imaging HTI system model was designed and optimized for detection of gamma rays in the Compton energy regime. It is capable of tracking a gamma ray through several Compton interactions until it is stopped via photoelectric effect, and also of tracking recoil electrons. The Compton scatter angle of the first interaction and the positions of the first two interactions allow to restrict the direction of the incident gamma ray to a cone surface. The reconstruction of the recoil electron direction enables to further restrict the origin distribution to a cone segment.

Section 4.3 introduces the proposed detection technique based on Compton gamma-ray tracking and describes the design of the HTI system as well as its simulated performance. Section 4.3.6 presents the reconstructed images of Compton scatter events simulated with the HTI system. Section 4.3.7 discusses the impact of the used imaging algorithm on the presented results. Conclusions are presented in Section 4.4.

4.1 Simplified hadron therapy scenario

Monte Carlo simulations were performed using the Geant4 package [Agostinelli et al., 2003] (version 9.1) with its front end Cosima [Zoglauer et al., 2006]. The Geant4 Livermore package including the Doppler-broadening extension G4LECS [Kippen, 2004] was used for electromagnetic interactions, and the standard QGSP-BIC-HP physics list for hadronic interactions. The considered simulation configuration consists of a PMMA ($C_5H_8O_2$) phantom, which was irradiated by three mono-energetic pencil proton beams with an intensity fixed at 10^6 protons/second. The start point of beam is along y-axis at -7.5 cm. The phantom is a sphere with 7.5 cm radius centered at 41.5 cm on z-axis (Figure 4.1).

Figure 4.2 illustrates depth dose deposition of three energies proton beams in the PMMA phantom. Fragments mostly travel in forward direction at almost the same rate as the incident ions. They can cause further fragmentation reactions. In contrast, the target nuclei remain approximately at the interaction

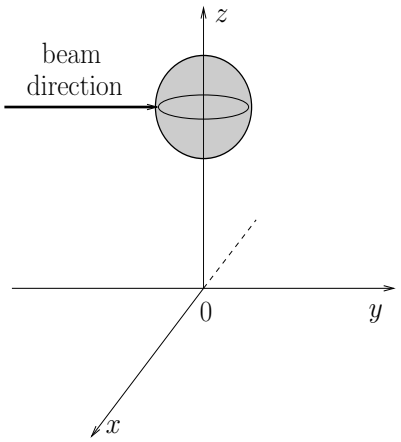

Figure 4.1: Schematic representation of the setup used for gamma ray emission simulations. The center of phantom represented by a PMMA sphere is situated at z = 41.5 cm.

position (Figure 4.2). Figure 4.3 shows the 2D dose deposition profiles of 70, 100, and 140 MeV proton beam into the phantom. The first line represents the xy-projections for the three proton beam energies, the second line represents the xz-projections, and the third line shows the yz-projections, considering $z = 0$, $y = 0$, and $x = 0$, respectively.

Dose distribution of hadron beams is due to both primary and secondary particles. The secondary

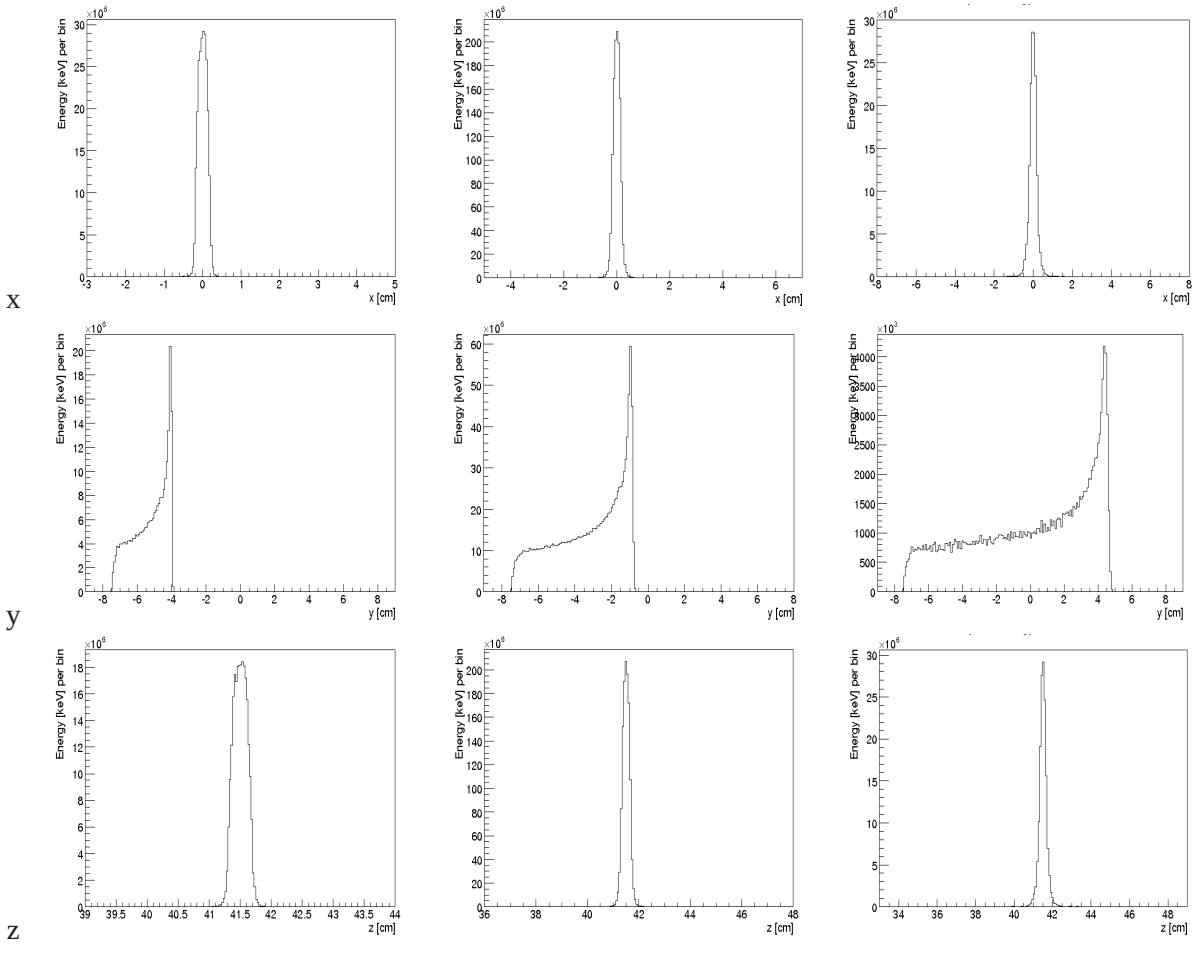

Figure 4.2: Dose deposition profiles of (a) 70 MeV, (b) 100 MeV, and (c) 140 MeV proton beam into a phantom, which is represented by a PMMA sphere. The entrance point in the phantom is at $y = -7.5$ cm. The calculation was done by Monte Carlo simulations using Geant4.

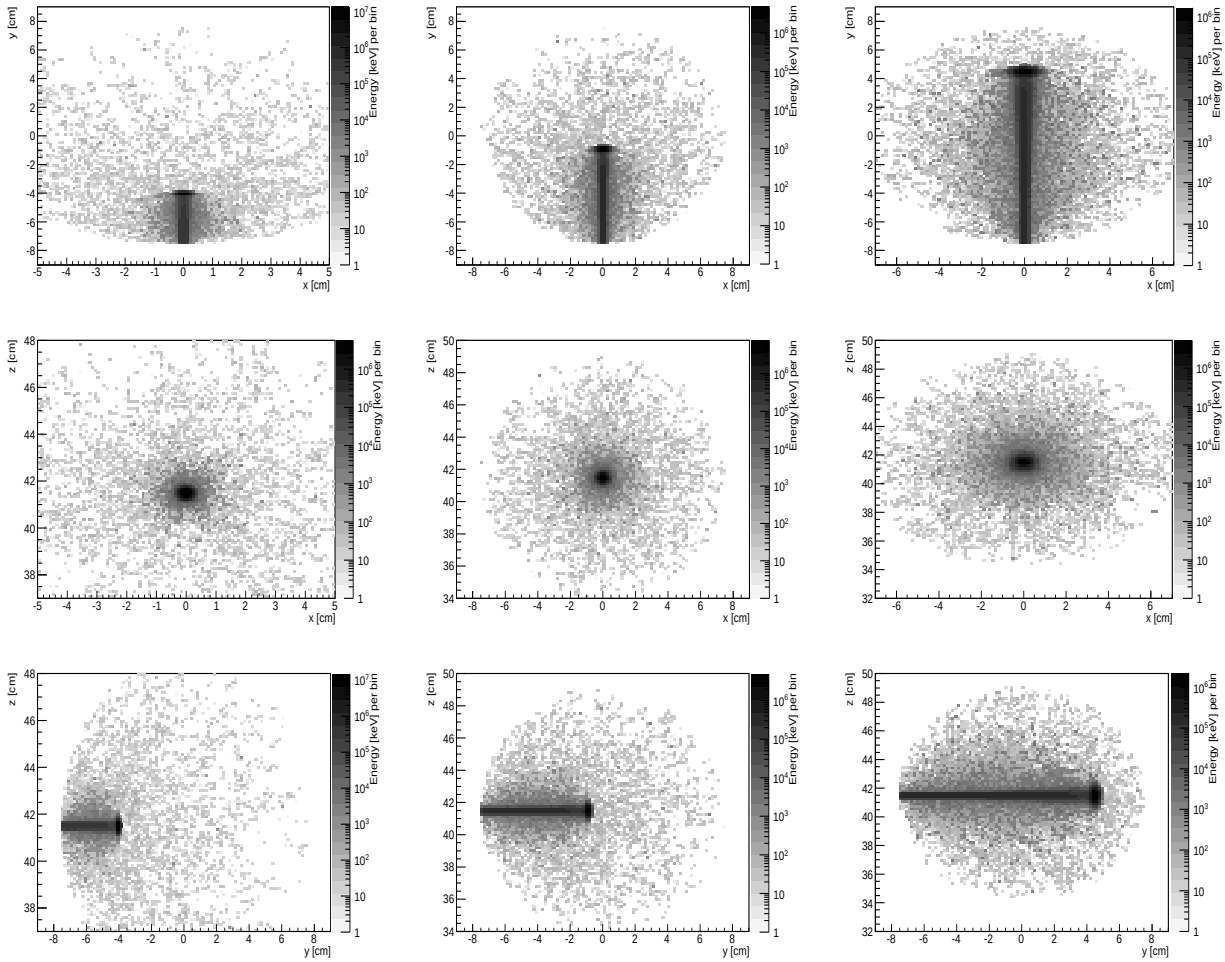

Figure 4.3: 2D Dose deposition profiles of (a) 70 MeV, (b) 100 MeV, and (c) 140 MeV proton beam into a phantom, which is represented by a PMMA sphere. The entrance point in the phantom is at $y = -7.5$ cm. The calculation was done by Monte Carlo simulations using Geant4.

particles are issued mainly from nuclear interactions, being important for the treatment plan calculation, regarding both dose deposition and RBE of the incident beams. Meanwhile, secondary neutrons may deliver dose outside the target volume, creating a less desirable effect. In its counterpart, emitted secondaries such as gamma rays following nuclear reactions can bring a valuable information about the location of the deposed dose during the treatment. In the following, emission location of secondaries which escape the PMMA phantom during the first second of proton beam irradiation are retrieved. The emission location as well as the energy spectrum of gamma rays which escape during phantom irradiation by the proton beam at 140 MeV are also analyzed.

Interactions occurring between the incident proton beam and the target determine emissions of various secondary particles, which further escape the phantom, e.g., β, e^-, e^+, n. Along with the primary particles, the emitted secondaries are also highly important for hadron therapy since they contribute to both deposed dose distribution, and RBE of the beam irradiation. Figure 4.4 shows the emission projections of secondary e^+ particles during the first second of irradiation by the proton beam at 140 MeV. The emission is isotropic, without presenting a well-defined pattern.

Figure 4.5 shows the emission projections of secondary n particles during the first second of irradiation by the proton beam at 140 MeV. The emission follows the proton beam path, presenting a continuous profile with a reduced fall-down at about the Bragg peak location, and a rather spread tail after it. The

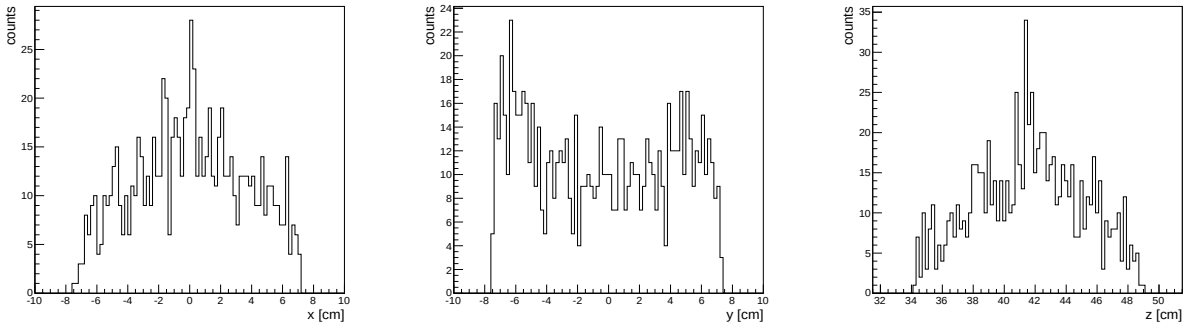

(a) (b) (c)

Figure 4.4: Profile projections of escaping e^+ particles during PMMA irradiation by a proton beam at 140 MeV. (a) x-projection ($y = 0$,$z = 0$), (b) y-projection ($x = 0$,$z = 0$), (c) z-projection ($x = 0$,$y = 0$).

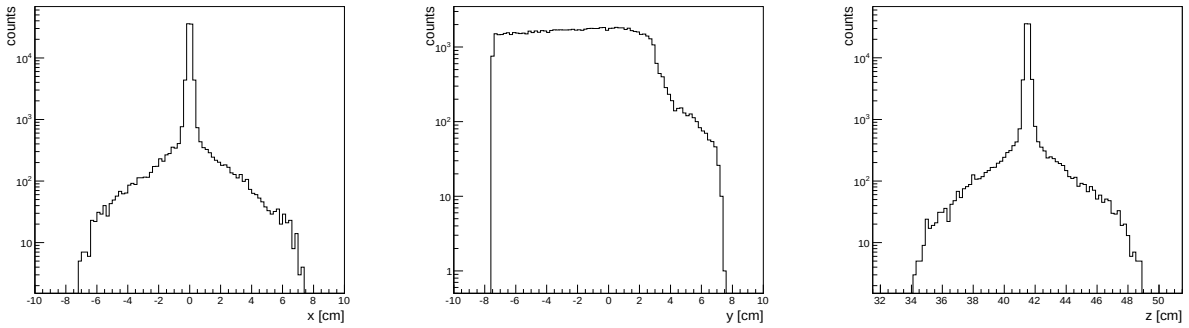

(a) (b) (c)

Figure 4.5: Profile projections of escaping n particles during PMMA irradiation by a proton beam at 140 MeV. (a) x-projection ($y = 0$,$z = 0$), (b) y-projection ($x = 0$,$z = 0$), (c) z-projection ($x = 0$,$y = 0$).

activity observed after the Bragg peak may cause dose deposition at undesired regions of the target volume. The other emitted particles present a lower activity in the first second of irradiation, and most of them are absorbed into the phantom.

Nuclear gamma rays issued from de-excitation of nuclei present an emission time less than a few nanoseconds, according to the nuclear state of the emitting nucleus (see Section 1.1.3.2). Moreover, correlation was observed between their origin emission profile and the dose distribution lateral profile. Figure 4.6 shows the dose deposition as well as the simulated distribution of originated nuclear gamma rays along the beam path for the first second of irradiation. Just before the proton comes to rest, a pronounced sharp profile of gamma-ray distribution can be observed. Hence, the profiles of dose distribution and emission location of escaping gamma rays are correlated.

The simulated energy spectrum of emitted gamma rays (i.e., those leaving the phantom) during the 140 MeV proton beam irradiation can be found in Figure 4.7. It shows a continuum ranging up to roughly 20 MeV and some nuclear lines. The most prominent lines are the 511 keV line from positron annihilation and the 4.4 MeV excitation line from carbon. The same nuclear lines can be observed for the other considered proton beam energies, e.g., 70 MeV and 100 MeV. The energy spectra of gamma rays depend on the energy states of the excited nuclei. Therefore an unique spectrum is expected for each element composing the phantom.

Simulations indicate that during the first second of irradiation, roughly 10% of the protons at 70 MeV lead to gamma rays, which escape the PMMA phantom isotropically. When the beam energy is 140 MeV,

the number of gamma photons increases to roughly 30% of the delivered protons.

The distribution of emitted particles is a function of their origin position. Obviously, close to the entry position of the beam into the phantom lower energy gamma rays can more easily escape the phantom. In addition, simulations show an increased concentration of escaping gamma rays with energies above 1 MeV close to the Bragg peak. Gamma rays with energies between 1 MeV and 10 MeV represent the dominant emission during the irradiation, with an intensity peak at the location of the Bragg maximum.

The time considered is the first second of irradiation. Note that gamma-ray emission issued from β^+-activity is unlikely due to rather long β-decays time. Therefore, the 'prompt emission' is the main gamma-ray activity in the considered time interval. Additional description of the gamma ray emission during proton beam irradiation is presented in Section 4.2.

4.2 Projections of gamma ray emission

Consider the simulation configuration presented in Section 4.1. The 2D emission projections of gamma-rays which escape the phantom during the first second of irradiation by the proton beam at three different energies are presented. Firstly, the origin position of the gamma rays leaving the phantom during the first second of irradiation without energy range restriction are shown. In this case, origin means either the creation location, if the gamma ray left the phantom unscattered, or the last scatter position (last position of direction change), if the gamma ray was subject to e.g., a Compton scatter. Figures 4.8, 4.12, 4.16 show the projections in case of proton beam at 70 MeV, 100 MeV, and 140 MeV, respectively.

Protons collisions generate radioactive elements, which have a certain life-time, i.e., decay after a given time, e.g., 121.8 s for ^{15}O, 1222.8 s for ^{11}C, 19.3 s for ^{10}C. Thus in the first second of irradiation, most of the annihilation photons are from pair production, which appear somewhere within the phantom. Figures 4.9, 4.13, 4.17 shows the origin position of the gamma rays at 511 keV leaving the phantom during the first second of irradiation, in case of proton beam at 70 MeV, 100 MeV, and 140 MeV, respectively. Only over the time, an increasingly strong component of gamma rays from β-decays is released within the proton beam path.

Considering the energy interval [2 MeV, 8 MeV], gamma rays leaving the phantom are presented in Figure 4.10, 4.14, 4.18. When including the energy interval restriction of [8 MeV, 30 MeV], emission projections of gamma rays leaving the phantom in the first second of irradiation are presented in Figure 4.11, 4.15, 4.19 for the three proton beam energies, respectively.

The origin emission pattern of gamma rays which leave the PMMA phantom within the first second of proton beam irradiation may be approximated to a 'line'. The energy spectrum of the line emission presents the lowest energy, e.g., below 500 keV, at the beginning of the path. Gamma rays at energy ranges, e.g., between 2 MeV and 8 MeV, are distributed all along the path with an intensity peak located

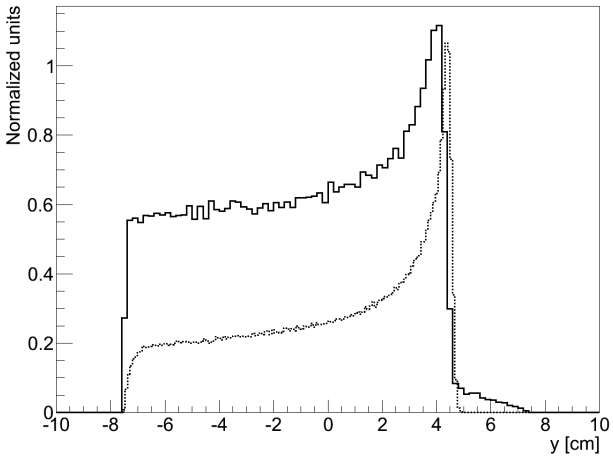

Figure 4.6: Simulated depth dose deposition profile (dotted line) and simulated depth distribution profile of originated nuclear gamma rays (solid line) in PMMA phantom for proton beam irradiation at 140 MeV. The start point of beam in PMMA is $y = -7.5$ cm.

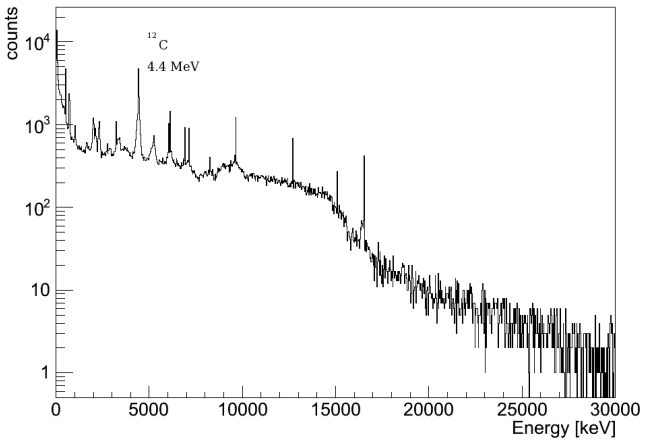

Figure 4.7: Simulated energy spectrum of gamma rays with energies below 30 MeV leaving the PMMA phantom during irradiation by a proton beam at 140 MeV.

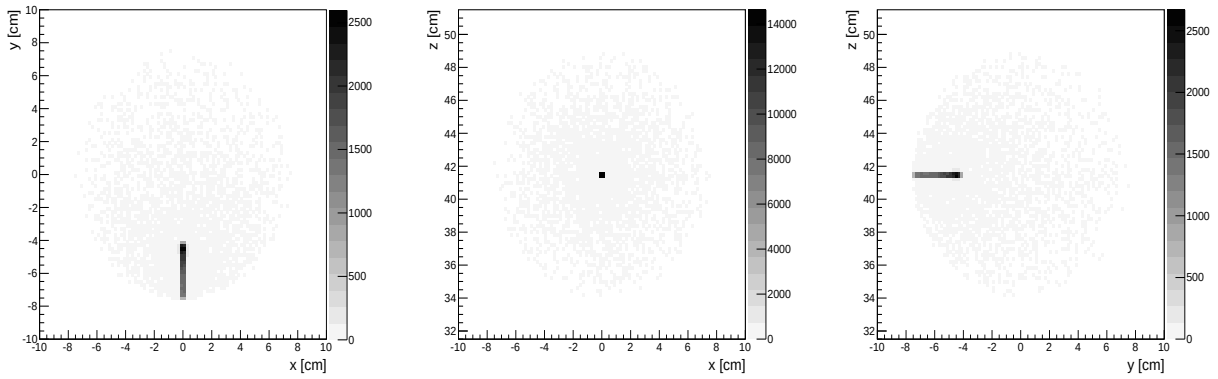

(a) (b) (c)

Figure 4.8: Simulated 2D images of (a) xy-projection, (b) xz-projection, (c) yz-projection of the emission location of gamma rays leaving the PMMA phantom during irradiation by the proton beam at 70 MeV.

at about 0.5 cm before the Bragg maximum. The highest energy range of the emitted gamma rays is concentrated at the Bragg peak location.

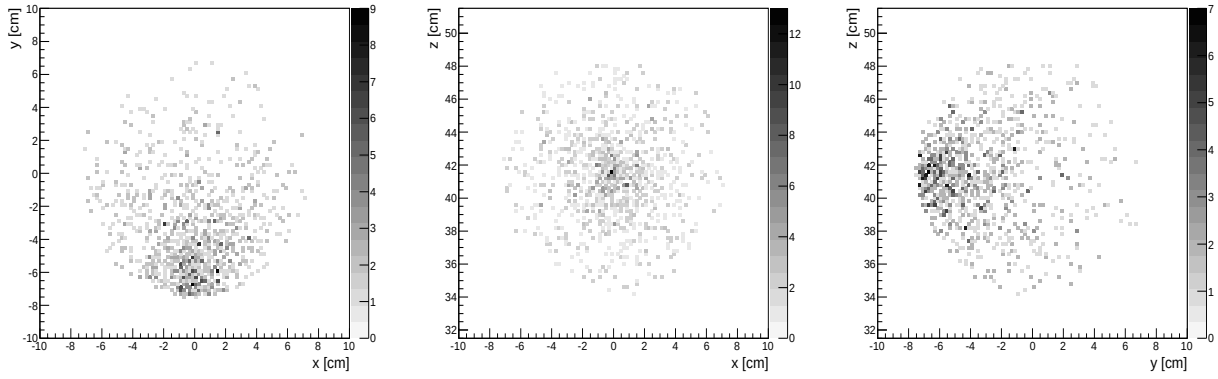

(a) (b) (c)

Figure 4.9: Simulated 2D images of (a) xy-projection, (b) xz-projection, (c) yz-projection of the emission location of gamma rays at 511 KeV energy, leaving the PMMA phantom during irradiation by the proton beam at 70 MeV.

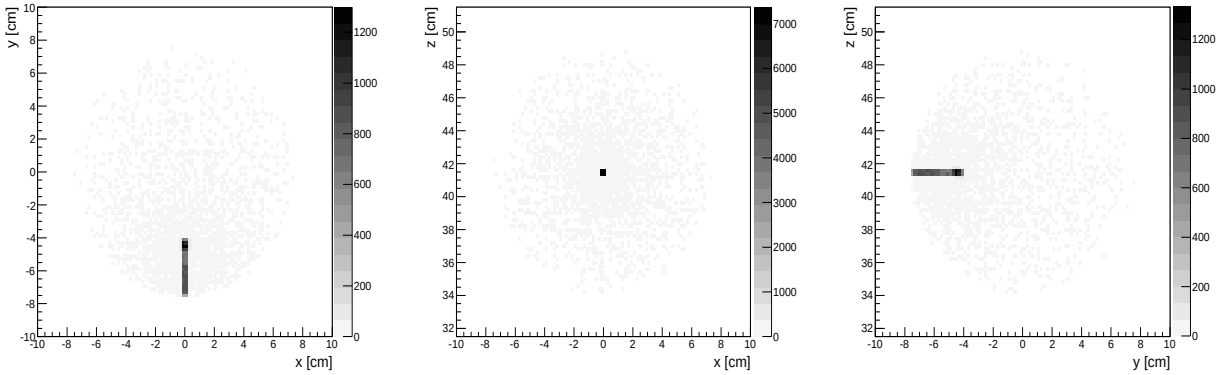

(a) (b) (c)

Figure 4.10: Simulated 2D images of (a) xy-projection, (b) xz-projection, (c) yz-projection of the emission location of gamma rays at energy interval [2 MeV, 8 MeV], leaving the PMMA phantom during irradiation by the proton beam at 70 MeV.

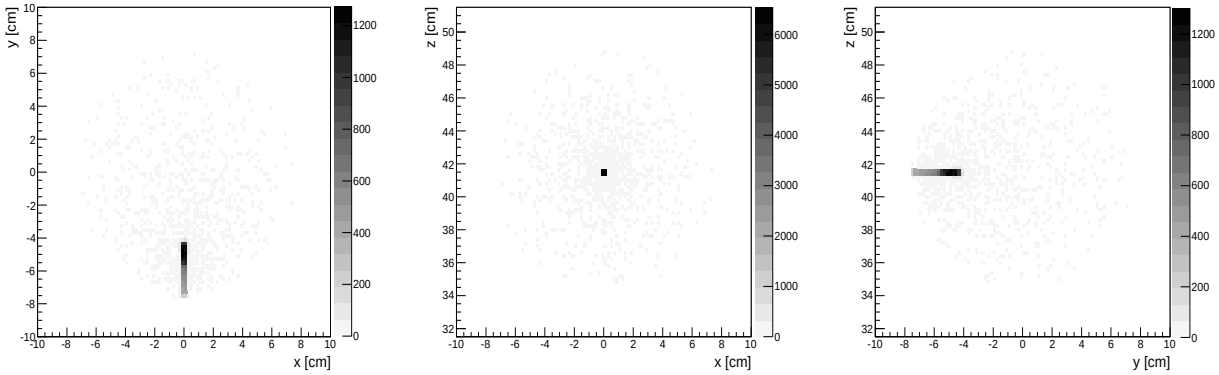

(a) (b) (c)

Figure 4.11: Simulated 2D images of (a) xy-projection, (b) xz-projection, (c) yz-projection of the emission location of gamma rays at energy interval [8 MeV, 30 MeV], leaving the PMMA phantom during irradiation by the proton beam at 70 MeV.

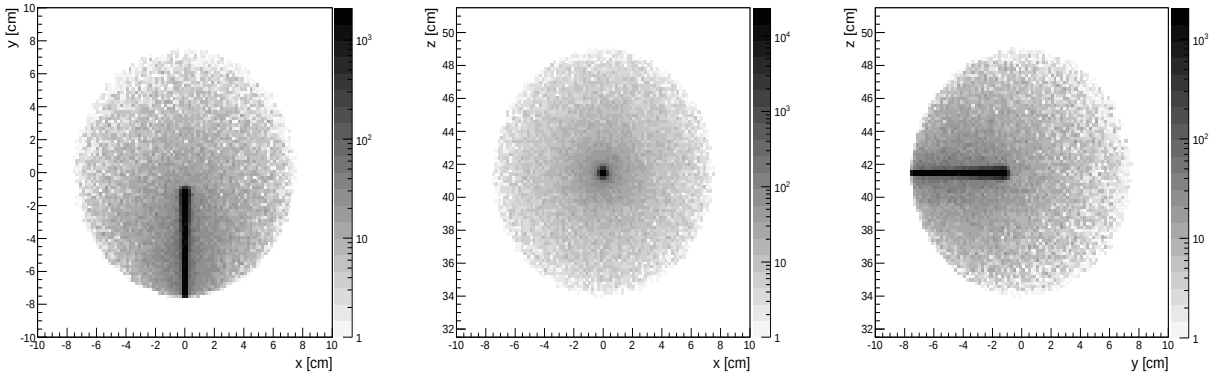

(a) (b) (c)

Figure 4.12: Simulated 2D images of (a) xy-projection, (b) xz-projection, (c) yz-projection of the emission location of gamma rays leaving the PMMA phantom during irradiation by the proton beam at 100 MeV.

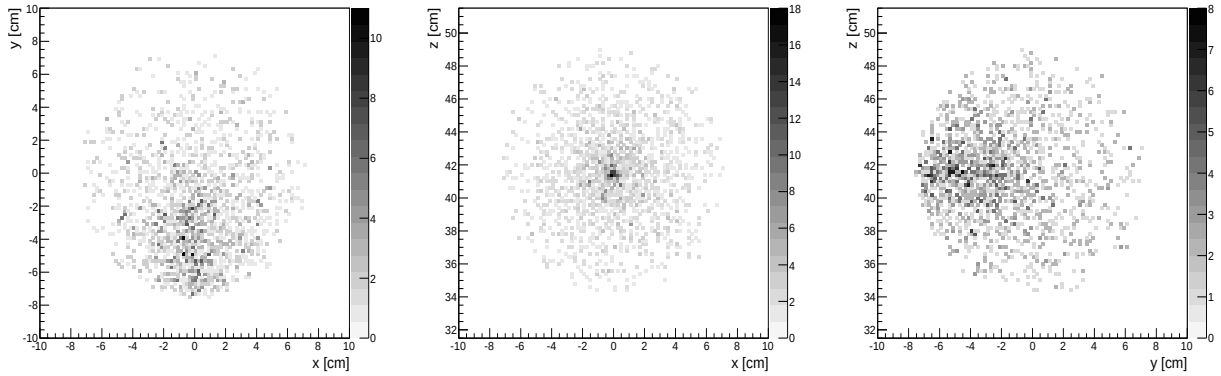

(a) (b) (c)

Figure 4.13: Simulated 2D images of (a) xy-projection, (b) xz-projection, (c) yz-projection of the emission location of gamma rays at 511 KeV energy, leaving the PMMA phantom during irradiation by the proton beam at 100 MeV.

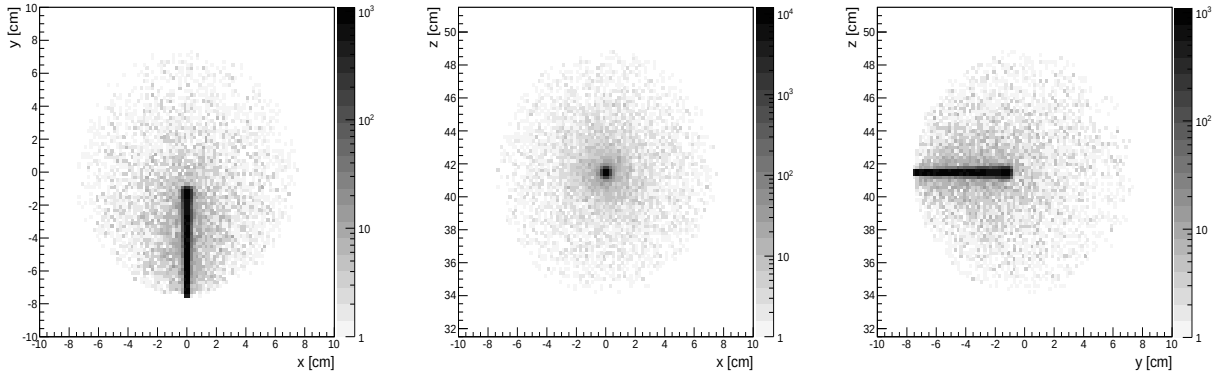

(a) (b) (c)

Figure 4.14: Simulated 2D images of (a) xy-projection, (b) xz-projection, (c) yz-projection of the emission location of gamma rays at energy interval [2 MeV, 8 MeV], leaving the PMMA phantom during irradiation by the proton beam at 100 MeV.

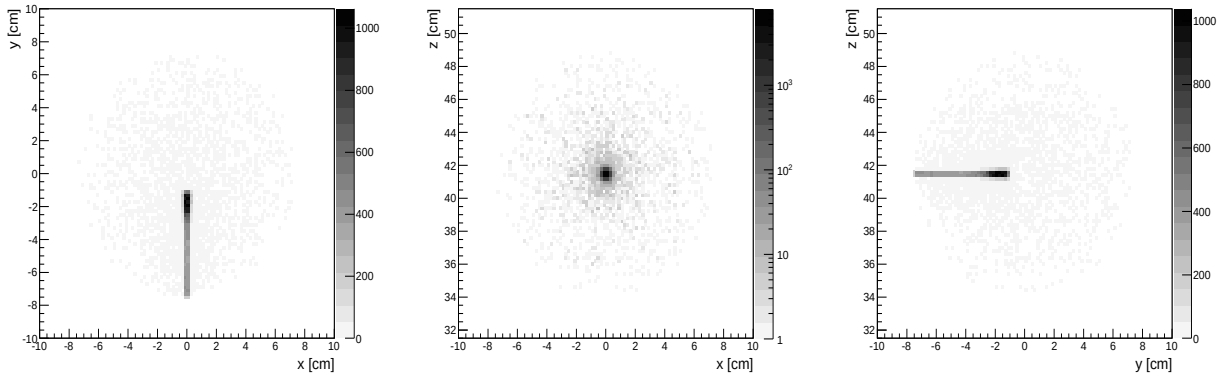

(a) (b) (c)

Figure 4.15: Simulated 2D images of (a) xy-projection, (b) xz-projection, (c) yz-projection of the emission location of gamma rays at energy interval [8 MeV, 30 MeV], leaving the PMMA phantom during irradiation by the proton beam at 100 MeV.

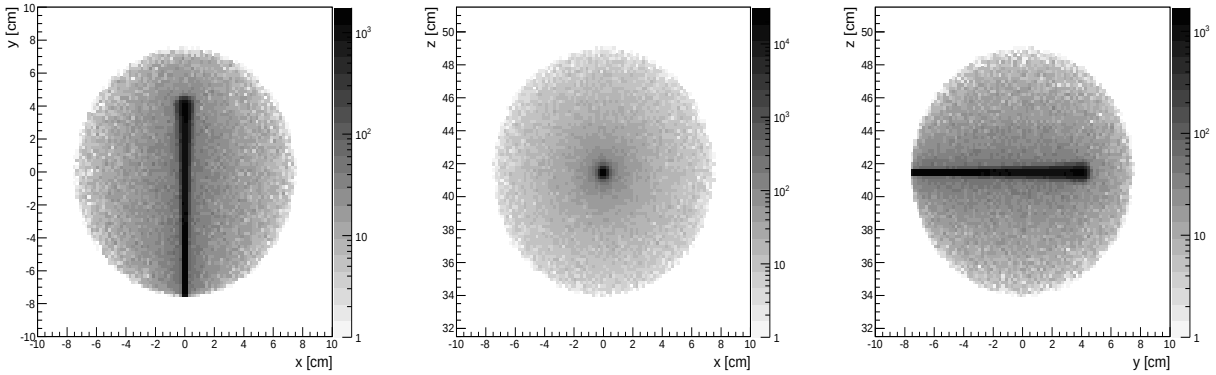

(a) (b) (c)

Figure 4.16: Simulated 2D images of (a) xy-projection, (b) xz-projection, (c) yz-projection of the emission location of gamma rays leaving the PMMA phantom during irradiation by the proton beam at 140 MeV.

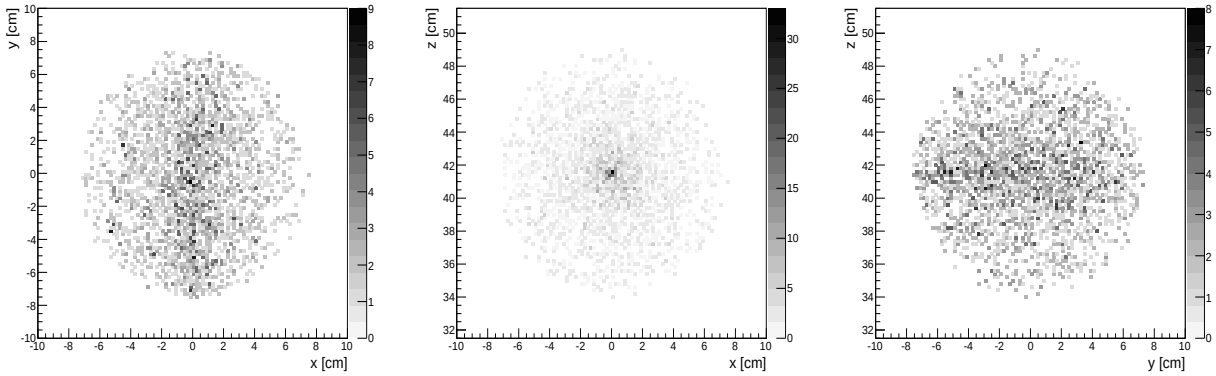

(a) (b) (c)

Figure 4.17: Simulated 2D images of (a) xy-projection, (b) xz-projection, (c) yz-projection of the emission location of gamma rays at 511 KeV energy, leaving the PMMA phantom during irradiation by the proton beam at 140 MeV.

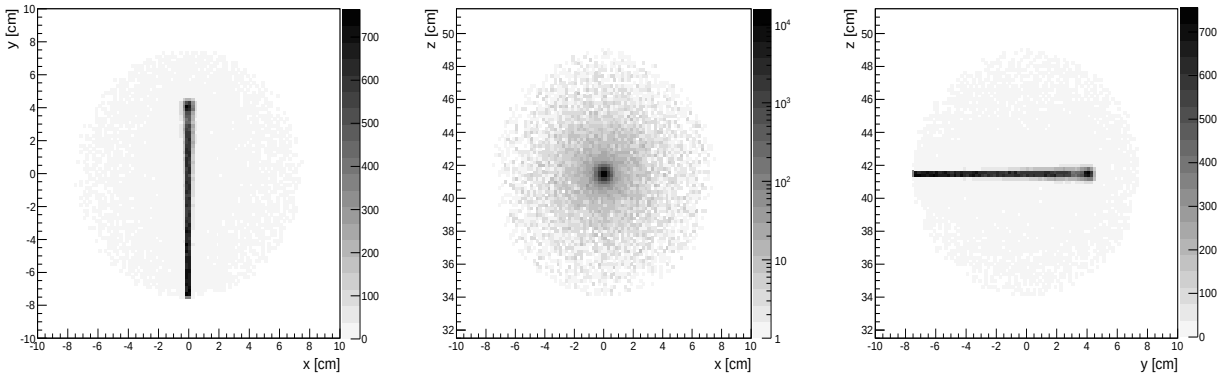

(a) (b) (c)

Figure 4.18: Simulated 2D images of (a) xy-projection, (b) xz-projection, (c) yz-projection of the emission location of gamma rays at energy interval [2 MeV, 8 MeV], leaving the PMMA phantom during irradiation by the proton beam at 140 MeV.

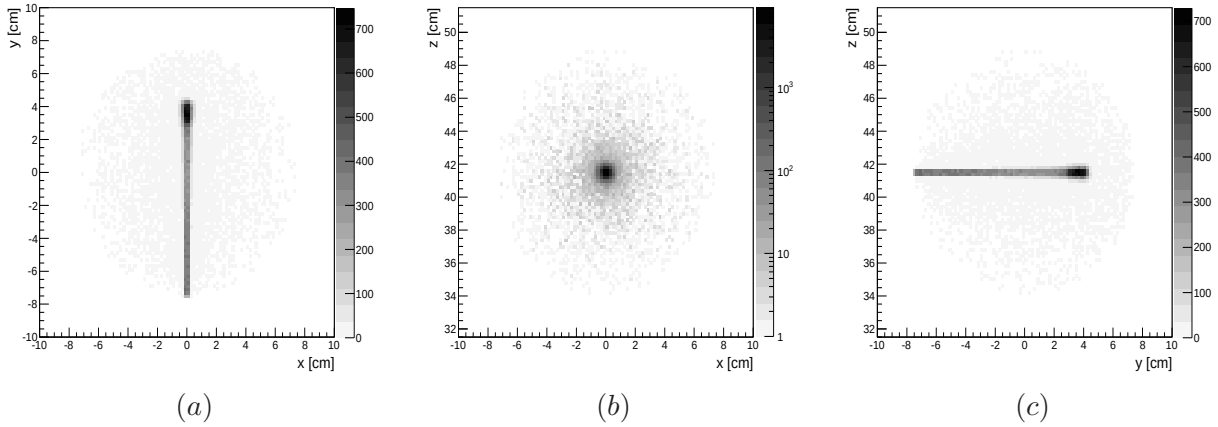

Figure 4.19: Simulated 2D images of (a) xy-projection, (b) xz-projection, (c) yz-projection of the emission location of gamma rays at energy interval [8 MeV, 30 MeV], leaving the PMMA phantom during irradiation by the proton beam at 140 MeV.

4.3 Quality assurance of hadron therapy

4.3.1 The proposed Compton imaging technique

The Compton scattering effect is the dominant interaction process of medium-energy gamma rays, i.e., with an energy range from a few hundred keV up to 10 MeV, depending on the scatter material. A way to reconstruct the origin of Compton scattered gamma rays is to record the directions of the secondary/scattered particles, i.e., measure the direction and energy of the scattered gamma ray as well as the direction and energy of the recoiled electron. Compton based techniques of energetic gamma-ray measurement, mainly developed for medium-energy astrophysics, vary according to the capability of measuring the Compton recoiled electron. One of the standard Compton camera designs consists of a low-Z scatter material, where the first Compton interaction takes place, and a high-Z material, where the scattered gamma-ray is absorbed. If the two detectors are well separated (as it was the case for COMPTEL [Schönfelder et al., 1993a]), then time-of-flight measurements are possible. However, here it is considered a more compact design of the scatterer, which does not allow time-of-flight measurements, but has the capability to measure the recoil electrons.

The proposed Compton based imaging technique enables the measurement of the recoiled electron

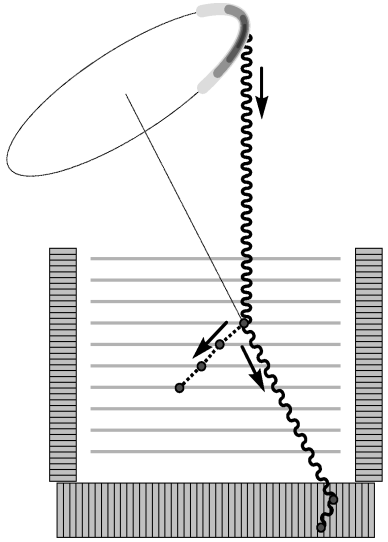

Figure 4.20: Compton imaging technique based on gamma-ray and electron tracking. Illustration of the basic detection sub-systems: a central tracker (the scattering sub-system) is surrounded by a calorimeter (the absorption sub-system). Both sub-systems are working in coincidence, i.e., a detectable gamma ray has to undergo at least one interaction in the tracker, and at least one interaction in the calorimeter. The tracker consists of several layers, thin enough to track the recoil electron. The scattered photon is stopped in the second subsystem.

direction (Figure 4.20). As a result, the gamma-ray origin can be narrowed down much more, namely the Compton cone is reduced to a cone segment of a length which depends on the measurement accuracy of the recoiled electron [Zoglauer, 2005].

The proposed Compton imaging technique records individual events by considering the kinematics and topology of the Compton interactions. Inherently, all the individual measurements are affected by errors which propagate into the recovery process of the source origin and direction. Moreover, the complex geometry of detectors illustrating the imaging technique requires a high precision of energy and position information. However, a definitive limit for the angular resolution possible to attain is represented by the impossibility to determine the initial (pre-scattering) momentum of the recoiled electron, i.e., Doppler broadening.

The efficiency of a detector utilizing the proposed Compton based imaging technique is determined by both detector technologies, and the performance of the algorithms which have to recover what happened into the detector, i.e., the event reconstruction algorithm, and the algorithm which has to reconstruct the sources , i.e., the image reconstruction algorithm. The goal of event reconstruction is to correctly order the individual hits in the detector, and then to identify the interactions, e.g., multiple Compton scatterings, pair creation, along with their parameters, e.g., energy deposits, interaction position. The most challenging step of data analysis is image reconstruction, which has to recover the origin of the sources. Each lost, unassigned, or incompletely reconstructed event lowers the efficiency and increases the background. Hence the capability of the algorithms to accurately perform the data analysis has a high influence on the overall performance of the detector. Data analysis steps performed in case of the proposed detector based on the described Compton imaging technique are presented in Section 4.3.4.

4.3.2 Preliminary study

A preliminary study was done by analyzing the response of the simulated version of the MEGA prototype in the presence of various gamma-rays and neutron sources. The measurement principle of the prototype is based on the technique described in Section 4.3.1, additionally enabling detection of pair creation events. Details about the MEGA prototype can be found in [Andritschke, 2006].

First, five gamma-ray point sources at different energies were placed at an on-axis position at 8 cm above the front side of the imaging detector. The intensity was set to 10^5 photons/second. The energy of the sources was successively 1 MeV, 3 MeV, 8 MeV, 10 MeV, and 20 MeV, respectively. Figure 4.21 shows the reconstructed images of the first source. The total number of Compton backprojected events is 3×10^4. Figure 4.22 shows the reconstructed images of the second gamma-ray point source at 3 MeV. The number of backprojected events is 4×10^4. Figure 4.23 shows reconstructed images of the 8 MeV point source. The number of backprojected events is 5×10^4 Compton scattering still represents the dominant interaction process, while the pair creation events represent about 8.6% of the total recorded events. The image of 10 MeV point source was reconstructed using 49×10^3 backprojected events, respectively (Figures 4.24).

When considering the 1 MeV gamma-ray source, the Compton scattering effect is dominant; in contrast, for the 20 MeV sources, the pair creation events result in a higher influence. In case of the 3 MeV point source, the number of pair events used for image reconstruction is 10^3, for the 8 MeV source is 5×10^3, while for the 10 MeV, and 20 MeV point sources, is 5×10^3, and 10^4, respectively. Figure 4.25 shows the reconstructed images of the 3 MeV and 20 MeV point sources using the pair creation events after 19 iterations of the imaging algorithm. At 3 MeV, mostly wrongly identified Compton events are reconstructed, where just one track is present, and the electron genertates a different signature.

A strong correlation between the detector geometry, technologies performance and the quality of the reconstructed image exists. Errors in events detection reduce the accuracy of sources localization (see Section 4.3.7). The angular resolution depends on Doppler broadening and both energy and spatial resolution of the detector. In case of the prototype, the angular resolution is limited to 10°, depending

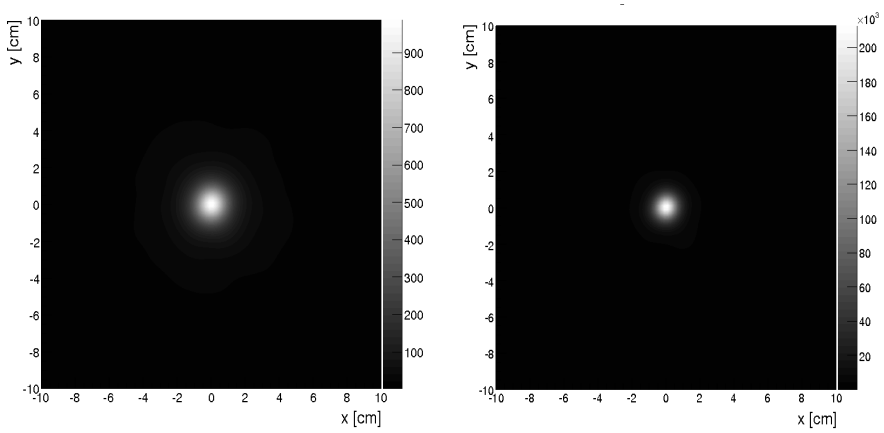

(a) (b)

Figure 4.21: Reconstructed images of the 1 MeV point source after (a) 7 iterations, and (b) 19 iterations.

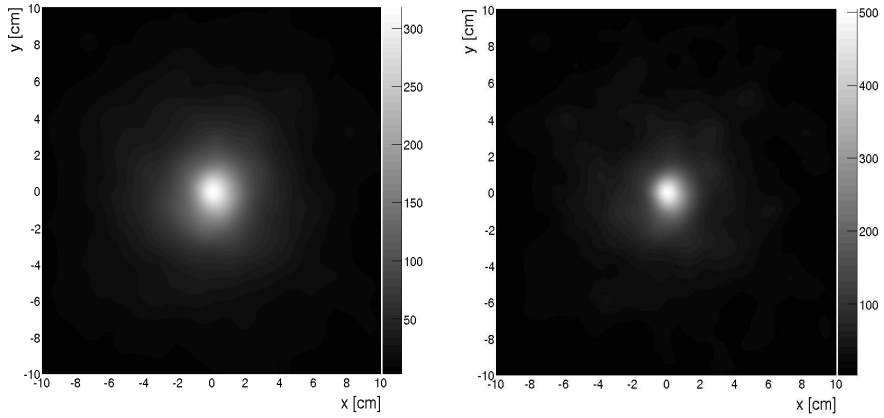

(a) (b)

Figure 4.22: Reconstructed images of the 3 MeV point source after (a) 7 iterations, and (b) 19 iterations.

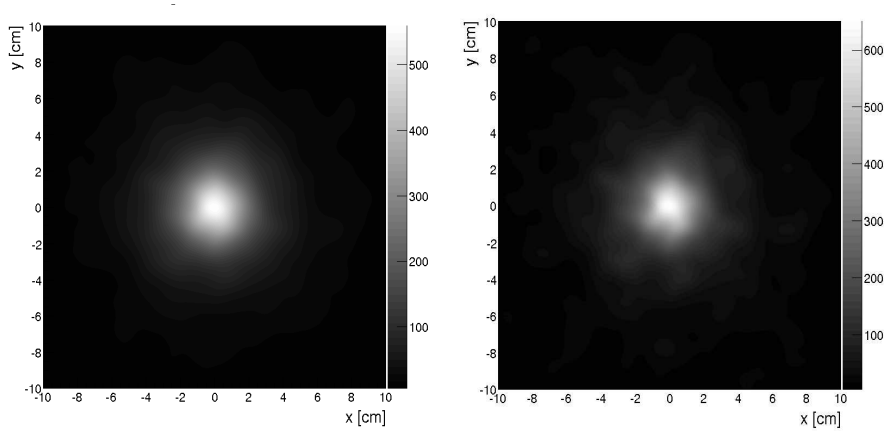

(a) (b)

Figure 4.23: Reconstructed images of a 8 MeV point source after (a) 7 iterations, and (b) 19 iterations.

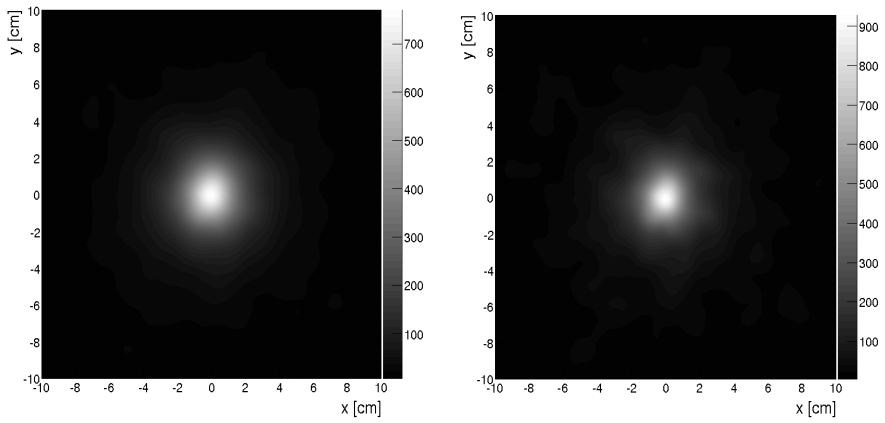

(a) (b)

Figure 4.24: Reconstructed images of a 10 MeV point source after (a) 7 iterations, and (b) 19 iterations.

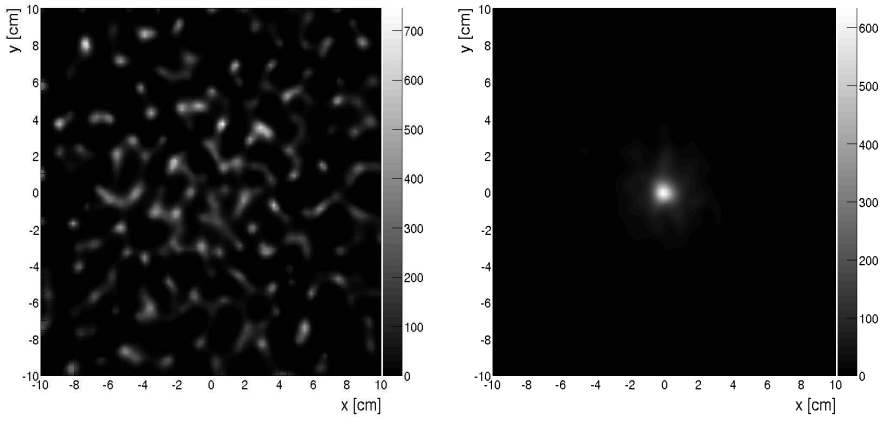

(a) (b)

Figure 4.25: Reconstructed images using pair creation events of the (a) 3 MeV, and (b) 20 MeV point sources after 19 iterations.

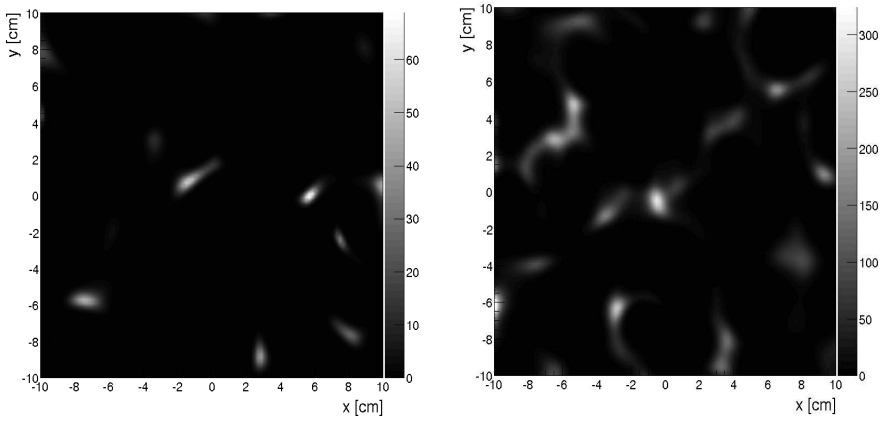

(a) (b)

Figure 4.26: Reconstructed images of the 3 MeV neutron point source after 19 iterations (a) without electron tracking, and (b) with electron tracking.

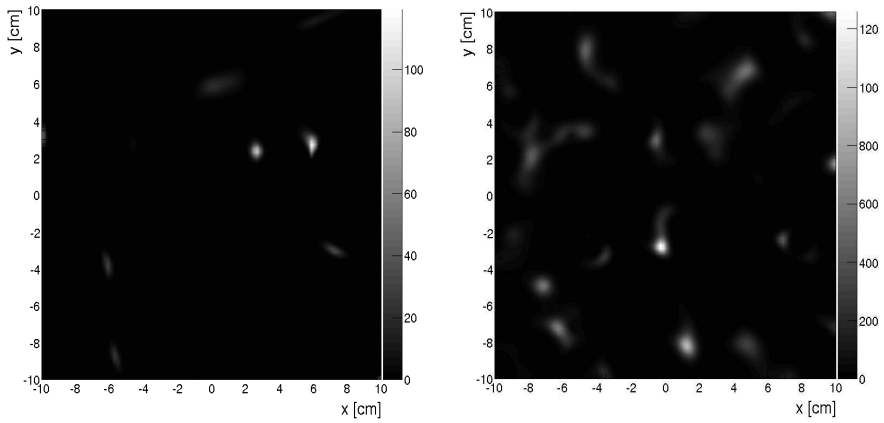

(a) (b)

Figure 4.27: Reconstructed images of the 20 MeV neutron point source after 19 iterations (a) without electron tracking, and (b) with electron tracking.

on considered energy. In addition, the spatial resolution of the reconstructed images is influenced by the imaging algorithm. Details about the reconstruction algorithm can be found in Section 5.1.

Five neutron sources at different energies, e.g., 1 MeV, 3 MeV, 8 MeV, 10 MeV, and 20 MeV, were placed at 8 cm above the front side of the imaging detector. The number of triggered events was 10^3, for each energy. The detection efficiency is about 50% for all the sources. Figures 4.26, and 4.27 show the Compton images reconstructed with and without considering the tracking of the recoiled electron. The number of backprojected events with electron tracking represents about one third of all reconstructed events.

The limited resolution of the prototype motivates the optimization of the imaging detector geometry, which should enable improved position and energy resolution, and consequently, improved angular resolution.

4.3.3 The proposed imaging detector

The geometry of the proposed gamma-ray detector HTI (Hadron Therapy Imaging) is based on the imaging technique described in Section 4.3.1. It consists of two detector sub-systems (see Figure 4.28).

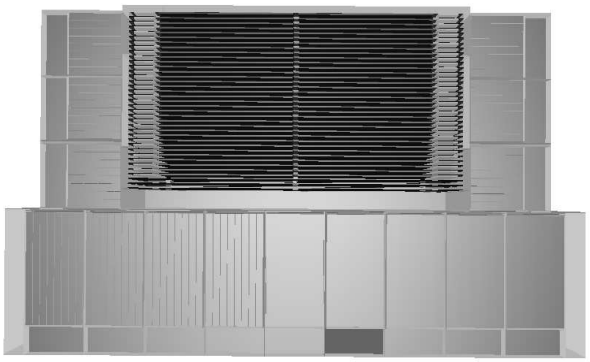

Figure 4.28: Illustration of the simulated version of the HTI system. The tracker is surrounded by the calorimeter made of $LaBr_3$ bars (surface area: 5×5 mm, length: 8 cm bottom, 4 cm side). The tracker consists of 36 layers of double-sided Silicon-strip detectors. Each layer is made of 2 by 2 wafers, which have a length of 10 cm, thickness of 0.5 mm and a strip pitch of 0.5 mm.

In the tracker, which is composed of several layers made of thin silicon wafers, the initial interaction happens (either Compton scattering or pair creation), and the electrons and positrons are tracked. A

calorimeter surrounds the lower hemisphere of the tracker and stops all secondary particles. It measures energy and interaction positions.

The simulation model of the tracker comprises 36 layers of double-sided Silicon-strip detectors. Each layer consists of 2 by 2 wafers, which have a length of 10 cm, thickness of 0.5 mm and a strip pitch of 0.5 mm. Strips on one side of the wafer determine the x-position of an interaction, orthogonal strips on the other side of the wafer determine the corresponding y-position. The layers are spaced 0.35 cm from each other. A uniform 1-sigma energy resolution of 1 keV and a 10 keV threshold were assumed in the electron tracker. The calorimeter consists of $LaBr_3$ bars (surface area: 5×5 mm, length: 8 cm bottom, 4 cm side). An energy resolution of 4.3% FWHM at 662 keV, and a threshold of 28 keV was assumed. For an event to be triggered at least one hit in the tracker and one hit in the calorimeter is required.

In the tracker, gamma rays undergo either Compton scattering or pair creation. If the energy of the produced electrons (and positrons) is above $\sim$500 keV then they pass through several layers and the direction of the recoil electron or electron-positron-pair can be determined during data analysis.

4.3.4 Data analysis tools

Simulations of the HTI system have been performed using the same tool as the simulations of the gamma-ray emission patterns, Cosima, a Monte-Carlo simulation tool based on Geant4, which is part of the MEGAlib package [Zoglauer et al., 2006].

For Compton telescopes, the first step of data analysis is the event reconstruction. The simulation (like real measurements) results in a set of positions and energies. To determine the origin of the gamma rays, the interaction sequence has to be determined by analyzing all possible paths of the gamma ray in the tracker and the calorimeter as well as of all secondaries in the tracker. For this step three different approaches are available, the classic approach named 'Compton sequence reconstruction' [Zoglauer, 2005], a Bayesian approach [Zoglauer et al., 2007], and a neural network approach [Zoglauer and Boggs, 2007]. Due to the large amount of generated simulation data, and the limited amount of available computing resources, the fastest approach, the classic approach has been chosen for the event reconstruction. Since the HTI allows for gamma ray as well as electron tracking, sufficient redundant measurements about the event is recorded to enable background rejection reliably. For the hadron-therapy application, the most important background sources are random coincidences, other particles originating from the phantom (e.g. neutrons), and incompletely absorbed events.

The next and most challenging step during data analysis is image reconstruction. The knowledge of the first and second interaction position of the gamma ray along with the measured energies allows restricting the origin of the gamma ray to a surface of a cone. Its opening angle can be calculated via the standard Compton equation. Moreover, if an electron track is present, reconstructing the direction of the recoil electron enables to restrict the incident gamma-ray direction further to a small segment of the cone. The applied list-mode maximum-likelihood expectation-maximization image reconstruction algorithm (LM-MLEM) is an event-by-event approach, which avoids large data-space matrices. This imaging algorithm was developed based on the two-dimensional near-field imaging algorithm proposed by [Wilderman et al., 1998a] for medical imaging, being extended to also include tracked Compton events. Details about the algorithm are included in Section 5.1.

The system response matrix is computed similar to [Wilderman et al., 2001]. Each event response is determined from the calculated emission and interaction probabilities, which are described by the Compton cones and arcs profiles. The profiles represent the distributions of possible true event cones for the measured one, and the distribution of possible true scatter planes for the measured scatter plane. The simplest form to determine the shape of the profile, which is currently used, is by an 1D Gaussian approximation of the widths corresponding to the values derived from the ARM and the SPD. The ARM is a distribution given by the smallest distance of the known origin of the gamma ray to the Compton cone. The SPD is defined as the angular distance on the Compton cone between the known origin of the

photons and the calculated one. It is a measure of the length for the Compton scatter arc, while the ARM is a measure for the width of the Compton scatter cone or arc (see Section 2.2.2).

4.3.5 Simulated performance

Determining the origin of a gamma ray with a Compton camera utilizes energy and position measurements. Therefore the accuracy of the reconstruction is limited by the uncertainties associated to those measurements. In addition, the angular resolution of Compton telescopes is limited by Doppler-broadening resulting from the unknown momentum of the electron bound to its nucleus. Finally the efficiency of the telescope is limited by the amount of available Silicon layers, the number of completely absorbed events, and the detection thresholds.

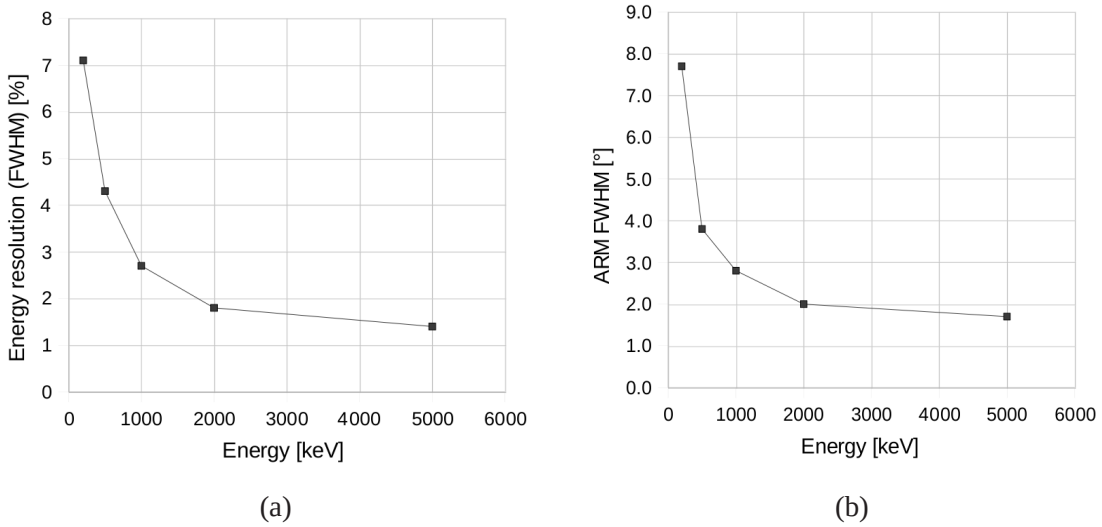

(a) (b)

Figure 4.29: (a) Energy resolution of the HTI simulation model. (b) Angular resolution of the HTI simulation model as FWHM of the ARM.

The final energy resolution is defined by the energy resolution in the tracker and in the calorimeter. It improves with increasing energy of the initial gamma ray (Figure 4.29 (a)).

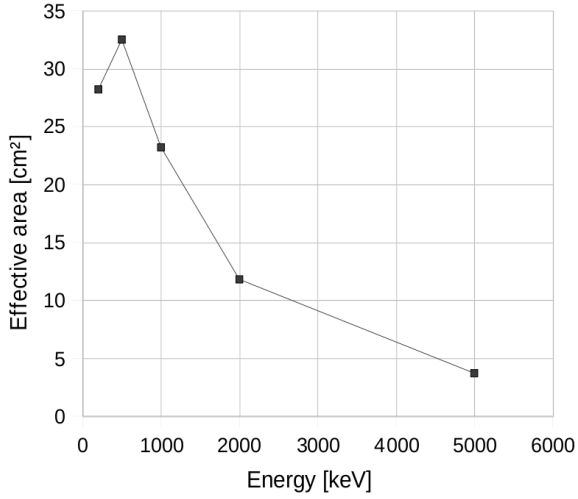

Figure 4.30: On-axis photo-peak effective area of the HTI simulation model after event with no energy cut selection.

The angular resolution of a telescope can be defined by the FWHM of the ARM of the telescope. The FWHM of the ARM of the HTI simulation model is, at lowest energies, limited by Doppler-broadening,

at medium energies by energy and position resolution and at higher energy by position resolution alone (Figure 4.29 (b)).

The on-axis effective area is defined as the efficiency in producing a detected event for each incident gamma-ray photon. The on-axis photo-peak effective area of the HTI simulation model can be found in Figure 4.30. The peak is situated around a few hundred keV. At low energies, the probability for a coincidence in tracker and calorimeter decreases due to a small cross-section for Compton scattering. At high energies the probability for a completely absorbed event decreases due to escapes and due to more interaction sites in the tracker, which generally increases the risk of interactions in passive material.

4.3.6 Reconstructed images

In order to estimate the imaging performance of the detector, a PMMA sphere (radius 7.5 cm) was placed at 8 cm distance from the imaging system (Figure 4.31). The phantom was irradiated by a proton beam with different energies selected from the expected treatment range, 70 MeV, 100 MeV and 140 MeV and an intensity fixed at 10^6 protons/s. The total simulation time is 20 seconds.

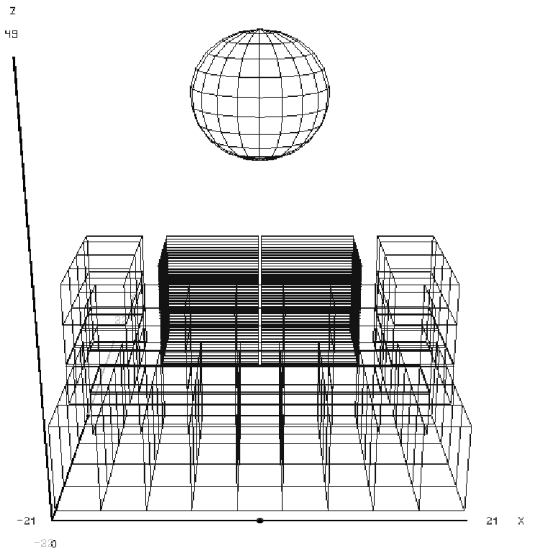

Figure 4.31: Wire-frame representation of geometry setup as used for hadron therapy simulations. A cut-view by a back-side plane was used.

The simulated data was reconstructed as described in Section 4.3.4.

Figure 4.32 shows reconstructed 2D images, where the reconstruction plane is the beam plane (at z = 41.5 cm) for the three different beam energies. Only Compton events with energies above 450 keV were reconstructed. As expected, elevating the proton beam energy from 70 MeV to 140 MeV results in increasingly long, line-shaped reconstructed beams path.

The intensity profiles of the reconstructed images along the central vertical line are illustrated in Figure 4.33. For the proton beam at 70 MeV, the falloff region of the deposed dose is after 3.5 cm from the entry point into the phantom (at -7.5 cm on the y-axis). When increasing the beam energy to 100 MeV and 140 MeV, the Bragg peak is translated to 6.5 cm and 12 cm, respectively (Figure 4.33, dashed lines).

The length of the reconstructed gamma-ray source depends on the beam energy being related to the proton range in the phantom. The decay of the reconstructed gamma ray activity allows retrieving information about the location of the Bragg peak. However, assuming ideal events, i.e., no measurement uncertainties (energy, position), and no escaping events or deposits in passive material, the intensity profile of Compton reconstructed image obtained at 140 MeV shows a roughly abrupt decay at the Bragg peak position (Figure 4.33, solid line). The ideal Compton reconstructed images of measured gamma

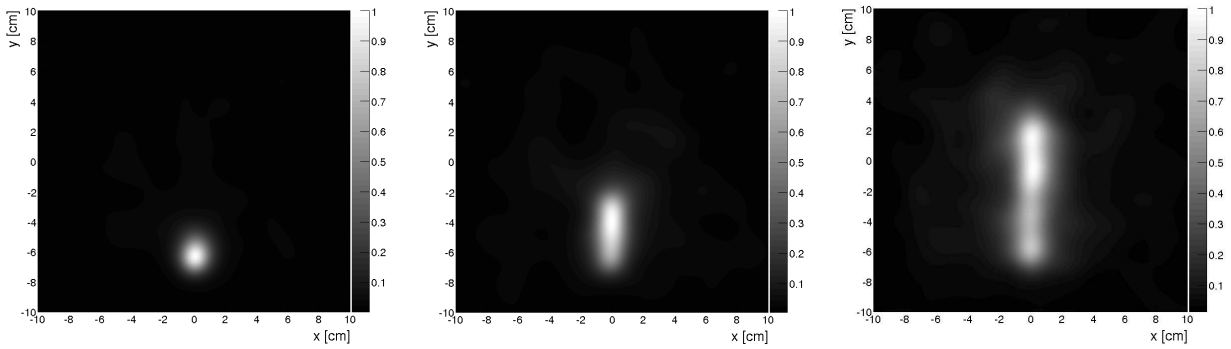

(a) (b) (c)

Figure 4.32: Compton reconstructed images of measured gamma rays during simulated irradiation of PMMA phantom by a proton beam at (a) 70 MeV, (b) 100 MeV, and (c) 140 MeV. The reconstruction plane is the beam plane.

rays during irradiation are illustrated in Figure 4.34. The corresponding profiles are presented in Figure 4.35.

With the current imaging algorithm the Bragg peak cannot be recovered precisely. This fact is expected since the reconstruction algorithm estimates the source distribution by a ML function using a crude approximation for the model of data acquisition process. The application of ML estimation based algorithms in reconstruction of radioactive sources in PET reported the existence of both noise and edge artifacts [Snyder et al., 1987]. Secondly, the detector response is not adapted for events with high-incident energy. In addition, the algorithm does not include corrections for absorptions in the phantom, and does not include the prior knowledge that the source is line shaped. A more detailed discussion about the reconstruction process is presented in the next section.

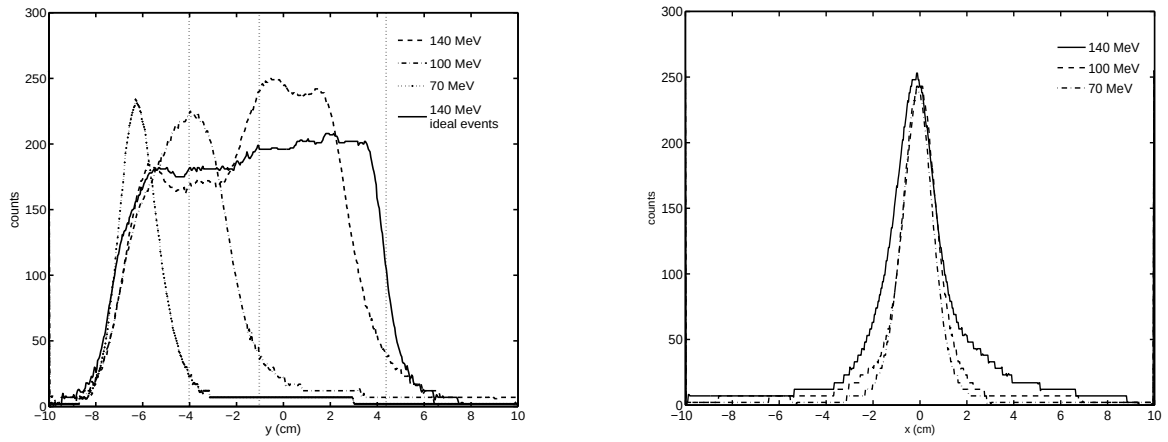

(a) (b)

Figure 4.33: (a) Vertical intensity profiles of the Compton reconstructed images assuming ideal events (solid line), and assuming measurement uncertainties (discontinuous lines). Bragg peak positions of proton beams at 70 MeV, 100 MeV and 140 MeV are indicated by dotted vertical lines. (b) Horizontal intensity profiles of the Compton reconstructed images assuming measurement uncertainties.

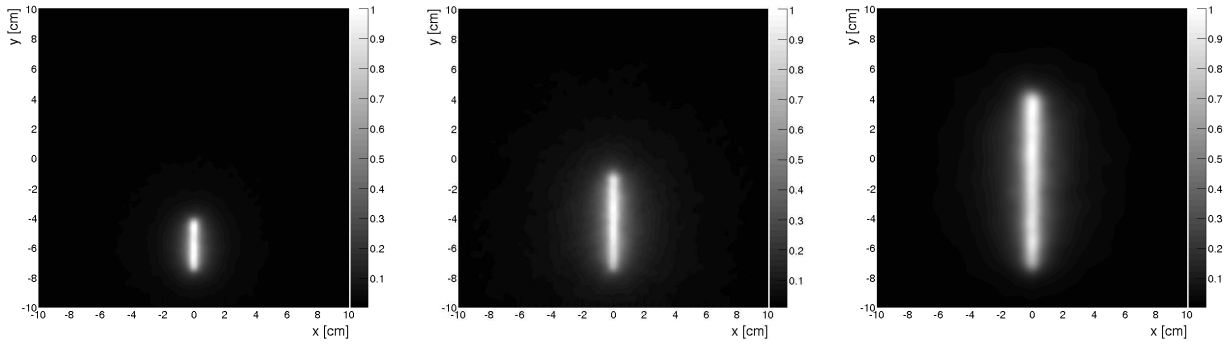

(a) (b) (c)

Figure 4.34: Ideal Compton reconstructed images of measured gamma rays during simulated irradiation of PMMA phantom by a proton beam at (a) 70 MeV, (b) 100 MeV, and (c) 140 MeV. The reconstruction plane is the beam plane.

4.3.7 Discussion

In this section, the capability of the proposed imaging system using the LM-MLEM algorithm is studied. To achieve the reconstruction precision required by our application, an accurate modeling of the detection system is necessary in order to correctly calculate the detection sensitivity and the response of individual events, which determine the estimated quality of the image reconstruction.

In the present algorithm, the response of each event is approximated via transition probabilities represented by the Compton cones and arcs profiles. For Compton events, where the energy transferred to the recoil electron is not sufficient to produce a track, i.e., incident gamma rays with energies below 2 MeV, the width and the shift of the cone is mainly determined by the energy and position measurement. With increasing energy, the events have an electron track and the origin is restricted to an arc of the cone-section whose length is determined by Molière Scattering, but the profile becomes broader due to energy leakage. Also, using a list-mode algorithm, a difficult problem to resolve is the absolute normalization, i.e., reconstructing intensity/flux during the image reconstruction process. Since a correct normalization for each event is extremely time consuming, this operation has not been done for the presented images

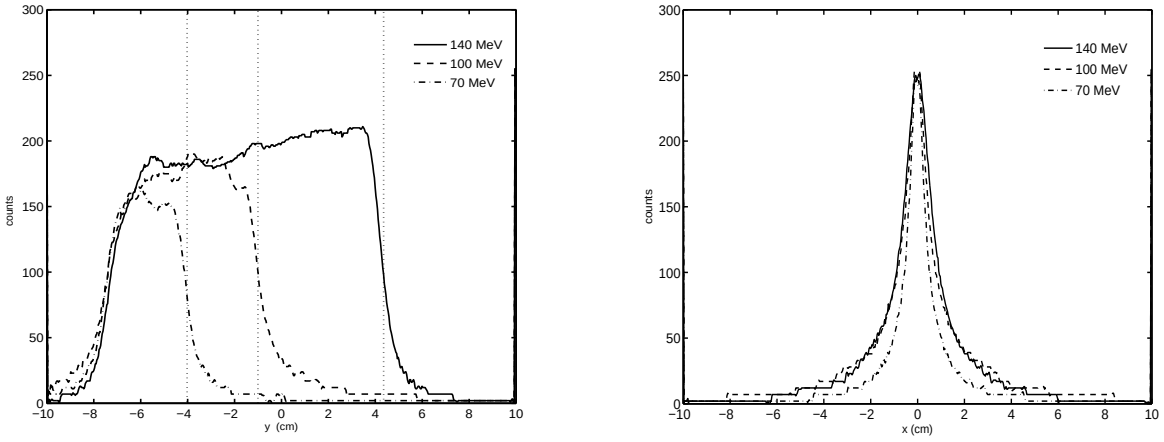

(a) (b)

Figure 4.35: (a) Vertical intensity profiles of the Compton reconstructed images (Figure 4.34) assuming ideal events. Bragg peak positions of proton beams at 70 MeV, 100 MeV and 140 MeV are indicated by dotted vertical lines. (b) Horizontal intensity profiles of the Compton reconstructed images assuming ideal events.

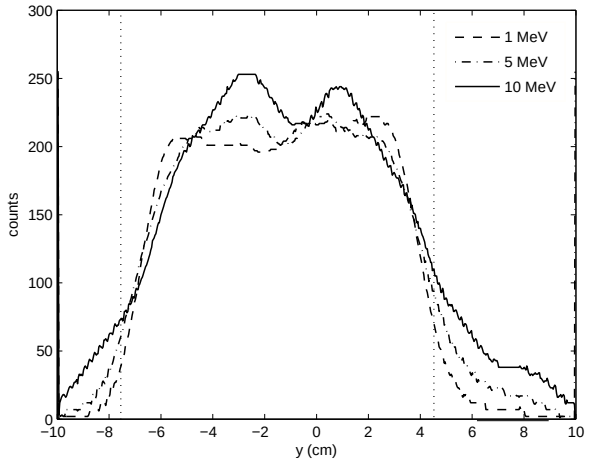

Figure 4.36: Intensity profiles of the Compton reconstructed images of gamma-ray line sources. The edge of line sources are represented by dotted vertical lines.

and the sensitivity coefficient is assumed to be one.

In order to evaluate the reconstruction performance, a gamma-ray line source was placed in the PMMA phantom at the same distance from the detector as the proton beam. The length of the sources is equal the 140 MeV proton beam path in the phantom, i.e., 12 cm. A mono-energetic spectrum was assumed for all sources. The number of reconstructed events is the same as for the images of emitted gamma rays activity during the 140 MeV proton beam irradiation. An equivalent response of the imaging algorithm can be observed, i.e., the edge artifact is present in all reconstructed images being more pronounced by increasing the source energy (Figure 4.36). This is due to usual artifacts generated by the reconstruction algorithm, the modelling of the system response, and the low number of photons. Moreover, the imaging algorithm does not take into account the different absorption probabilities which the photons encounter when they are emitted at different depths in the phantom, i.e., it is less likely to measure a photon from the center of the phantom than from the edge of the phantom.

The present imaging algorithm includes the ordered-subsets acceleration technique. One iteration took 2 seconds on an Intel® Core™2 Duo CPU, T7700 @2.40GHz, and 2 GB of RAM, while the initial back-projection consumed nearly 120 seconds. However, more sophisticated acceleration techniques could be envisioned, e.g., space-alternating generalized EM, strategies of row-action mode with dynamic relaxation, etc. Acceleration could also be achieved by using an architecture exploiting parallel processing of data (e.g., using multiple cores or the GPU). The latter method will allow storing a greater number of Compton events, and an extension into 3D of the algorithm.

4.4 Conclusion

Gamma rays in the Compton scattering energy regime are predominantly emitted during proton beam irradiation of a PMMA phantom. Thus they are the primary target for an on-line monitoring system, which measures the dose deposition and the Bragg peak location during hadron therapy.

Simulations revealed that using a tracking Compton camera to detect gamma rays emitted during irradiation of a PMMA phantom by a typical hadron therapy beam, allows to recover the beam path within the phantom. The obtained intensity profiles show a correlation between the decay of the gamma rays spatial distribution and the Bragg peak. However, further improvements of the image reconstruction algorithm are necessary to clearly extract the Bragg peak position with millimeters precision from the reconstructed images.

Chapter 5

List-mode wavelet based algorithm for Compton imaging

List-mode data acquisition was firstly introduced for Compton imaging by [Wilderman et al., 1998b], resulting in a significant computation advantage over approaches using binned-data. This data acquisition mode requires to store the essential parameters of the Compton events, e.g., Compton scatter angle, total energy, interaction positions, into a list. Therefore a full precision of measured Compton events is assured. The classical MLEM algorithm including list-mode data acquisition is described in Section 5.1. A novel approach of its regularization based on wavelet thresholding is presented in Section 5.2.3. The algorithm was evaluated using simulated data generated by a Compton camera [Frandes et al., 2010a].

Generally, the primary factors limiting the quality of the reconstructed images are e.g., the detector resolution and photon density. To overcome the finite detector resolution, i.e., the inherent measurement uncertainties due to energy, and position resolution, geometry of the detector, it is necessary to accurately model the photon detection process, i.e., the imaging detector response.

The detection process of a Compton based imaging system has to analyze all the probabilities of interactions encountered by photons in order to retrieve their origin direction. This analysis results in a high dimensional calculation which demands large computation resources. Generally, the system resolution is scarified to reduce the noise in the reconstructed images. An optimal trade-off between resolution and noise propagation requires to also accurately model the noise distribution in the data. The model of both detector response and noise distribution are determined by the adopted reconstruction methods. Therefore the methods chosen for reconstruction represent a significant aspect in the overall performance of the imaging detector.

In the following, the statistical model associated to Compton data acquisition process is presented.

The Statistical Detection Model

Let J be the pixelated image space domain, each pixel presenting an intensity (mean) $f_j = (f)_j$, $j = \overline{1, M}$, and x_j the photon count with the Poisson distribution

$$p(x_j) = e^{-f_j} \frac{f_j^{x_j}}{x_j!} \tag{5.1}$$

Let D be the data space domain, and $y = (y_i)_{i=\overline{1,N}}$ a set of measured events. The probability of detecting an emission from the source pixel j with the attributes (y_i) is t_{ij}, which denotes an element of the system response matrix T. Therefore the intensity of expected events is defined by

$$g(y_i|f) = \sum_j t_{ij} f_j \tag{5.2}$$

The sensitivity, i.e., the probability of an emission from f_j to be detected with any attributes $y_i \in y$ is $s_j = \sum_i t_{ij}$. The total mean number of counts is $c = \sum_j^M s_j f_j$.

The likelihood function of y given f is defined as

$$l(y|f) = p(N|f) \prod_{i=1}^{N} p(y_i|f) \tag{5.3}$$

where $p(N|f) = \frac{c^N}{N!} e^{-c}$ is the probability of detecting N events following a Poisson distribution.

The disctretized forward problem of the Compton imaging process may be illustrated as following

$$y = Tf + n \tag{5.4}$$

The vector n denotes the noise arising from the measurement, or acquisition process of Compton data. Generally, the errors in Compton cameras are approximated as following normal distributions [Wilderman et al., 2001]. Therefore the noise is estimated by a general normal distribution, $n \sim N(\mu, \sigma^2)$.

To calculate f knowing both y and T is an ill-posed inverse problem, intensively studied in the last decades. Several attempts have formulated an inversion formula in specific conditions of Compton data acquisition using, e.g., analytical approaches (e.g., [Cree and Bones, 1994], [Basko et al., 1999], [Parra, 2000], [Tomitani and Hirasawa, 2002], [Maxim et al., 2009]), or iterative reconstruction methods (e.g., [Singh and Doria, 1983b], [Brechner et al., 1987], [Brechner and Singh, 1990], [Sauve et al., 1993]). A classical reconstruction method maximizes the likelihood function of estimated solution by the iterative EM algorithm. The iterative formula of the MLEM algorithm [Shepp and Vardi, 1982] with list-mode data acquisition, and acceleration by the ordered-subsets method included has the following form

$$f_j^{(k,l+1)} = \frac{f_j^{(k,l)}}{s_j} \sum_{i \in S_l} \frac{t_{ij}}{\sum_{b=1}^{M} t_{ib} f_b^{(k,l)}} \tag{5.5}$$

where S_l represents the considered lth subset of events.

Considering a unique set of events, the iterative formula describes the classical MLEM algorithm. The sensitivity factor $s_j = \sum_{i=1}^{N} t_{ij}$ represents the addition of response elements over all the possible measurements. The list-mode MLEM algorithm is detailed in Section 5.1.

ML criterion provides image estimation from Poisson data, which are corrupted by noise. Generally, estimation by unconstrained or constrained ML criterion yields noise amplification during the iterative process, which arbitrarily causes large changes of solutions when only a slight change of data is produced. A remedy is to stop the iterations before artifacts appear. However, this solution is challenging.

Possible solutions could be derived by integration of various penalization and regularization strategies. A regularization method was proposed by [Knödlseder et al., 1999] in context of COMPTEL [Schönfelder et al., 1993b] data reconstruction. Considering a Bayesian framework, [Lee et al., 2008] investigated the application of maximum a posterior approach in case of Compton scattered data. The iterative algorithms are firstly, a row-action method and secondly, a block-sequential method, which is a relaxed version of the OSEM method. The regularization is done by using a convex non-quadratic smoothing prior. The prior information reflects assumptions about the spatial distribution of the source. Both algorithms are applied in their binned-data version.

After introducing the classical MLEM algorithm in list-mode data acquisition, one version of the algorithm is presented as improved solution to the Compton image reconstruction problem. Namely, Section 5.2 presents a regularization in wavelet domain of the list-mode MLEM algorithm.

5.1 The list-mode MLEM algorithm

In comparison to the bin-mode MLEM, each measurement in the list-mode MLEM is considered as a unique and infinite small bin, thus $y_i = 1$ for each detected photon, and $y_i = 0$ for the infinite number

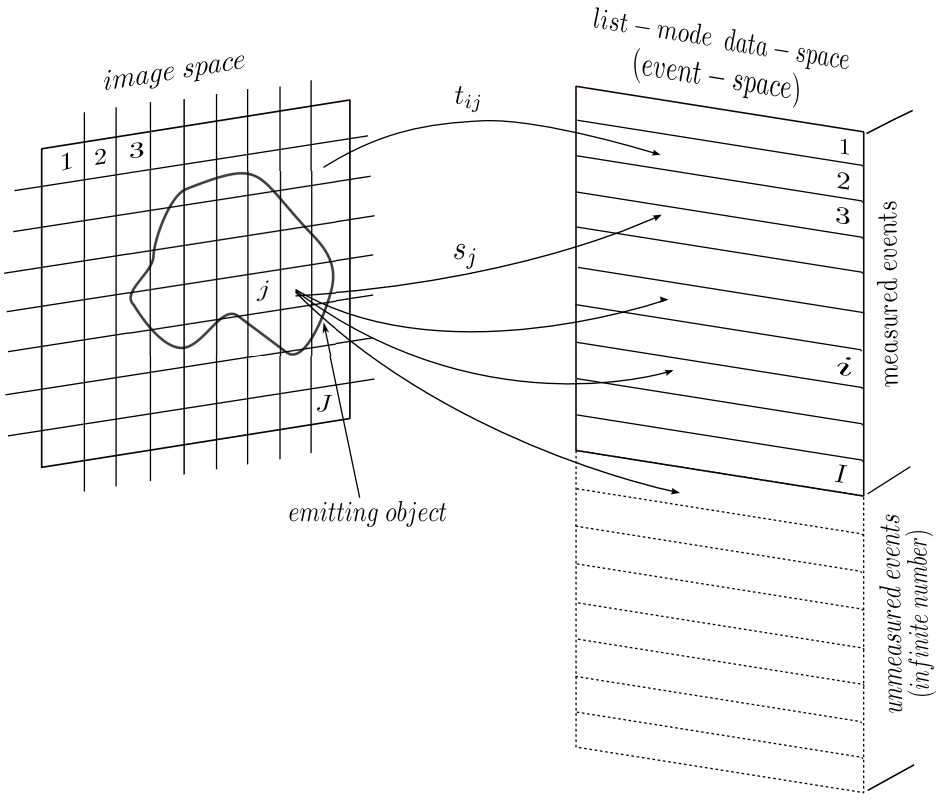

Figure 5.1: Illustration of the relations between data spaces (events space and image space).

events, which are not detected in the current measurement. The value M is the total number of detected measurements instead of the number of detector bins. The image reconstruction purpose is to find the best estimate of the discrete source according to the measurement data set y.

The likelihood function of the list measurements is

$$p(y_1, y_2, \cdots, y_M|f) = \prod_{i=1}^{M} p(y_i|f) \tag{5.6}$$

where $p(y_i|f)$ is the conditional probability density of measuring a single event y_i knowing the event is generated by the source f:

$$p(y_i|f) = \sum_{j=1}^{N} p(y_i|f_j, D)P(f_j, D|f) \tag{5.7}$$

where $p(y_i|f_j, D)$ is the probability density of a detected event generated from f_j, leading to a measurement y_i in the detector. $P(f_j, D|f)$ is the probability of detecting the event which originated in j given the source distribution f

$$P(f_j, D|f) = \frac{f_j s_j}{\sum_{n=1}^{N} f_n s_n} \tag{5.8}$$

The log-likelihood of the list of measurements is [Parra and Barrett, 1998]

$$l(y|f) = \sum_{i=1}^{M} \log \left(\sum_{j=1}^{N} p(y_i|f_j, D) f_j s_j - \sum_{j=1}^{N} f_j s_j \right) \tag{5.9}$$

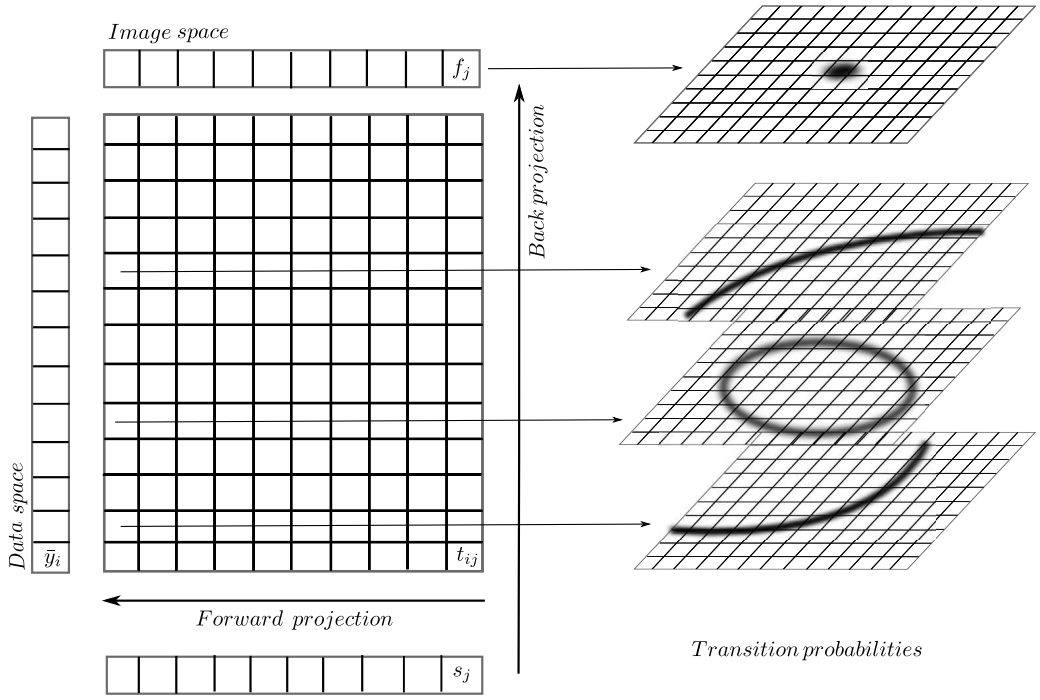

Figure 5.2: Illustration of how the initial image is generated. The transition matrix $T = (t_{ij})$ presents in each bin the probability that the event originates from the given bin. In a visual representation, cone sections appear for each measured Compton event. The addition over all transition probabilities generates the initial image (f^0). Afterwards, the iterative algorithm maximizes the expectation in mainly two steps. First, given the current estimate of the image f and the imaging response t_{ij}, the expectation that this event is measured $\overline{y_i}$ is calculated. This step is basically a forward projection from image to data space. The second step maximizes the expectation and corrects the previous image. This step is basically a backprojection from data into image space.

Similarly to the bin-mode ML criterion, estimating the unknown source f in list-mode requires to find the maximum of Equation (5.9)

$$\hat{f} = \arg\max_{f \geq 0} l(y|f) \tag{5.10}$$

The list-mode ML estimation can also be solved using the iterative EM algorithm. After applying the E-step and the M-step, the estimate of f^{k+1} is

$$f_j^{k+1} = \frac{f_j^k}{s_j} \sum_{i=1}^{M} \frac{p(y_i|f_j, D)}{\sum_{l=1}^{N} p(y_i|f_l, D) f_l^k} \tag{5.11}$$

where $t_{ij} = p(y_i|f_j, D)s_j$.
Finaly, the list-mode MLEM update equation is

$$f_j^{k+1} = \frac{f_j^k}{s_j} \sum_{i=1}^{M} \frac{t_{ij}}{\sum_{l=1}^{N} t_{il} f_l^k} \tag{5.12}$$

The sensitivity is not the sum over the detected events $s_j \neq \sum_{i=1}^{M} t_{ij}$, instead it has to be summed over all possible measurements originating from source element j, including the events for which $y_i = 0$ (see Figure 5.1). The scheme of the algorithm is presented in Table 5.1.

The imaging response matrix $T = (t_{ij})$ represents the transition probabilities generated by the measured events. A measured event is represented in image space by a matrix t_{ij}, where each element gives

Initialization f^0
for each iteration $k := 0$ to $K-1$ **do**
  Projection: $\bar{y}_i = \sum_j t_{ij} f_j^k \quad \forall$ i
  Back-projection: $e_j = \sum_i t_{ij}/\bar{y}_i \quad \forall$ j
  Update: $f_j^{k+1} = f_j^k e_j / s_j \quad \forall$ j
end for

Table 5.1: Scheme of the MLEM algorithm.

the probability that the event i originates from the given bin j. Following [Zoglauer, 2005], Figure 5.1 illustrates the transition from data space (or event space) to source space (or image space). The collection of all measured events forms a first estimation of the source, i.e., f^0, which is also called 'initial image' (Figure 5.2).

Most of the iterative algorithms require the integration of a form of regularization in order avoid artifacts. In case of Compton data reconstruction, this problem occurs especially when the detector response is not approximated by a high fidelity model, e.g., at the 1st approximation of the transition probabilities. Hence, in this case, the more accurate the detector response is modeled, the weak may be the regularization. Therefore, the primary aim should be to determine t_{ij} and s_j as accurately as possible. Calculation of images by means of higher fidelity detector response may usually avoid to include regularization.

Note that the regularized algorithm, which is presented in the following, consider the same initial image as the MLEM algorithm. More precisely, the imaging response t_{ij} is not affected by the regularization included into the reconstruction method.

5.2 Regularization in wavelet domain

In the following, a multiresolution strategy to suppress noise by integrating a Wavelet-based Regularization step into a list-mode accelerated version of MLEM algorithm, called WREM, is proposed [Frandes et al., 2010a]. The approach aims to attain noise control when the iterative method is applied, full precision of all measured information as well as computation efficiency, which is a critical point of iterative Compton image reconstruction. The multiresolution analysis seeks to decorrelate the image pixels allowing to extract only the significant structure, which is related to the data.

The wavelet threshold based methods were efficiently applied to remove white Gaussian noise, which is represented by identically and independently distributed (iid) variables following the normal distribution with mean zero. The pioneering work [Donoho and Johnstone, 1994] proved that various wavelet thresholding techniques have near optimal properties in min-max sense for one-dimensional iid signals estimation. The wavelet coefficients are modified according to a threshold policy. The threshold based methods are efficient when the signal has a sparse representation where most of the signal energy is concentrated on a small subset of coefficients.

Many attempts tried to find the optimal thresholds for parameters estimations in statistics. Here, the noise variance is estimated at each scale of the wavelet decomposition as the median value of the coefficients from the high frequency sub-bands. The regularization of the MLEM algorithm includes at each iteration a thresholding step, which is applied in the wavelet domain. The method has the effect of an inter-smoothing operator allowing to suppress the noise in the reconstructed images.

5.2.1 Wavelet transform and filter banks

Wavelet analysis gives the possibility to access the information of a signal by its localization in both space and frequency domains. Among all possible application fields of wavelet based methods, digital

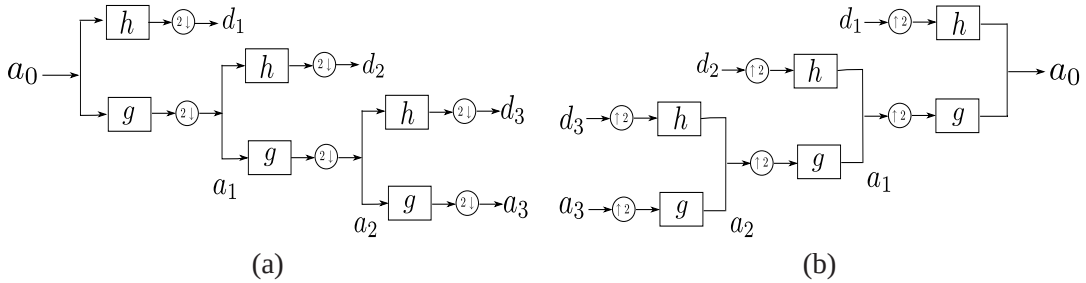

Figure 5.3: Filter bank analysis tree. a_i represent the coarse-scale signals, and d_i the detail coefficients. (a) At each decomposition level, the generated outputs are subsampled by a factor 2. (b) At each reconstruction level, the generated coefficients are upsampled by a factor 2.

image processing is probably the most visible one. Most studied problems and proposed solutions are from one-dimensional signal processing, having an equivalent in image processing.

Wavelet transforms can be classified into continuous wavelet transforms (CWTs), and discrete wavelet transforms (DWTs). CWTs operates over every possible scale and translation, while DWTs use a specific set of scale and translation values. CWTs are described in [Daubechies, 1992].

The DWT analyzes the signal at different resolutions by decomposing it into coarse and detail approximations. DWT uses two sets of functions, called scaling functions and wavelet functions, which are associated with low-pass g and high-pass h filters, respectively. Both filters correspond to a certain chosen wavelet basis [Mallat, 1999].

The signal decomposition is represented as a binary tree with nodes which represent a sub-space with a different space-frequency localizations. The tree is known as a filter bank (Figure 5.3).

The wavelet and scaling function coefficients on a certain scale l follow the equations

$$\begin{cases} d_l(k) = \sum_{n\in\mathbb{Z}} h(2k-n)a_{l-1}(n) \\ a_l(k) = \sum_{n\in\mathbb{Z}} g(2k-n)a_{l-1}(n) \end{cases} \tag{5.13}$$

where the low-pass filter g and the high-pass filter h are constructed from the mother scaling function, and jointly the wavelet and scaling functions, respectively. The $d_l(k)$ and $a_l(k)$ are the detail coefficients at the level l (i.e., the wavelet coefficients), and the approximation coefficients at the level l (i.e., the scale coefficients), respectively.

The discrete wavelet decomposition of the signal a_0 may be described as follows

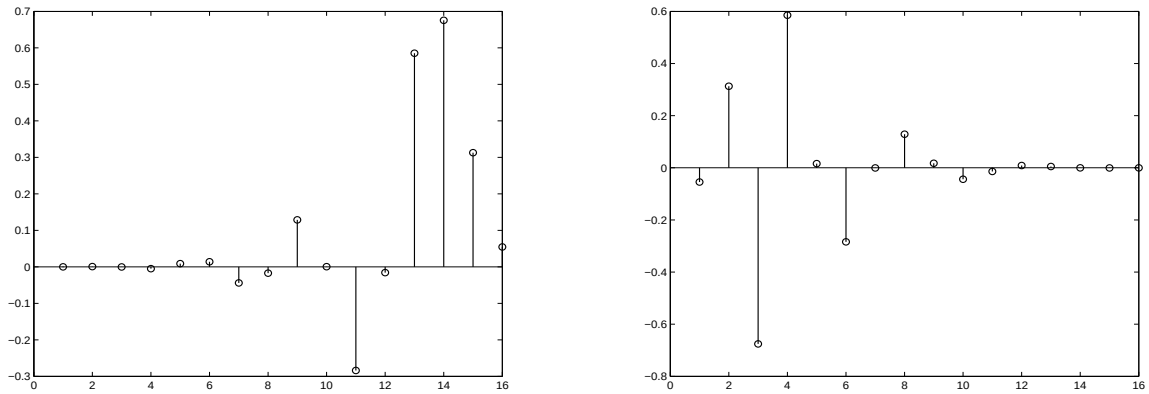

Figure 5.4: Graphical representation of the Daubechies 8 analysis (a) low-pass, and (b) high-pass filters.

$$a_0(n) = \sum_{k\in\mathbb{Z}} \tilde{g}(n-2k)a_L(2k) + \sum_{l=1}^{L}\sum_{k\in\mathbb{Z}} \tilde{h}(n-2k)d_l(2k) \tag{5.14}$$

where the low-pass filter $\tilde{g}$, and the high-pass filter $\tilde{h}$ are the reconstruction filters derived from the analysis filters g and h, respectively. The parameter L represents the finest scale in the wavelet decomposition. For example, the Daubechies 8 analysis filters are represented in Figure 5.4.

In case of a $2D$-signal, the wavelet separable transform is performed by first decomposing each column of the image, and then decomposing each row of the result to obtain the rows of the wavelet coefficients matrix. Four frequency bands will be obtained after one level of decomposition, namely Low-Low (LL), Low-High (LH), High-Low (HL) and High-High (HH). Application of the next level of decomposition is done to only the LL band of the current decomposition creating a recursive decomposition procedure (Figure 5.5). The sub-bands LH_l, HL_l, HH_l, $l = \overline{1,L}$ represent the detail coefficients $d_{l,n}(k)$, and the sub-band LL_L is the low resolution image, i.e., the approximation coefficients $a_L(k)$, where n denotes the subband, and k the spatial position.

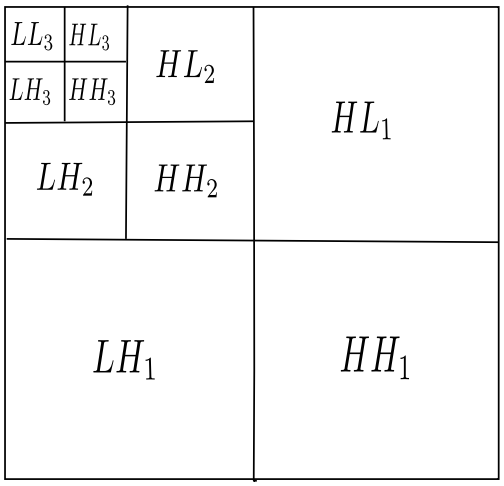

Figure 5.5: Schematic representation of the structure generated by applying a 2D-DWT with three decomposition levels of an input image. The coefficients $d_{l,1} \in HL_1$, $d_{l,2} \in LH_l$, $d_{l,3} \in HH_l$, $l = \overline{1,3}$ represent the image details, while $a_3 \in LL_3$ represents the approximation coefficients of the low resolution image.

5.2.2 Noise reduction methods by wavelet thresholding

A classical approach in image de-noising proposes the combination of the wavelet transform with a non-linear thresholding of the wavelet coefficients. Standard methods [Donoho, 1993] address de-noising of signals contaminated by additive white Gaussian noise. Various wavelet thresholding techniques were investigated; the reference ones are the universal threshold proposed by [Donoho et al., 1995], the sub-band adaptive scheme [Donoho and Johnstone, 1995], and the Bayesian approach [Chang et al., 2000].

Nuclear medical images are generally modeled as the realization of a Poisson process. The Poisson noise, i.e., variations of the signal from its mean, is not data-independent as it is assumed by general Gaussian case, but it follows the image intensities. Thus the direct application of a Gaussian based standard wavelet thresholding method has proved to be inappropriate. The investigated approaches include the application of a first pre-processing step, which aims to stabilize the noise variance, followed by the analysis of the resulting data in a Gaussian framework. The pre-processing step may be computed using, e.g., the Anscombe transform [Anscombe, 1948], or the Fisz transform [Fisz, 1955]. The Anscombe procedure defines, for a given signal $u \geq 0$, its Gaussian counterpart

$$\mathcal{A}(u) = 2\sqrt{u + 3/8} \tag{5.15}$$

The Fisz's method implies the application of the non normalized Haar wavelet transform followed by the detail coefficients transformation as

$$\mathcal{F}[d_{l,n}(k)] = \begin{cases} d_{l,n}(k)/\sqrt{a_l(k)} & \text{if } a_l(k) \neq 0 \\ 0 & \text{if } a_l(k) = 0 \end{cases} \tag{5.16}$$

Finally, the signal is reconstructed using the inverse non normalized Haar transform.

In the context of Poisson data, an approach based on a Bayesian inference was proposed by [Timmermann and Nowak, 1999], in which a prior distribution is placed in wavelet coefficients, and a l_1-penalized likelihood method by [Sardy et al., 2004].

When the data are corrupted by a noise integrated in a mixed Poisson-Gaussian model, the Generalized Anscombe transform [Murtagh et al., 1995] is adopted as solution to stabilize the noise variance.

Considering the measured signal u as a sum of a Gaussian variable G, of mean μ_G, and standard deviation σ_G; and a Poisson variable P, of mean μ_P, the signal model is set to $u = G + \alpha P$, where α is the mixing coefficient. The Generalized Anscombe transform is defined as

$$\mathcal{GA}(u) = \frac{2}{\alpha}\sqrt{\alpha u + 3/8\alpha^2 + \sigma_G^2 - \alpha\mu_G} \tag{5.17}$$

The application of this transform is conditioned by the knowledge of the statistical properties of both noises.

5.2.3 Wavelet-based multiresolution EM

5.2.3.1 The method

The proposed iterative algorithm is based on the list-mode MLEM algorithm derived from the equation (5.5). In list-mode, each detected event is considered as a unique bin. The sensitivity factor s_j is difficult to calculate since the integration is done over both scatter and absorption detectors, and over all the possible energies and scattering angles. Following [Wilderman et al., 1998b], s_j was set constant (s_j = 1, $\forall j$).

The proposed de-noising method consists on the integration of a wavelet analysis into the iterative procedure aiming to decorrelate the image pixels and to only reconstruct of the significant structures from the measured data. First, the transformation of the data into the wavelet domain is done by applying DWT with orthogonal Daubechies wavelets, where the length of the filter is 8. The correction factor is now represented by the obtained wavelet coefficients $d_{l,n}$, where l represents the wavelet level, and n the sub-band index.

The soft-thresholding operator η_S is defined by

$$\eta_S(d_{l,n}(k), \tau_{l,n}) = sgn(d_{l,n}(k))\ max(0, |d_{l,n}(k)| - \tau_{l,n}) \tag{5.18}$$

The employed wavelet threshold depends on the decomposition level, and follows the expression

$$\tau_{l,n} = 2^{2(L-l)} q\ \sigma_{l,n} \tag{5.19}$$

The noise variance $\sigma_{l,n}$ was estimated by the median of the coefficients at each HH_l subband. The parameter q denotes the threshold coefficient, which is equaled to $2^2 M^{-1}\sqrt{2logM}$, where M is the number of pixels in the image.

The inverse DWT is then applied to the wavelet coefficients, which result after the thresholding step. This leads to a de-noised image $\bar{f}^k$.

The wavelet processing step may be expressed by the following notation

$$\bar{f}^k = \mathtt{W}[f^k] = DWT^{-1}\eta_S DWT f^k \tag{5.20}$$

In the last step, the estimate $\bar{f}^k$ is updated using (5.5), with one subset.

Initialization f^0
for each iteration $k := 0$ to $K-1$ **do**
  Projection: $\bar{y}_i = \sum_j t_{ij} f_j^k \quad \forall$ i
  Back-projection: $e_j = \sum_i t_{ij}/\bar{y}_i \quad \forall$ j
  Regularization: $\overline{f}_j^k = \mathtt{W}[f_j^k] \quad \forall$ j
  Update: $f_j^{k+1} = \overline{f}_j^k e_j / s_j \quad \forall$ j
end for

Table 5.2: Scheme of the WREM algorithm.

5.2.3.2 Thresholding scheme

The iterative method starts with a positive distribution computed as the following

$$f_j^0 = \sum_{i=1}^{N} t_{ij} \tag{5.21}$$

Considering the central limit theorem, the estimated distribution of the data follows approximately a normal distribution, after several iterations. Hence, the application of wavelet thresholding is appropriate without including variance stabilization technique as described in Section 5.2.2, or in [Frandes et al., 2009]. Herein, the wavelet technique is empirically applied after 4 iterations. The DWT with four levels of decomposition ($L = 4$ in Equation (5.19)) was employed, and the wavelet thresholding step was applied at all detail sub-bands.

At each iteration, the noise variance $\sigma_{l,n}$ is estimated by the median operator applied to the wavelet coefficients at the each scale,

$$\sigma_{l,n} = median_k(|d_{l,n}(k)|),\ d_{l,n} \in HH_l,\ l = \overline{1, L} \tag{5.22}$$

Following [Johnstone and Silverman, 1997], the standard deviation is defined as the robust median estimator. It has been proved to be efficient for cases when noise is correlated to data.

5.3 Results

The Compton scattered projection data was generated by Monte Carlo simulations for a Compton camera using MEGAlib [Zoglauer et al., 2006], a Geant4 based simulation code. The lists of the exact interaction positions and energy deposits as well as the uncertainties in the measurements were recorded. The program read the data in list-mode applying a back-projection algorithm, which is based on [Wilderman et al., 2001]. The coefficients of the system response matrix $T = (t_{ij})$ were computed and stored.

The simulated detector system is a generic Compton scattering camera, which was designed as a simplified model of the HTI (Hadron Therapy Imaging) system proposed in [Frandes et al., 2010b], being also described in Figure 2.4. The first detector is made of a single double-sided Silicon strip layer, which consists of one wafer with a length of 10 cm, thickness of 2 mm. The wafer has 128 orthogonal strips per wafer side (0.5 mm pitch). The top and bottom sides of the wafer are p and n doped, respectively. An uniform 1-sigma energy resolution of 1 keV was assumed, along with a 10 keV threshold. The second

detector consists of $LaBr_3$ bars (surface area: 5×5 mm, length: 8 cm). An energy resolution of 4.3% FWHM at 662 keV, and a threshold of 28 keV was assumed.

The quality of the reconstructed images was evaluated considering the Mean Squared Errors (MSE) defined as

$$MSE^k = \frac{1}{M^2} \sum_{i=0}^{M-1} \sum_{j=0}^{M-1} \left[\frac{f(i,j)}{\max_f} - \frac{\bar{f}^k(i,j)}{\max_{\bar{f}^k}} \right]^2 \tag{5.23}$$

where $\max_{\mathbf{f}}$ is the maximum of original image values, while $\max_{\bar{f}^k}$ is the maximum of reconstructed image values at iteration k. The MSE was defined knowing the algorithm does not include normalization.

The error of Contrast Recovery (CR) is defined as the difference between the ratio of the maximum point of the spot, denoted $\max_s$, and the background, denoted $\max_b$, respectively, of the reconstructed images R_r, and the original ratio R_o.

$$\text{Error}_{CR} = |R_r - R_o| \tag{5.24}$$

where $R_r = \frac{\max_s}{\max_b}$. The spot on background source is illustrated in Figure 5.6 (b).

Two simulation cases were considered, one where ideal Compton events are assumed, and the other including measurement uncertainties. For both cases, the number of stored projections is constrained by the storage size of the coefficients t_{ij}. The energy considered was 364 keV (^{131}I).

5.3.1 Ideal simulations

First, the performance of both algorithms was analyzed by ideal simulations, i.e., assuming ideal Compton events into the imaging detector. Ideal events represent events which are not affected by the finite position and energy resolution of the detector, but include Doppler broadening.

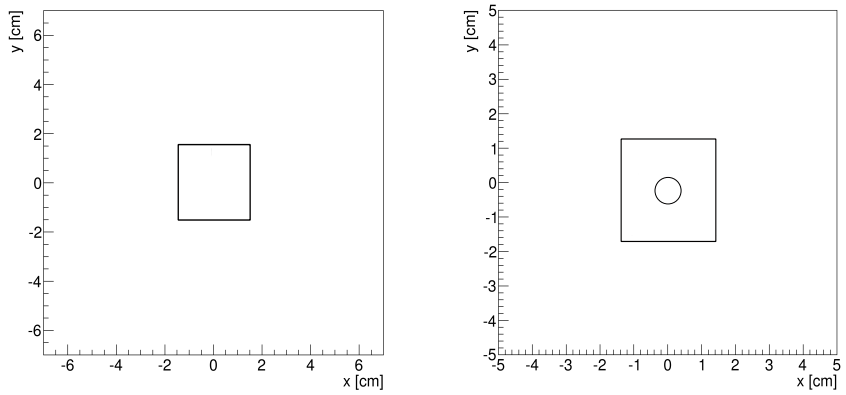

(a) (b)

Figure 5.6: Geometry of the (a) square source, and (b) spot on a background source at $z = 12$ cm.

Figure 5.6 illustrates the geometry of ideal events generated by the considered gamma-ray sources, which represent a 3×3 cm^2 square source (BoxSource in Cosima [Zoglauer et al., 2006], Figure 5.6 (a)), and a spot placed at the center of a 3×3 cm^2 uniform rectangle (i.e., background), (BoxSource and SphereSource in Cosima, Figure 5.6 (b)). The first source was placed at a distance of 2 cm above the scattering detector, at the center of the xy-axis. The second simulation test includes the source in which a central spot activity was placed. The spot is represented by a sphere of 0.5 cm radius, and

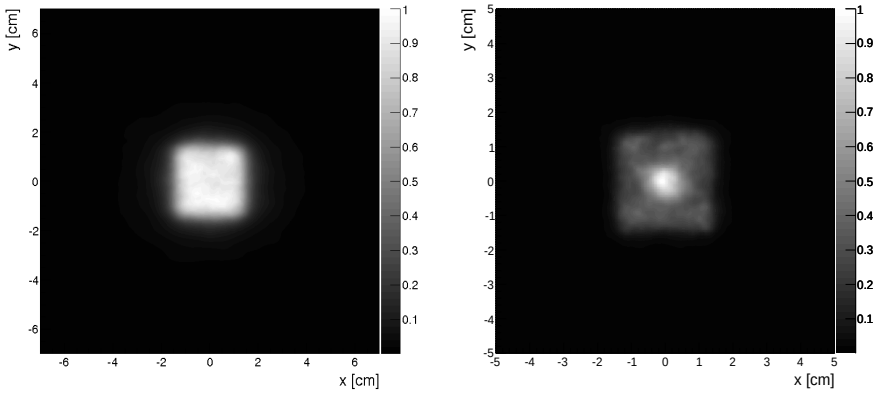

(a) (b)

Figure 5.7: Ideal events. Reconstructed image using the proposed WREM algorithm considering (a) the square source, (b) the spot on a uniform background source.

an intensity level of 3 standard deviation above the background. Both square and background uniform sources contained 100 Poisson distributed counts per bin.

Considering ideal events, similar performance using MLEM and WREM algorithms was observed. Figure 5.7 shows the reconstructed images using the WREM algorithm after (a) 24 iterations, in case of the square homogeneous source, and (b) 14 iterations, in case of the spot on background source.

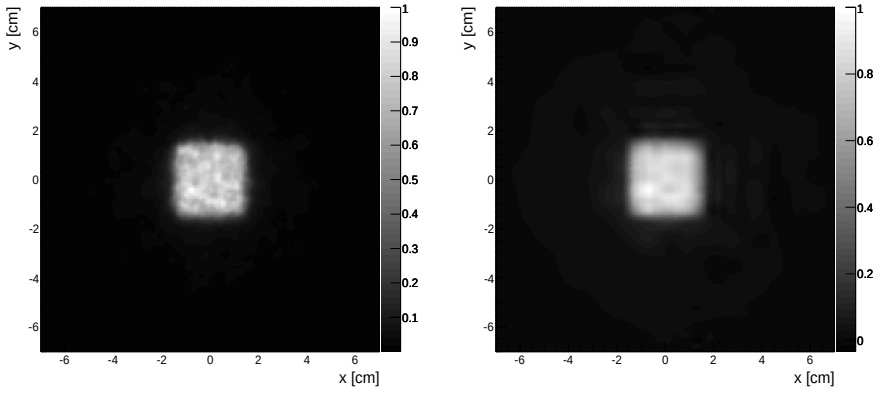

(a) (b)

Figure 5.8: Realistic simulation. Reconstructed images of the square source (a) using the classical MLEM algorithm, (b) using the proposed WREM algorithm.

5.3.2 Realistic simulations

Homogeneous source

Emissions from the 3×3 cm^2 square homogeneous distribution were sampled until $124\ 146$ Compton events were reconstructed. Figure 5.8 presents the images reconstructed using the classical MLEM algorithm and our wavelet based algorithm WREM, respectively, after 16 iterations.

The intensity profiles of the reconstructed images along the central horizontal line are illustrated in

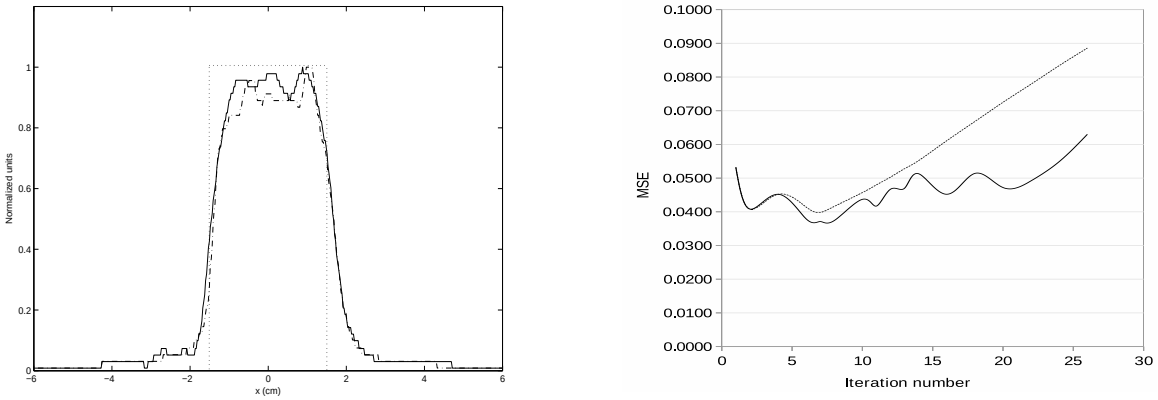

(a) (b)

Figure 5.9: Uniform square source with realistic simulation. (a) Plot of the central line intensity profile of the square source. Original source (box), the reconstructed image obtained using the MLEM algorithm (dotted line), and the reconstructed image obtained using the WREM algorithm (continuous line). (b) Mean Square Error of the images reconstructed using the classical MLEM algorithm (dotted line) and the WREM algorithm (continuous line).

Figure 5.9 (a). Clearly, the WREM algorithm results in a higher homogeneous gray level distribution than the MLEM algorithm. Moreover, the classical MLEM algorithm presents a larger reconstruction error, meanwhile the wavelet based algorithm maintains a rather constant evolution of the error, when the iteration number was increased (Figure 5.9(b)).

Spot on background

Figure 5.10 (a) illustrates the image reconstructed using the classical MLEM algorithm. The central hot spot is partially retrieved presenting a central cold spot. The application of the WREM algorithm results in a more accurately reconstructed original source (Figure 5.10 (b)).

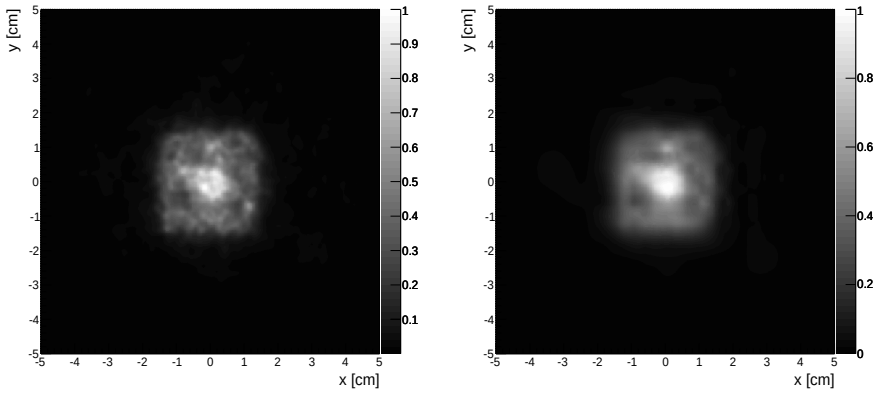

(a) (b)

Figure 5.10: Realistic simulation. Reconstructed images of the spot on a uniform background (a) using the classical MLEM algorithm, (b) using the proposed WREM algorithm.

For both images, the reconstruction plane intersects the center of the spot, i.e., at $z = 12$ cm.

Figure 5.11 (a) presents the error of contrast recovery (5.24), while Figure 5.11 (b) presents the mean square error (5.23), as a function of the iteration number. Indeed, considering both error measures, the

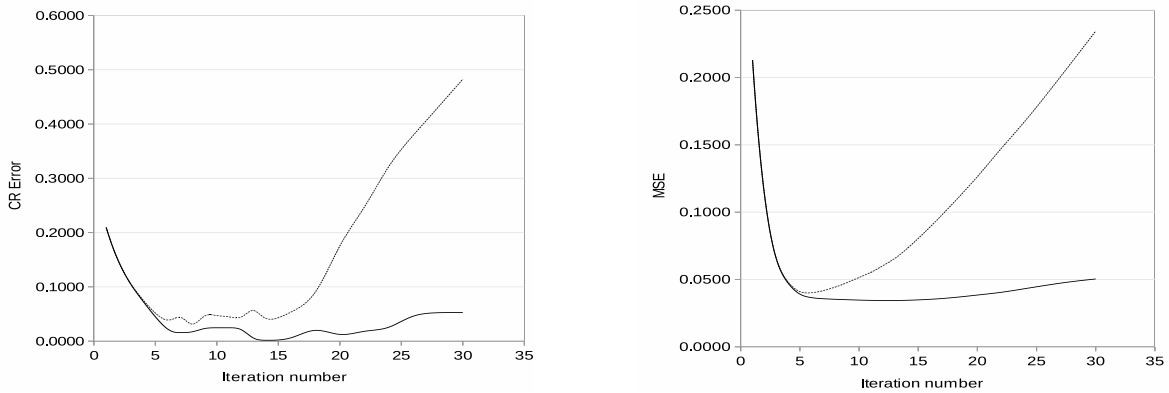

(a) (b)

Figure 5.11: Spot on a uniform background with realistic simulation. (a) Contrast Recovery Error of the reconstructed images using the classical MLEM algorithm (dotted line) and the WREM algorithm (continuous line). (b) Mean Square Error of the reconstructed images using the classical MLEM algorithm (dotted line), and the WREM algorithm (continuous line).

classical MLEM algorithm results in an unpredictable optimal iteration number for an acceptable error. Note that the noise in the data is represented by all the uncertainties which inherently arise during the measurement process.

A more dramatic difficulty in using the MLEM algorithm is that it is divergent. In sharp contrast, the proposed WREM algorithm results in lower errors than the MLEM algorithm, and, in addition, it is stable. This result is due to the regularization induced by the shrinkage of the wavelet coefficients.

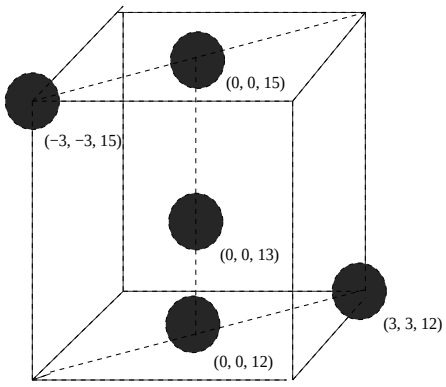

Figure 5.12: Schematic representation of the simulation configuration, which consists of five sources placed at different distances above the detector. Each spot is labeled with the axis coordinate of its center.

Spots on 3D

A third configuration considered sources at different distances from the imaging detector: five spheres of the same radius, i.e., 0.25 cm, and the same intensity, i.e., 200 uniformly distributed Poisson counts per bin. Two spheres were placed at 2 cm above the detector at the center of the axis, i.e., $(x, y, z) = (0, 0, 12)$, and at $(x, y, z) = (3, 3, 12)$, respectively.

At a distance of 3 cm above the detector at the center of the axis were placed one sphere, and two spheres at a distance of 5 cm, i.e., $(x, y, z) = (0, 0, 15)$ and $(x, y, z) = (-3, -3, 15)$, (Figure 5.12).

The reconstruction was done at different depth planes according to the considered configuration. Figures 5.13 (a) illustrates the image reconstructed at the plane corresponding to $z = 12$ cm of the coordinate system, i.e., the plane which intersects the center of the two sources placed nearest to the front of the scattering detector. As expected, the off-center source was more difficult to reconstruct. Figures

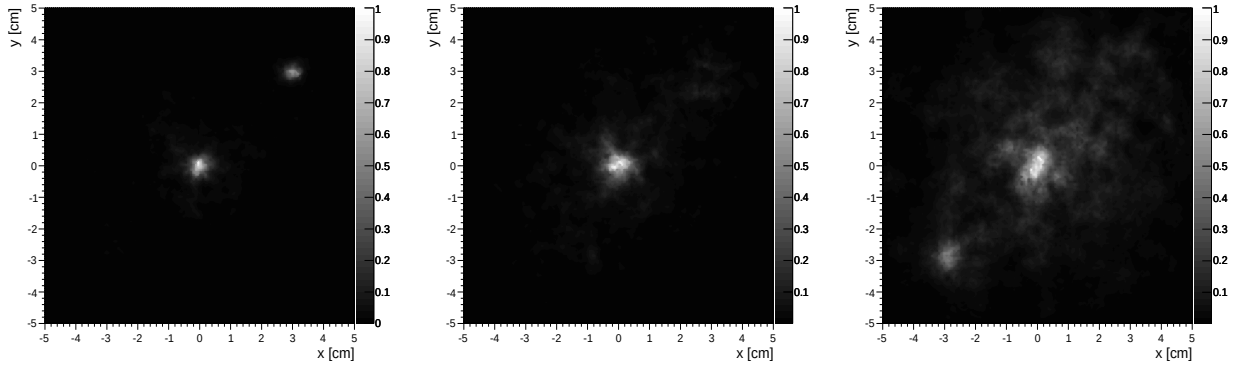

(a) (b) (c)

Figure 5.13: Realistic simulation. Reconstructed images of the multiple spots source using the MLEM algorithm. The reconstruction plane is situated at (a) $z = 12$ cm, (b) $z = 13$ cm, (c) $z = 15$ cm.

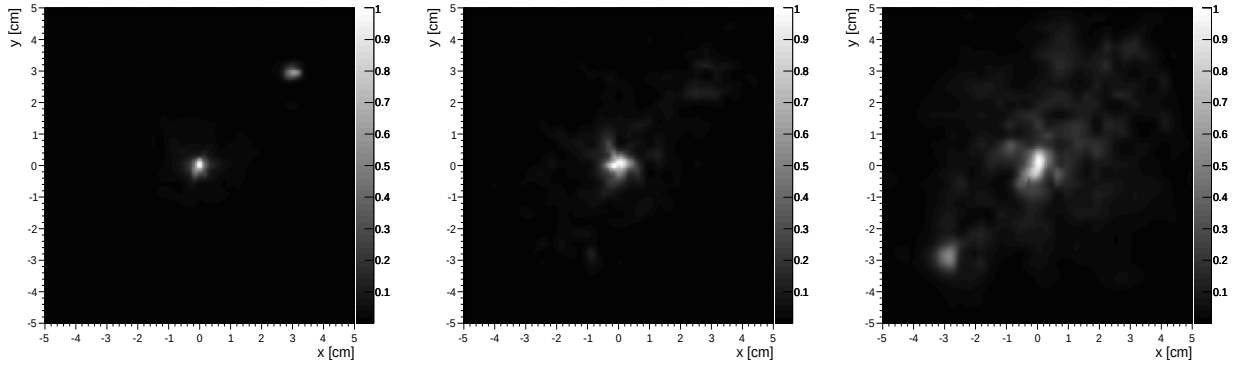

(a) (b) (c)

Figure 5.14: Realistic simulation. Reconstructed images of the multiple spots source using the WREM algorithm. The reconstruction plane is situated at (a) $z = 12$ cm, (b) $z = 13$ cm, (c) $z = 15$ cm.

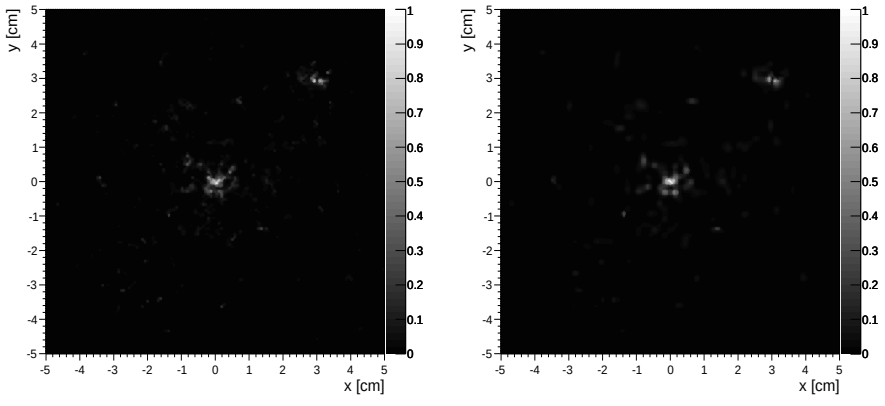

(a) (b)

Figure 5.15: Realistic simulation. Reconstructed images of the multiple spots source using the MLEM algorithm (a), and the WREM algorithm (b). The reconstruction plane is situated at $z = 11.75$ cm

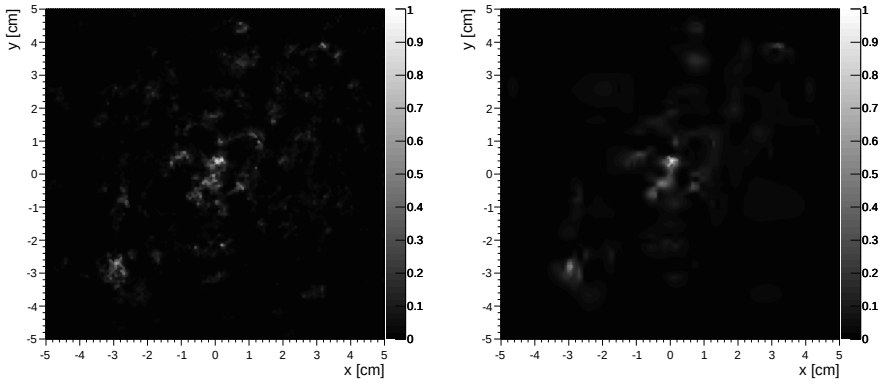

(a) (b)

Figure 5.16: Realistic simulation. Reconstructed images of the multiple spots source using the MLEM algorithm (a), and the WREM algorithm (b). The reconstruction plane is situated at $z = 15.26$ cm

5.13 (b), (c) illustrate the images reconstructed at the other two altitude planes intersecting the center of the spheres. Considering tangential planes to the source, Figure 5.15, and Figure 5.16 present the reconstructed images using both algorithms. Clearly, our approach reduces the reconstruction artifacts.

5.4 Application to multi-energy source

The regularized version of the list-mode MLEM algorithm, presented in Section 5.2.3, was applied to reconstruct multi-energy Compton events. The events were generated by the HTI system when considering the simplified hadron therapy scenario presented in Section 4.1. Only the proton beam at 140 MeV was considered, and the same analysis tools as described in Section 4.3.4 were applied.

Profiles of the reconstructed images along the central vertical and horizontal lines were considered, and compared to the ones extracted from the images reconstructed using the classical list-mode MLEM algorithm.

Figures 5.17, 5.18 show the horizontal profiles of the reconstructed images using list-mode MLEM, and WREM algorithm, when considering different iteration numbers. At the first iterations, a broader horizontal profile is observed. When increasing the iteration number, the profile becomes sharper (Figure 5.19), being closer to the dose profile along the x-axis (see the simulation configuration in Section 4.1), or the profile of emitted gamma rays in the first second of PMMA phantom irradiation by the proton beam.

When comparing the horizontal profiles of the reconstructed images using alternatively the classical MLEM, and its wavelet regularized version WREM, a superior behavior of the WREM algorithm is observed. Figure 5.20 shows the profiles depicted at different iteration numbers, ranging from a low iteration number to the iteration where the WREM algorithm is stable, i.e., no changes of the profiles occur when increasing the iteration number. When considering the vertical profiles, observable differences can be noticed from one iteration to the next. Namely, the classical algorithm generates iteration dependent reconstructed images, while the WREM algorithm presents lower variability of the extracted vertical profiles, becoming stable at an earlier iteration number. Figure 5.21 shows both the horizontal and vertical profiles of the reconstructed images at the optimal iteration number of the MLEM and WREM algorithms. A similar behavior of both algorithms can be observed.

When applying the WREM algorithm to multi-energy sources, a real drawback is represented by the incompletely measured events, when going from lower to higher energies. Thus an accurate description of those events is highly desirable.

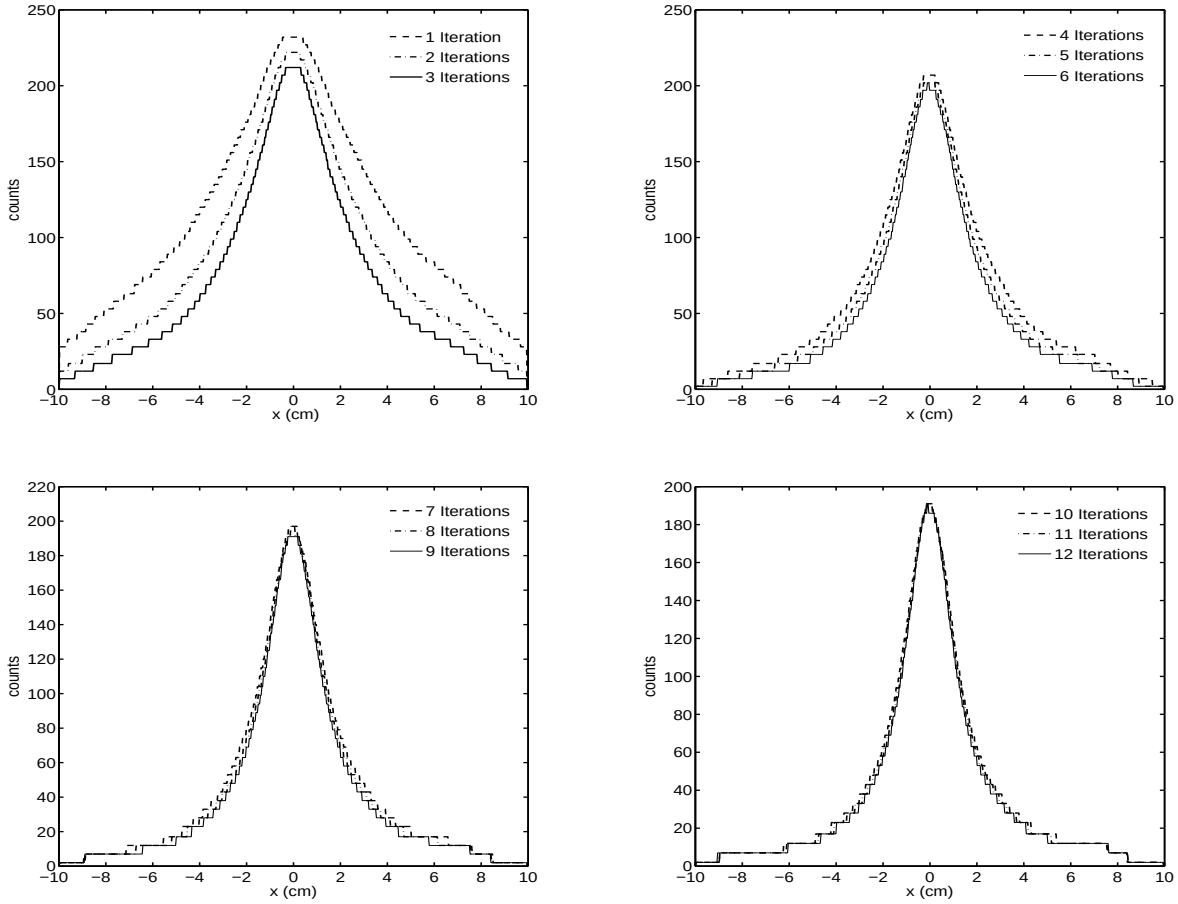

Figure 5.17: Profiles along the central horizontal line of the reconstructed images using the classical MLEM algorithm, when considering different iterations of the algorithm.

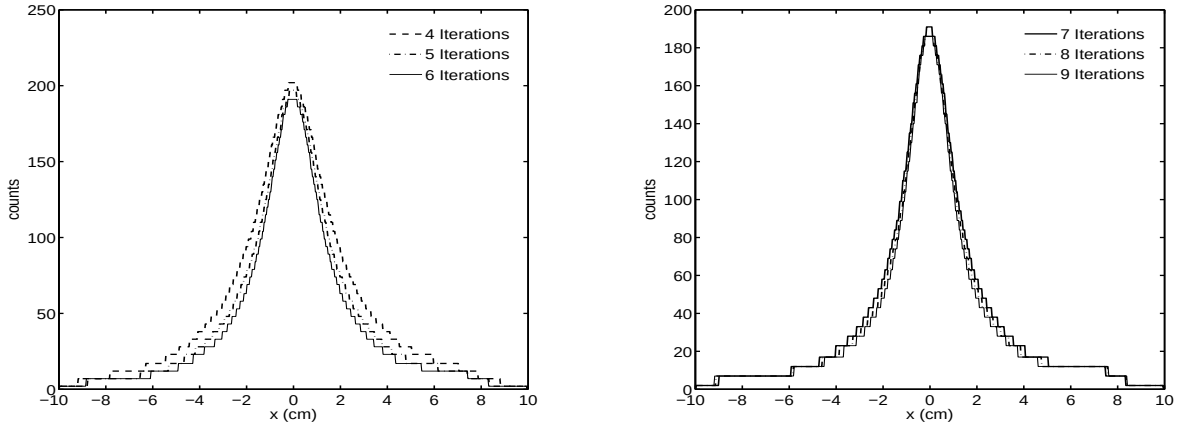

Figure 5.18: Profiles along the central horizontal line of the reconstructed images using the WREM algorithm, when considering different iterations of the algorithm.

5.5 Discussion

The performance of the wavelet domain de-noising methods applied to the iterative classical MLEM algorithm for Compton scattered data depends on several considerations.

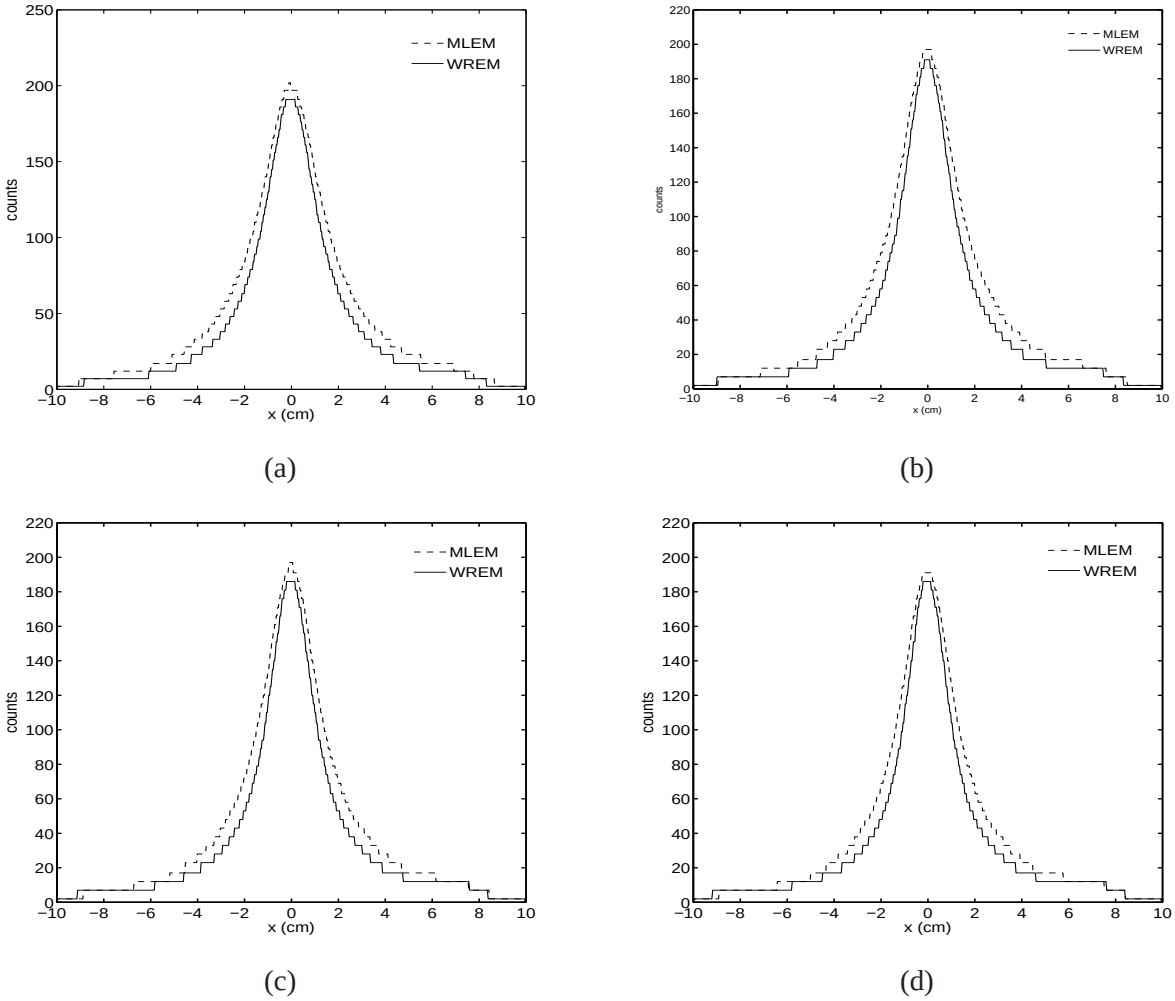

Figure 5.19: Profiles along the central horizontal line of the reconstructed images using the MLEM and WREM algorithms at (a) 6 iterations, (b) 7 iterations, (c) 8 iterations, (d) 9 iterations.

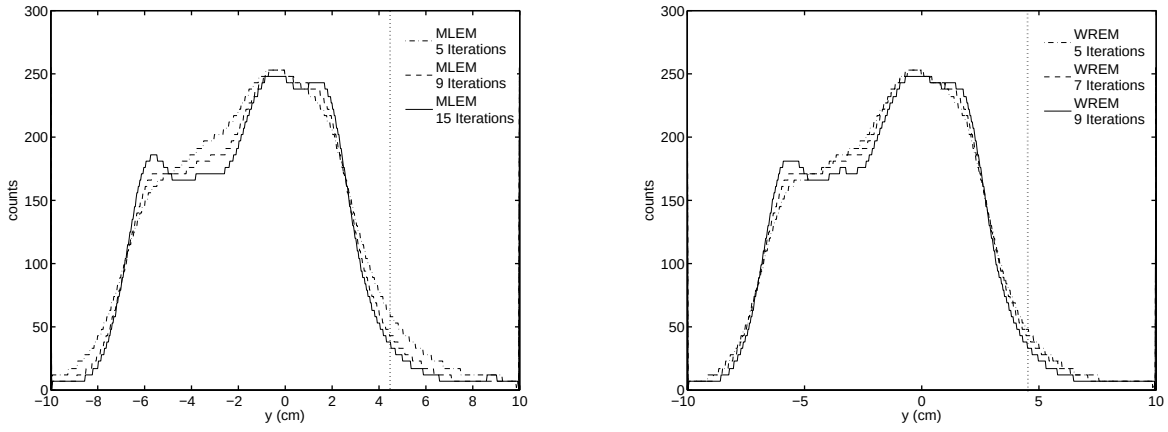

Figure 5.20: Comparative profiles along the central vertical line of the reconstructed images.

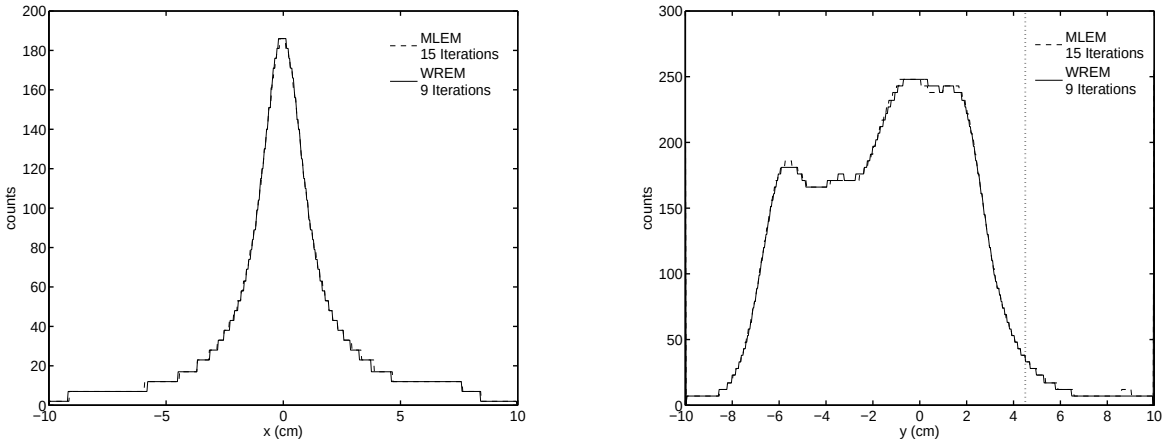

Figure 5.21: Comparative profiles along the central (a) horizontal line, (b) vertical line of the "best" reconstructed images.

Efficient wavelet domain de-noising may be achieved when knowing the statistical properties of the noise in data. In addition, the noise should be data-independent when the wavelet thresholding method is applied. A generally used method to improve the de-noising procedure is the integration of 'a priori' knowledge about the source distribution, and the noise variance, or both, creating object-dependent solutions. However, a practical procedure may not have this information.

The Compton imaging response is influenced by the uncertainty of measurements (e.g., energy, position), the detector geometry, read-out noise, and Doppler broadening. The data measured have high dimensionality, and are incompletely sampled in the scattering angle. Each of these difficulties introduces its own uncertainty distribution into the resulting data. Roughly speaking, all these uncertainties can be considered as noise in data. Thus wavelet coefficients shrinking alleviate that noise, and provides a stable iterative method. In addition, the Compton cones do not intersect when full energy has not been deposited in the camera. Therefore, a further step would be to adopt a combined spatial-spectral deconvolution [Xu and He, 2007]. Moreover, in list-mode acquisition, computing the absolute normalization to recover the source flux is difficult. This drawback is the reason why the reconstructed images were normalized when the analysis of algorithms was performed.

The model of the imaging detector response plays an important role in the achievable resolution of the reconstructed images. The response of each event is described by Compton cone profiles. A profile represents the distribution of possible true event cones from the measured one, and the distribution of true scatter planes from the measured one. In this study, the profile shape is estimated by 1D Gaussian distributions, which represent the simplest approximation form. Hence, it may be considered that Compton measurement data follow more complex statistical properties than the classical projection data generated in nuclear medicine (PET, SPECT).

Consider a point source of 10 MeV placed at 8 cm above the HTI system. The measured ARM as a function of the measured energy for the known source position is represented in Figure 5.22.

It can be seen that the ARM distribution is strongly influenced by the measured energy, i.e., the distribution becomes more or less broaden according to the amount of incompletely absorbed events. Therefore, a possible way of imaging response approximation is to include the measured energy information when retrieving the cone section profiles. Note that other dependence parameters (e.g., measured Compton cone, distance between the first two interactions) may be further included.

The energy integrated imaging may be achieved by adopting a partially list-mode approach to store the imaging response. A binned matrix is then used to store the cone profiles as a function of the measured energy. Afterwards, the corresponding slice of the response is fitted along the measured cone section.

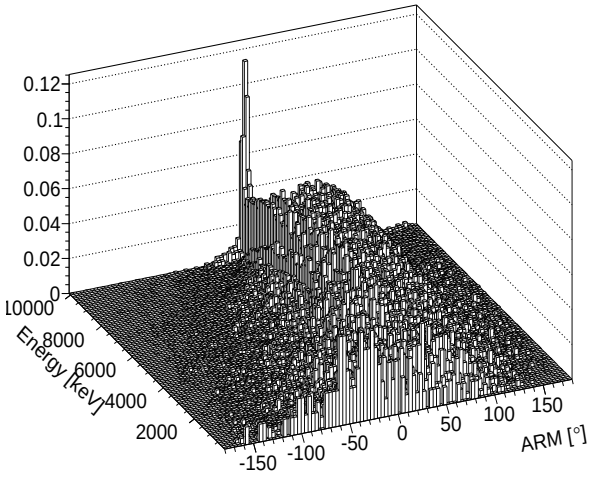

Figure 5.22: Graphic representation of the ARM vs. measured energy. The ARM peak is measured at the incident energy (10 MeV), where full-absorption events were recorded. The ARM distributions change according to the amount of measured energy, being more broaden where events escaped from the detector, i.e., incompletely absorbed events.

Other approach to handle incompletely absorbed events is to derive analytically the energy integrated response [Xu and He, 2007]. In list-mode data acquisition, an approach is to expand the response model to also integrate the measured energy, i.e., improve the model which describe the cone-section profiles of measured Compton events. One back-projection is then represented by the spatial information (angles θ, ϕ), and the measured energy E, i.e., the j dimension describing the contribution of event i in the image space is represented by (θ, ϕ, E).

5.6 Conclusion

A regularization technique based on wavelet thresholding was introduced into an iterative MLEM reconstruction, and evaluated on simulated Compton scattered data. The main advantage of the proposed WREM algorithm is its stability in terms of error versus the number of iterations used. The current threshold value depends on the wavelet decomposition scale. The noise variance was computed using the high subbands wavelet coefficients, assuming they contain most of the noise in the data, i.e., the noise is white. The Daubechies 8 wavelets were applied since their response generally provides a good space-frequency localization.

Further work seeks the study of the optimal model framework enabling consistent estimation of the expected noise characteristics as well as the integration of all dependence parameters related to the Compton data measurement process. The latter would result in a higher fidelity detector response model, and thus improving the signal-to-noise ratio. Note that efficient implementation of the algorithm could be achieved by using an architecture exploiting parallel processing of data (e.g., multiple cores, GPU).

Chapter 6

Closing remarks

Hadron therapy is a new radiation therapy technique with advanced dose distribution located at a precise point well known as Bragg peak. Further improvement in hadron therapy is possible with real time quality assurance (QA) of dose delivery. The precise knowledge of the distal fall-off position of the dose with millimeter accuracy is critical since very often hadron therapy is used for the treatment of a tumor which is close to vital organs. One solution for tracking of heavy ion and proton beam dose distribution is the measurement of positrons emitting isotopes activity using PET technology. The generated PET images are correlated, but not in direct coincidence with the Bragg peak.

Chapter 4 presented investigatory work about QA in proton therapy by considering the reconstruction of gamma rays originated from inelastic interactions of protons to target nuclei. To reconstruct these high-energy gamma events, the Compton camera with electron tracking possibility was proposed and modeled. The proposed Compton detection technique was initially developed to observe gamma rays in the MeV region from the universe. Herein, the imaging device illustrating this detection method was redesigned and optimized for hadron therapy imaging to observe gamma rays from an object, which is represented by a PMMA phantom. Monte Carlo simulations of the emitted gamma photons profiles in the phantom for pencil proton beams is presented along with energy deposition of protons. Assuming a hadron therapy scenario, the reconstructed images derived from numerical experiments with Geant4 are shown. A correlation was observed between the pattern of the reconstructed high-energy gamma events, and the location of the Bragg peak. The capacity of the HTI imaging technique has to be viewed as a function of at least several parameters: the detector performance in terms of detection efficiency as well as spatial and energy resolutions, the acquisition time, and the algorithms used to reconstruct the gamma-ray activity.

Two main challenges arise when considering an imaging system based on Compton scattering: the detector optimization and data analysis. The first challenge demands the choice of e.g., the detector materials as well as the geometry configuration. Data analysis has to cover the complete chain from measurements or simulations to reconstruction of individual events, and finally to image reconstruction. The latter requests the existence of a model describing the imaging response, which has to depict the complex behavior of the detector. In addition, besides the performance of the imaging algorithm, the resolution of reconstructed images is affected by the count statistics. A reasonable solution would be to add more detectors to the imaging system, e.g., two detectors at 90° one from the other. However, this improvement would need large memory resources to store and analyze the Compton events.

Each measured event creates a single-event image response. The response is approximated by the profile of the cone, or the length of the arc, in case of tracked events. The profile is determined by the measurements of the scattered gamma-ray energy E_g, the recoiled electron energy E_e, the Doppler broadening, the spatial resolution of the detector. The length is mainly determined by the direction and energy of the recoiled electron. For each event, the transition probabilities t_{ij} are calculated by including the event cone with the derived profile perpendicular to the cone, and the length parallel to the cone.

Hence, the approximation of the response is a complex process which has to include all the measurement variables, resulting in a high-dimensional calculation. The first approximation, the simplest form, consists of using 1D Gaussian distributions to estimate the profile and the length, where the widths correspond to the values derived from ARM and SPD (see Section 2.2.2). A second approximation form is to find an estimation function, which includes the measured energy information. This new approximation will allow integrating in the imaging response of events which are incompletely absorbed into the detector. In the case of gamma rays emitted during target (e.g., PMMA phantom) irradiation by hadron beams, events which are not full-stopped into the detector are likely to appear. Hence, including the measured energy increase the accuracy of the response description, and consequently, the quality of the final results.

The final aim of hadron therapy monitoring is the determination of the delivered dose location during irradiation. A first goal for a usefulness proof of the proposed gamma-ray imaging technique can be to reach a detection capability of the dose fall-off region of the order of millimeters from the reconstructed images. Alternatively, a solution could be to determine a filter function which applied to the planned dose deposition will match to the estimated gamma-ray distribution, which will be further compared to the measured gamma-ray distribution.

Possible perspectives include also a more complex characterization of the dose when studying the feasibility of the treatment monitoring method. In addition, everything which can be included in more complex irradiation scenarios, e.g., modulation wheel inserted in the beam configuration, complex phantoms (different materials, dimensions), SOBP, may be considered. In order to more accurately select the real reasons for which potential disagreements between the measured and predicted dose deposition are detected, multi-modality imaging techniques, e.g., Compton imaging/CT, could be envisioned.

Bibliography

[Agostinelli et al., 2003] Agostinelli, S., Allison, J., Amako, K., Apostolakis, J., Araujo, H., Arce, P., Asai, M., and Axen, D. (2003). Geant4-a simulation toolkit. *Nuclear Instruments and Methods in Physics Research Section A: Accelerators, Spectrometers, Detectors and Associated Equipment*, 506(3):250 – 303.

[Andia et al., 2002] Andia, B., Sauer, K., and Bouman, C. (2002). Nonlinear backprojection for tomographic reconstruction . *IEEE Trans. Nucl. Sci.*, 49:61–68.

[Andritschke, 2006] Andritschke, R. (2006). *Calibration of the MEGA Prototype*. PhD thesis, Technical University Munich, Germany. to be published.

[Anscombe, 1948] Anscombe, F. J. (1948). The transformation of poisson, binomial and negative-binomial data. *Biometrika*, 35:246–254.

[Basko et al., 1999] Basko, R., Zeng, G. L., and Gulberg, G. T. (1999). Application of spherical harmonics to image reconstruction for the compton camera. *Phys. Med. Biol.*, 43:887–894.

[Bhattacharya et al., 2004] Bhattacharya, D. et al. (2004). Prototype tigre compton γ-ray balloon-borne instrument. 48:287–292.

[Bolozdynya et al., 1997] Bolozdynya, A., Ordonez, C. E., and Chang, W. (1997). A concept of cylindrical Compton camera for SPECT. In *Proceedings of the 1997 IEEE Nuclear Science Symposium*, pages 1047–51.

[Bortfeld and Oelfke, 1999] Bortfeld, T. and Oelfke, U. (1999). Fast and exact 2D image reconstruction by means of Chebyshev decomposition and backprojection. *Phys. in Med. and Biol.*, 44:1105–1120.

[Brechner and Singh, 1990] Brechner, R. R. and Singh, M. (1990). Iterative reconstruction of electronically collimated SPECT images. *IEEE Trans. Nucl. Sci.*, 37:1328–1332.

[Brechner et al., 1987] Brechner, R. R., Singh, M., and Leahy, R. (1987). Computer simulated studies of tomographic reconstruction with an electronically collimated camera for SPECT. *IEEE Trans. Nucl. Sci.*, 34:369–373.

[Chang et al., 2000] Chang, S. G., Yu, B., and Vetterli, M. (2000). Adaptive wavelet thresholding for image denoising and compression. *IEEE Trans. on Image Process.*, 9(9):1532–1546.

[Chelikani et al., 2004] Chelikani, S., Gore, J., and Zubal, G. (2004). Optimizing compton camera geometries. *Physics in Medicine and Biology*, 49(8):1387–1408.

[Cree and Bones, 1994] Cree, M. J. and Bones, P. J. (1994). Towards direct reconstruction from a gamma camera based on compton scattering. *IEEE Trans. Med. Imaging*, 13:398–407.

[Crespo et al., 2001] Crespo, P., Debus, J., Enghardt, W., Haberer, T., Jakel, O., Kramer, M., and Kraft, G. (2001). Tumor Therapy with Carbon Ion Beams. *Physica Medica*, XVII Suppl. 4.

[Daubechies, 1992] Daubechies, I. (1992). *Ten Lectures on Wavelets*. SIAM: Society for Industrial and Applied Mathematics.

[Defrise and Gullberg, 2006] Defrise, M. and Gullberg, G. T. (2006). Image reconstruction. *Physics in Medicine and Biology*, 51(13):R139–R154.

[Dixon et al., 1996] Dixon, D., Johnson, W., Kurfess, J., Pina, R., Puetter, R., Purcell, W., Tumer, T., Wheaton, W., and Zych, A. (1996). Pixon-based deconvolution. *Astron. Astrophys. Suppl. Ser.*, 120:683–686.

[Donoho, 1993] Donoho, D. L. (1993). Nonlinear wavelet methods for recovery of signals, densities, and spectra from indirect and noisy data. In *In Proceedings of Symposia in Applied Mathematics*, pages 173–205. American Mathematical Society.

[Donoho and Johnstone, 1994] Donoho, D. L. and Johnstone, I. M. (1994). Ideal spatial adaptation by wavelet shrinkage. *Biometrika*, 81(3):425–455.

[Donoho and Johnstone, 1995] Donoho, D. L. and Johnstone, I. M. (1995). Adapting to unknown smoothness via wavelet shrinkage. *J. Am. Stat. Assoc.*, 90:1200–1224.

[Donoho et al., 1995] Donoho, D. L., Johnstone, I. M., Kerkyacharian, G., and Picard, D. (1995). Wavelet shrinkage: Asymptopia? *J. of the Royal Stat. Soc., Series B*, 57:301–369.

[Du et al., 1999] Du, Y. F., He, Z., Knoll, G. F., Wehe, D. K., and Li, W. (1999). Evaluation of a compton scattering camera using 3d position-sensitive cdznte detectors. *SPIE Proc. Int. Soc. Opt. Eng.*, 32:228–238.

[Edholm and Herman, 1987] Edholm, P. R. and Herman, G. T. (1987). Linograms in image reconstruction from projections. *IEEE Trans Med Imaging*, 6:301–307.

[Fessler and Hero, 1994] Fessler, J. A. and Hero, A. O. (1994). Space-alternating generalized expectation-maximization algorithm. *IEEE Trans. Signal Processing*, 42:2664–2677.

[Fessler and Hero, 1995] Fessler, J. A. and Hero, A. O. (1995). Penalized maximum-likelihood image reconstruction using space-alternating generalized em algorithms. *IEEE Trans. Image Proc.*, 4:1417–1429.

[Fisz, 1955] Fisz, M. (1955). The limiting distribution function of two independent random variables and its statistical application. *Colloquium Mathematicum*, 3:138–146.

[Frandes et al., 2010a] Frandes, M., Magnin, E., and Prost, R. (2010a). List-Mode Wavelet Thresholding MLEM algorithm for Compton Imaging. In *IEEE Nucl. Sci.* submitted.

[Frandes et al., 2009] Frandes, M., Maxim, V., and Prost, R. (2009). List-Mode Wavelet-Based Multiresolution Image Reconstruction for Compton Imaging. In *Proceedings of the 2009 IEEE Nuclear Science Symposium*, pages 3781–3785.

[Frandes et al., 2010b] Frandes, M., Zoglauer, A., Maxim, V., and Prost, R. (2010b). A Tracking Compton-scattering Imaging System for Hadron Therapy Monitoring. *IEEE Trans Nucl Sci*, 57:144–150.

[Frandes et al., 2010c] Frandes, M., Zoglauer, A., Maxim, V., and Prost, R. (2010c). A Tracking Compton-scattering Imaging System for Hadron Therapy Monitoring. *IEEE Trans. Nucl. Sci.*, 57:144–150.

[Gehrels and other, 1999] Gehrels, N. and other (1999). Glast: the next-generation high energy gamma-ray astronomy mission. *Astroparticle Physics*, 11(1):277–282.

[Gordon et al., 1970] Gordon, R., Bender, R., and Herman, G. T. (1970). Algebraic Reconstruction Techniques (ART) for three-dimensional Electron Microscopy and X-ray photography. *J. Theor. Biol.*, 29:471–481.

[Gunter, 2006] Gunter, D. L. (2006). Filtered backprojection algorithms for compton cameras in nuclear medicine,. *Patent*.

[Halloin, 2003] Halloin, H. (2003). *CLAIRE: Premières Lumières d'une Lentille Gamma*. PhD thesis, Université Paul Sabatier de Toulouse.

[Hebert et al., 1990] Hebert, T., Leahy, R., and Singh, M. (1990). Three-dimensional maximum-likelihood reconstruction for an electronically collimated single-photon-emission imaging system. *J. Opt. Soc. Am. A*, 7:1305–1313.

[Herman and Lent, 1976] Herman, G. T. and Lent, A. (1976). Iterative reconstruction algorithms. *Computers in Biology and Medicine*, 6(4):273 – 294.

[Hudson and Larkin, 1994] Hudson, H. and Larkin, R. (1994). Accelerated image reconstruction using ordered subsets of projection data. *IEEE Trans. Med. Imag.*, 13:601–609.

[Huesman et al., 2000] Huesman, R., Klein, G., Moses, W., and Qi, J. (2000). List-mode maximum-likelihood reconstruction applied to positron emission mammography (PEM) with irregular sampling. *IEEE Trans. Med. Imaging*, 19:532–537.

[Johnstone and Silverman, 1997] Johnstone, I. M. and Silverman, B. W. (1997). Wavelet threshold estimators for data with correlated noise. *Journal of the Royal Statistical Society B*, 59(2):319–351.

[Kamae et al., 1988] Kamae, T., Hanada, N., and Enomoto, R. (1988). Prototype design of multiple Compton gamma-ray camera. *IEEE Trans. Nucl. Sci.*, 35:352–355.

[Kim et al., 2007] Kim, S. M., Lee, J. S., and Lee, S.-J. (2007). Fully Three-Dimensional Image Reconstruction for Compton Imaging Using Ordered Subsets of Conical Projection Data. In *Nuclear Science Symposium Conference Record*, pages 3070–3073.

[Kippen, 2004] Kippen, R. (2004). The GEANT low energy Compton scattering (GLECS) package for use in simulating advanced Compton telescopes. 48:221–226.

[Knödlseder et al., 1999] Knödlseder, J., Dixon, D., Bennett, K., Bloemen, H., Diehl, R., Hermsen, W., Oberlack, U., Ryan, J., Schönfelder, V., and von Ballmoos, P. (1999). Image Reconstruction of COMPTEL 1.8 MeV 26Al Line Data. *Astron. Astrophys.*, 345:813–825.

[Knoll, 2000] Knoll, G. F. (2000). *Radiation Detection and Measurement*. John Wiley & Sons, New York, 3rd edition.

[Kramer et al., 2000] Kramer, M., Jakel, O., Haberer, T., Kraft, G., Schardt, D., and Weber, U. (2000). Treatment planning for heavy-ion radiotherapy: physical beam model and dose optimization. *Physics in Medicine and Biology*, 45(11):3299–3317.

[Lange et al., 1987] Lange, K., Bahn, M., and R., L. (1987). A theoretical study of some maximum likelihood algorithms for emission and transmission tomography. *IEEE Trans Med Imaging*, 6:106–14.

[Lange and Carson, 1984] Lange, K. and Carson, R. (1984). EM reconstruction algorithms for emission and transmission tomography. *J. Comput. Assist. Tomogr.*, 8:306–316.

[Leblanc et al., 1999] Leblanc, J. W., Clinthorne, N. H., Hua, C. H., Nygard, E., Rogers, W. L., Wehe, D. K., Weilhammer, P., and Wilderman, S. J. (1999). Experimental results from the C-SPRINT prototype Compton camera. *IEEE Trans. Nucl. Sci.*, 46(3):201–204.

[Lee et al., 2008] Lee, S., Lee, M., Nguyen, V., Kim, S., and Lee, J. (2008). Three-Dimensional Edge-Preserving Regularization for Compton Camera Reconstruction. In *Proceedings of the 2008 Nuclear Science Symposium*, pages 3070–3073.

[Lee, 2008] Lee, S.-J. e. a. (2008). Three-Dimensional Edge-Preserving Regularization for Compton Camera Reconstruction. In *Nuclear Science Symposium Conference Record*, pages 3070–3073.

[Liang et al., 1989] Liang, Z., Jaszczak, R., and Greer, K. (1989). On Bayesian image reconstruction from projections: uniform and nonuniform a priori source information . *IEEE Trans Med Imaging*, 8:227–35.

[Mallat, 1999] Mallat, S. (1999). *A Wavelet Tour of Signal Processing*. Academic Press.

[Maxim et al., 2009] Maxim, V., Frandes, M., and Prost, R. (2009). Analytical inversion of the Compton Transform using the full set of available projections. *Inverse Probl.*, 9:1–21.

[Min et al., 2006] Min, C.-H., Kim, C.-H., Youn, M.-Y., and Kim, J.-W. (2006). Prompt gamma measurements for locating the dose falloff region in the proton therapy. *Appl. Phys. Lett.*, 89.

[Murtagh et al., 1995] Murtagh, F., Starck, J.-L., and Bijaoui, A. (1995). Image restoration with noise suppression using a multiresolution support. *Astron. and Astrophys., Suppl. Ser*, 112:179–189.

[Parodi, 2004] Parodi, K. (2004). *On the feasibility of dose quantication with in-beam PET data in radiotherapy with and proton beams*. Ph.d., TU Dresden.

[Parodi and Bortfeld, 2006] Parodi, K. and Bortfeld, T. (2006). A filtering approach based on gaussian-powerlaw convolutions for local PET verification of proton radiotherapy. *Phys. Med. Biol.*, 51:1991–2009.

[Parodi et al., 2002] Parodi, K., Enghardt, W., and Haberer, T. (2002). In-beam PET measurements of $beta^+$-radioactivity induced by proton beams. *Phys. Med. Biol.*, 47:21–36.

[Parra and Barrett, 1998] Parra, L. and Barrett, H. (1998). List-mode likelihood: EM algorithm and image quality estimation demonstrated on 2-D PET. *Medical Imaging, IEEE Transactions on*, 17(2):228 –235.

[Parra, 2000] Parra, L. C. (2000). Reconstruction of cone-beam projections from compton scattered data. *IEEE Trans. Nucl. Sci.*, 47:1543–50.

[Pommier et al., 2002] Pommier, P., Balosso, J., Bolla, M., and Gérard, J. P. (2002). Le projet français étoileÂă: données médicales actuelles de l'hadronthérapie par ions légers. the french project etoile: review of clinical data for light ion hadrontherapy. *Cancer/Radiotherapie*, 6(6):369 – 378.

[Qi and Leahy, 2006] Qi, J. and Leahy, R. M. (2006). Iterative reconstruction techniques in emission computed tomography. *Physics in Medicine and Biology*, 51(15):R541–R578.

[Ribberfors, 1975] Ribberfors, R. (1975). Relationship of the relativistic Compton cross section to the momentum distribution of bound electron states. ii. effects of anisotropy and polarization. *Physical Review B*, 12:3136–3141.

[Ribberfors and Berggren, 1982] Ribberfors, R. and Berggren, K.-F. (1982). Incoherent-X-ray-scattering functions and cross sections by means of a pocket calculator. *Physical Review A*, 26:3325–3333.

[Sardy et al., 2004] Sardy, S., Antoniadis, A., and Tseng, P. (2004). Automatic smoothing with wavelets for a wide class of distributions. *J. Comput. Graph. Stat.*, 13:399–421.

[Sauve et al., 1993] Sauve, A. C., Hero, A. O., Rogers, W. L., and Clinthone, N. H. (1993). 3D image reconstruction for a Compton SPECT camera model. *IEEE Trans. Nucl. Sci.*, 46:2027–84.

[Schönfelder et al., 1993a] Schönfelder, V., Aarts, H., Bennett, K., de Boer, H., Clear, J., and Collmar, W. (1993a). Instrument description and performance of the imaging gamma-ray telescope COMPTEL aboard the Compton Gamma-Ray Observatory. *Astrophys. J. Suppl.*, (86):657–692.

[Schönfelder et al., 1993b] Schönfelder, V., Aarts, H., Bennett, K., de Boer, H., Clear, J., and Collmar, W. (1993b). Instrument description and performance of the imaging gamma-ray telescope COMPTEL aboard the Compton Gamma-Ray Observatory. *Astrophys. J. Suppl.*, (86):657–692.

[Schönfelder et al., 1973] Schönfelder, V., Hirner, A., and Schneider, K. (1973). A telescope for soft gamma ray astronomy. *Nuclear Instruments and Methods*, 107:385–394.

[Shepp and Vardi, 1982] Shepp, L. A. and Vardi, Y. (1982). Maximum Likelihood Reconstruction for Emission Tomography. *Medical Imaging, IEEE Transactions on*, 1(2):113–122.

[Singh and Doria, 1983a] Singh, M. and Doria, D. (1983a). An electronically collimated gamma camera for single photon emission computed tomography. Part I: Theoretical considerations and design criteria. *Med.Phys.*, 10:421–427.

[Singh and Doria, 1983b] Singh, M. and Doria, D. (1983b). An electronically collimated gamma camera for single photon emission computed tomography. Part II: Image reconstruction and preliminary experimental measurements. *Med.Phys.*, 10:428–435.

[Singh and Doria, 1985] Singh, M. and Doria, D. (1985). Single photon imaging with electronic collimation. *IEEE Trans. Nucl. Sci.*, 32(1):843–847.

[Sisterson, 2005] Sisterson, J. (2005). A Newsletter for those interested in proton, light ion and heavy charged particle radiotherapy. *Particles*, 36:1–11.

[Snyder et al., 1987] Snyder, D. L., Miller, M., Thomas, L., and Politte, D. (1987). Noise and Edge Artifacts in Maximum-likelihood Reconstrcutions for Emission Tomography. *IEEE Trans. Med. Imag.*, 3:228–238.

[Strong et al., 1990] Strong, W. A., Bennett, K., Cabeza-Orcel, P., Deerenberg, A., Diehl, R., den Herder, W. J., Hermsen, W., Lichti, G., Lockwood, J., McConnell, M., Macri, J., Morris, D., Much, R., Ryan, J., Schönfelder, V., Simpson, G., Steinle, H., Swanenburg, N. B., and Winkler, C. (1990). Maximum Entropy Imaging with COMPTEL Data. In *International Cosmic Ray Conference*, volume 4 of *International Cosmic Ray Conference*, pages 154–+.

[Tanimori et al., 2004] Tanimori, T., Kubo, H., Miuchi, K., Nagayoshi, T., Orito, R., Takada, A., Takeda, A., and Ueno, M. (2004). Mev gamma-ray imaging detector with micro-tpc. *New Astronomy Reviews*, 48(1-4):263 – 268. Astronomy with Radioactivities IV and Filling the Sensitivity Gap in MeV Astronomy.

[Tavani et al., 2003] Tavani, M. et al. (2003). The agile instrument. In Truemper, J. and Tananbaum, H., editors, *X-Ray and Gamma-Ray Telescopes and Instruments for Astronomy*, volume 4851, pages 1151–1162. SPIE.

[Timmermann and Nowak, 1999] Timmermann, K. E. and Nowak, R. D. (1999). Multiscale Modeling and Estimation of Poisson Processes with Application to Photon-limited Imaging. *IEEE Trans. on Info. Theory*, 45:846–862.

[Todd et al., 1974] Todd, R. W., Nightingale, J. M., and Everett, D. B. (1974). A proposed gamma camera. *Nature*, 251:132–134.

[Tomitani and Hirasawa, 2002] Tomitani, T. and Hirasawa, H. (2002). Image reconstruction from limited angle Compton camera data. *Phys. Med. Biol.*, 47:2129–2145.

[Tumer et al., 1997] Tumer, T. O., Yin, S., and Kravis, S. (1997). A high sensitivity, electronically collimated gamma camera. *IEEE Trans. Nucl. Sci.*, 44:889–904.

[Vandenberghe et al., 2001] Vandenberghe, S., D'Asseler, Y., Van de Walle, R., Kauppinen, T., Koole, M., Bouwens, L., Van Laere, K., Lemahieu, I., and Dierckx, R. (2001). Iterative reconstruction algorithms in nuclear medicine . *Computerized Medical Imaging and Graphics*, 25:105–111.

[Wilderman et al., 1998a] Wilderman, S. J., Clinthorne, N. H., Fessler, J. A., and Rogers, W. L. (1998a). List-mode maximum likelihood reconstruction of Compton scatter camera images in nuclear medicine. In *Proceedings of the 1998 IEEE Nuclear Science Symposium*, volume 3, pages 1716–1720.

[Wilderman et al., 2001] Wilderman, S. J., Fessler, J., Clinthorne, N., LeBlanc, J., and Rogers, W. (2001). Improved Modeling of System Response in List-Mode EM Reconstruction of Compton Scatter Camera Images. *IEEE Trans. Nucl. Sci.*, 48:111–116.

[Wilderman et al., 1999] Wilderman, S. J., Fessler, J. A., Clinthorne, N. H., Leblanc, J. W., and Rogers, W. L. (1999). Improved modeling of system response in list mode em reconstruction of compton scatter camera images. In *Proceedings of the 1999 IEEE Nuclear Science Symposium*, pages 1052–1056.

[Wilderman et al., 1998b] Wilderman, S. J., Les Rogers, W., Knoll, G., and Engdahl, J. (1998b). Fast algorithm for list mode back-projection of Compton scatter camera data. *IEEE Trans. Nucl. Sci.*, 45:957–962.

[Xu and He, 2007] Xu, D. and He, Z. (2007). Gamma-ray energy-imaging integrated spectral deconvolution. *Nuclear Instruments and Methods in Physics Research Section A: Accelerators, Spectrometers, Detectors and Associated Equipment*, 574(1):98 – 109.

[Zoglauer, 2000] Zoglauer, A. (2000). *Methoden der Bildrekonstruktion füer das Comptonteleskop MEGA*. Diploma thesis, Technische Universität München.

[Zoglauer, 2005] Zoglauer, A. (2005). *First Light for the Next Generation of Compton and Pair Telescopes*. Doctoral thesis, Technische Universität München.

[Zoglauer et al., 2007] Zoglauer, A., Andritschke, R., Kanbach, G., and Boggs, S. E. (2007). A Bayesian-based Method for Particle Track Identification in Low-energy Pair-creation Telescopes. In Ritz, S., Michelson, P., and Meegan, C., editors, *AIP Conference proceedings: The First GLAST Symposium*, volume 921, pages 584–585.

[Zoglauer et al., 2006] Zoglauer, A., Andritschke, R., and Schopper, F. (2006). MEGAlib — The Medium Energy Gamma-ray Astronomy Library. *New Astron. Rev.*, 50:629–632.

[Zoglauer and Boggs, 2007] Zoglauer, A. and Boggs, S. E. (2007). Application of Neural Networks to the Identification of the Compton Interaction Sequence in Compton Imagers. In *IEEE Nuclear Science Symposium Conference*, volume 6, pages 4436–4441.

[Zoglauer and Kanbach, 2003] Zoglauer, A. and Kanbach, G. (2003). Doppler broadening as a lower limit to the angular resolution of next generation Compton telescopes. Proceedings of SPIE.

Acknowledgements

I would like to thank all those who have contributed to this work, and in particular to:

- Rémy Prost and Voichiţa Maxim, my advisors, for their collaboration during the thesis period, for allowing me to present the work at international conferences.
- Isabelle Magnin, the laboratory director, for managing the problems which appeared, and for the work suggestions.
- Michael Cree for sending me a copy of his PhD thesis, which was really helpful.
- Jürgen Knödlseder for answering my questions, and all those who made free-available study materials (courses, programs, presentations).
- All my office colleagues throughout this period, especially to Feng Yang, for her enthusiasm for conversations about work, french, cultural traditions.
- The community of St. Archangels for their acceptance, especially at my arrival, and for all Sundays which made me feel well integrated in Lyon.
- Andreas Zoglauer for his intellectual generosity, his help since this work initially started to take shape; namely, for his help to handle MEGAlib, his advises to manage the simulation files, to start reading articles about iterative image reconstruction algorithms applied in astrophysics, for well understanding problems although being at a very long distance, for... many other things which would need too much space for being possible to write them all here.

And my very special thanks go to my parents for their unconditioned support.

FOLIO ADMINISTRATIF

NOM: Frandes
PRÉNOM: Mirela

DATE DE SOUTENANCE: le 16 septembre 2010

TITRE: Détection des rayons gamma et reconstruction d'images pour la caméra Compton: Application à l'hadronthérapie.

NATURE: Doctorat

NUMÉRO D'ORDRE: 2010-ISAL-0067

ECOLE DOCTORALE: Électronique, Électrotechnique et Automatique
SPÉCIALITÉ: IMAGES ET SYSTÈMES

COTE B.I.U. LYON :

CLASSE:

RÉSUMÉ:

Une nouvelle technique de radiothérapie, l'hadronthérapie, irradie les tumeurs à l'aide d'un faisceau de protons ou d'ions carbone. L'hadronthérapie est très efficace pour le traitement du cancer car elle permet le dépôt d'une dose létale très localisée, en un point dit 'pic de Bragg', à la fin du trajet des particules. La connaissance de la position du pic de Bragg, avec une précision millimétrique, est essentielle car l'hadronthérapie a prouvé son efficacité dans le traitement des tumeurs profondes, près des organes vitaux, ou radio-résistantes.

Un enjeu majeur de l'hadronthérapie est le contrôle de la délivrance de la dose pendant l'irradiation. Actuellement, les centres de traitement par hadronthérapie effectuent un contrôle post-thérapeutique par tomographie par émission de positron (TEP). Les rayons gamma utilisés proviennent de l'annihilation de positons émis lors la désintégration bêta des isotopes radioactifs créés par le faisceau de particules. Ils ne sont pas en coïncidence directe avec le pic de Bragg. Une alternative est l'imagerie des rayons gamma nucléaires émis suites aux interactions inélastiques des hadrons avec les noyaux des tissus. Cette émission est isotrope, présentant un spectre à haute énergie allant de 100 keV à 20 MeV. La mesure de ces rayons gamma énergétiques dépasse la capacité des systèmes d'imagerie médicale existants. Une technique avancée de détection des rayons gamma est proposée. Elle est basée sur la diffusion Compton avec possibilité de poursuite des électrons diffusés. Cette technique de détection Compton a été initialement appliquée pour observer les rayons gamma en astrophysique (télescope Compton). Un dispositif, inspiré de cette technique, a été modélisé avec une géométrie adaptée à l'Imagerie en HadronThérapie (IHT). Il se compose d'un diffuseur, où les électrons Compton sont mesurés et suivis ('tracker'), et d'un calorimètre, où les rayons gamma sont absorbés par effet photoélectrique. Un scénario d'hadronthérapie a été simulé par la méthode de Monte-Carlo, en suivant la chaîne complète de détection, de la reconstruction d'événements individuels jusqu'à la reconstruction d'images de la source de rayons gamma. L'algorithme 'Expectation Maximisation' (EM) à été adopté dans le calcul de l'estimateur du maximum de vraisemblance (MLEM) en mode liste pour effectuer la reconstruction d'images. Il prend en compte la réponse du système d'imagerie qui décrit le comportement complexe du détecteur. La modélisation de cette réponse nécessite des calculs complexes, en fonction de l'angle d'incidence de tous les photons détectés, de l'angle Compton dans le diffuseur et de la direction des électrons diffusés. Dans sa forme la plus simple, la réponse du système à un événement est décrite par une conique, intersection du cône Compton et du plan dans lequel l'image est reconstruite. Une forte corrélation a été observée entre l'image de la source gamma reconstruite et la position du pic de Bragg. Les performances du système IHT dépendent du détecteur, en termes d'efficacité de détection, de résolution spatiale et énergétique, du temps d'acquisition et de l'algorithme utilisé pour reconstituer l'activité de la source de rayons gamma.

L'algorithme de reconstruction de l'image a une importance fondamentale. En raison du faible nombre de photons mesurés (statistique de Poisson), des incertitudes induites par la résolution finie en énergie, de l'effet Doppler, des dimensions limitées et des artefacts générés par l'algorithme itératif MLEM, les images IHT reconstruites sont affectées d'artefacts que l'on regroupe sous le terme 'bruit'. Ce bruit est variable dans l'espace et dépend du signal, ce qui représente un obstacle majeur pour l'extraction d'information. Ainsi des techniques de dé-bruitage ont été utilisées. Une stratégie de régularisation de l'algorithme MLEM (WREM) en mode liste a été développée et appliquée pour reconstituer des images Compton. Cette proposition est multi-résolution sur une base d'ondelettes orthogonales. A chaque itération, une étape de seuillage des coefficients d'ondelettes a été intégrée. La variance du bruit a été estimée à chaque itération par la valeur médiane des coefficients de la sous-bande de haute fréquence. Cette approche stabilise le comportement de l'algorithme itératif, réduit l'erreur quadratique moyenne et améliore le contraste de l'image.

MOTS-CLÉS: Hadronthérapie, rayons gamma, imagerie Compton, reconstruction d'image, algorithme MLEM, ondelettes.

LABORATOIRES DE RECHERCHES: CREATIS (CNRS UMR 5520, INSERM U630)

DIRECTEURS DE THÈSE: Pr. Rémy Prost

COMPOSITION DU JURY: Mai Nguyen-Verger (Rapporteur), Laurent Desbat (Rapporteur), Denis Dauvergne, Isabelle Magnin, Voichita Maxim, Rémy Prost